Title
Collective motion in behaviorally heterogeneous systems

Permalink
https://escholarship.org/uc/item/8750d6nj

Author
Copenhagen, Katherine

Publication Date
2017

Peer reviewed|Thesis/dissertation

UNIVERSITY OF CALIFORNIA, MERCED

Collective motion in behaviorally heterogeneous systems

A dissertation submitted in partial satisfaction of the requirements for the degree Doctor
of Philosophy

in

Physics

by

Katherine Copenhagen

Committee in charge:

       Professor Linda Hirst, Chair
       Professor Ajay Gopinathan, Advisor
       Professor Arnold Kim
       Professor Kevin Mitchell

2017

The Dissertation of Katherine Copenhagen is approved, and it is acceptable in quality and form for publication on microfilm and electronically:

_____

Ajay Gopinathan

_____

Kevin Mitchell

_____

Arnold Kim

_____

Linda Hirst, Chair

University of California, Merced
2017

To Genny, Richie, Keith and Linda

and the rest of my family. You are all the best.

Abstract

University of California, Merced 2017
Doctor of Philosophy
Collective motion in behaviorally heterogeneous systems
Katherine Copenhagen
PI: Professor Ajay Gopinathan, Chair: Professor Linda Hirst

Collective motion is a widespread phenomenon in nature where individuals actively propel themselves, gather together and move as a group. Some examples of collective motion are bird flocks, fish schools, bacteria swarms, cell clusters, and crowds of people. Many models seek to understand the effects of activity in collective systems including things such as environmental disorder, density, and interaction details primarily at infinite size limits and with uniform populations. In this dissertation I investigate the effects of finite sizes and behavioral heterogeneity as it exists in nature. Behavioral heterogeneity can originate from several different sources. Mixed populations of individuals can have inherently different behaviors such as mutant bacteria, injured fish, or agents that prefer individualistic behavior over coordinated motion. Alternatively, agents may modify their own behavior based on some local environmental dependency, such as local substrate, or density.

In cases such as mutant cheaters in bacteria or malfunctioning drones in swarms, mixed populations of behaviorally heterogeneous agents can be modelled as arising in the form of aligning and non-aligning agents. When this kind of heterogeneity is introduced, there is a critical carrying capacity of non-aligners above which the system is unable to form a cohesive ordered group. However, if the cohesion of the group is relaxed to allow for fracture, the system will actively sort out non-aligning agents the system will exist at a critical non-aligner fraction. A similar heterogeneity could result in a mixture of high and low noise individuals. In this case there is also a critical carry capacity beyond which the system is unable to reach an ordered state, however the nature of this transition depends on the model details.

Agents which are part of an ordered collective may vary their behavior as the group changes environments such as a flock of birds flying into a cloud. Using a unique model of a flock where the group behaves as a rigid disk reveals interesting behaviors as the system crosses a boundary between interfaces. The collective rotates and reorients or becomes stuck on the boundary as it crosses. I also investigate the effects of variable behavior depending on local density, and find that a frustration driven transient rotational phase arises in clusters where agents with low local density move faster than those with high local density as in cell clusters. All together I have shown that behavioral heterogeneity in collective motion can lead to unique phases and behaviors that are not seen in their homogeneous counterparts.

Contents

List of Figures

List of Tables

List of Symbols

Symbol	Description
d_v	Vision radius, for determining neighbor lists
t	Simulation time
$\vec{x}_i$	Agent position
$\hat{d}_i$	Agent direction of propulsion
$\vec{d}_A$	Direction of alignment interaction
$\vec{d}_{LJ}$	Direction of Lennard-Jones cohesive interaction
R	Agent prefered separation, or diameter
$\vec{\eta}$	Angular noise vector representation
α	Alignment interaction scaling factor
ϵ	Lennard-Jones potential interaction scaling factor
δt	Physical reaction time of agents
Δt	Simulation timestep
d_r	Reaction distance, distance moved in reaction time
f	Some fraction of the population selected at random
$\vec{s}_{ij}$	Separation vector pointing from agent i to agent j
s	Distance between two agents
$\mathcal{O}$	Order parameter of group polarization
f^*	Critical heterogeneity fraction
Θ	Direction angle of propulsion for agents
μ	Mean of a gaussian distribution
σ	Standar deviation of a gaussian distribution
N	System size - number of agents
$\mathcal{F}_i$	Agent fitness
$\phi_{\mathcal{O}}$	Fitness advantage for being in an ordered cluster
ϕ_c	Fitness advantage for being a cheater
Φ	Ratio of order fitness to cheater fitness advantages $(\phi_{\mathcal{O}}/\phi_c)$
n	Number of neighbors
$\mathcal{N}$	Normalized average largest cluster
$\mathcal{A}$	Angular momentum
$\vec{v}$	Agent velocity.

List of Abbreviations

nbr	**N**eigh**b**or
Sw	**Sw**arming
So	**So**rting
St	**St**atic
AL	**Al**igning model
NA	**N**ormalized **A**lignment model
AC	**A**ctive **C**olloid model
ABP	**A**ctive **B**rownian **P**article model

Acknowledgements

Curriculum Vita

EDUCATION

PhD, Physics - Start date: Fall 2012
University of California, Merced, CA 2017
GPA: 3.88
Bachelor of Science, Physics
University of California, Merced, CA 2011
GPA: 3.56

EXPERIENCE

Research Assistant   Summer 2013 - ongoing
Computational Biophysics Lab, Professor Ajay Gopinathan, UC Merced

- Wrote programs to simulate many different swarming systems with various behavioral heterogeneities.

- Collected data from simulations and analyze using Python, or Matlab, and published two papers.

Research Assistant   Academic Year 2012 - 2013
Quantum Dot Research Lab, Professor Michael Schiebner, UC Merced

- Began devolopment and set up of a time resolved spectroscopy experiment, for lifetime measurements of PbSe quantum dots.

Teaching Assistant   2012 - 2013, Spring 2015
UC Merced

- Prepared and directed lab and discussion sections for introductory math and physics courses.

Lab Demonstrator   Academic Year 2011 - 2012
University of Western Australia, Perth, Western Australia, Australia.

- Prepared labs and instructed a total of 13 sections of introductory and second year physics and chemistry courses.

- Helped develop and test new experiments for implementation into the class.

Research Assistant - Senior Thesis Project   Academic year 2010 - 2011
Superconductor research lab, Professor Raymond Chiao, UC Merced.

- Executed experiments using and operating a delution refridgerator.
- Calibrated and took measurements from a Hall Probe for magnetic fields.
- Analyzed data using Matlab

Research Assistant   Academic year 2008 - 2009
Laser Research Lab, Professor Jay Sharping, UC Merced.

- Assembled and tested multiple input detection and fiber-optic splitting devices for use in Graduate student's experiments.

Research Assistant   Summer 2005
Optics Research Lab, Professor David Copenhagen, University of California, San Francisco.

- Learned lab sanitary procedures including working with mice.

- Prepared solutions of antibodies and preservatives, as well as disecting and preparing samples of mouse eyes.

CONFERENCES & PRESENTATIONS

APS March Meeting 2017, Presentation.
APS March Meeting 2016, Presentation.
Dynamics Days 2016, Presentation.
APS CAM, Oaxaca 2015, Poster.
Gordon research conference 2015, Poster.
IGERT Summer institute bionanotechnology 2015, Poster.
APS March Meeting 2015, Presentation and Poster.
UC Merced Physics Colloquium 2014, Presentation.
UC Merced Foraging Workshop 2014, Presentation.
Physics Retreat 2014, Poster.
Quantitative Systems Biology Retreat 2014 and 2015, Poster.
APS March Meeting 2014, Presentation.
BPS 2014, Poster.
KITP 2014, Attended.
APS Far West 2013, Presentation.

PUBLICATIONS

1. Katherine Copenhagen, and Ajay Gopinathan. **Active matter clusters at interfaces.** *Frontiers in Materials.* 3 (13) 2016
2. Katherine Copenhagen, David A Quint, Ajay Gopinathan **Self-organized sorting limits behavioral variability in swarms.** *Nature's Scientific Reports.* 6 (31808) 2016
3. Katherine Copenhagen, Gema Malet-Engra, Weimiao Yu, Giorgio Scita, Nir Gov,and Ajay Gopinathan **Frustration induced phases in migrating cell clusters** arXiv Nature Communications (in review).

AWARDS FELLOWSHIPS

Deans Distinguished Scholar Fellowship Spring 2017.
Center for Cellular and Bio-molecular Machines Scholar 2016-2017.
IGERT fellowship June 2015 - June 2016.
Best poster QSB retreat May 2015.
UC Merced Physics Summer Fellowship, Summer 2016.
UC Merced Physics Summer Fellowship, Summer 2015.
UC Merced Physics Summer Fellowship, Summer 2014.
UC Merced Physics Summer Fellowship, Summer 2013.
UC Merced Travel Award Spring 2016.
UC Merced Travel Award Spring 2015.
UC Merced Travel Award Spring 2014.
Dean's Honors list, Fall 2010, Fall 2008, Spring 2008.
Chancellor's Honors list, Spring 2009.

OUTREACH

Elementary School educational assistant. Assisted with demonstrating the use of educational ipad apps to elementary school students.

Elementary School demonstration. Demonstrated robot experiments to a group of elementary students to inspire an interest in biophysics and higher education.

Physics Pizza Hour Organized a bi-weekly gathering for UC Merced Physics Graduate students and Faculty, 2014.

Adventure World Science Day Performed physics demonstrations at a booth for people of all ages. Perth, AU 2012.

Aboriginal Highschool Demonstrations Participated in an outreach program to introduce rural aboriginal high-school students to the opportunities in persuing science in University. Perth, AU 2012.

Prospective Student Fair, UWA Performed physics demonstrations for high school students considering attending University of Western Australia. Perth, AU 2011.

National Youth Science Forum Showed and explained physics demonstrations to selected students. Perth, AU 2011.

Physics Show Performed physics demonstrations for students visiting from the National University of Singapore. Perth, AU 2011.

Prospective Student Fair, UC Merced Guided lab tours for prospective students to see the lab facilities available for students considering attending UC Merced for Physics. Merced 2009

COMPUTER SKILLS

Languages & Software: C++, Python, R, Matlab, Bash, Java, LaTeX.

EXTRA-CURRICULAR ACTIVITIES

Delegate Assembly Member, 2014-2015.

Accomplished viola player, member of the Merced Sinfonia Baroque, 2013 - ongoing.
Member of the Mariposa symphony orchestra, ongoing. 2016 - ongoing.
Musician in local musicals of Oliver! (2015), Pirates of Penzance (2015) and Beauty and the Beast (2016) and Ragtime (2017).
Past member of Fremantle Symphony Orchestra, and Merced Symphony, 2008 - 2012.
Accomplished spring board diver, attended Nationals 2007, placed third in community college state competition 2008, placed record at Merced College 2009

Chapter 1

Introduction

1.1 Motivation

Living things can group up into large groups which behave as if they were a single object. Flocks of starlings fly around together as a single group which appears to act like a liquid with flowing waves [1, 2]. Fish schools act as one single unit rather than many fish acting as individuals [3]. Swarms of flies [4, 5], actin filaments inside our cells [6, 7], herds of wildebeests [8], bacteria swarms [9], cell clusters [10] and many more systems like these [11, 12, 13, 14, 15] are also all examples of collective motion. There are a few things that collective motion systems all have in common. First, individuals consume energy to propel themselves forwards, and second, individuals interact with eachother to form some structure or order on length scales much larger than the size of the individual constituents. The mechanism for propulsion and interaction between agents varies widely from system to system, but there are common features and collective behaviors that are carried over across length and timescales. Birds and fish interact by sight or sensing air or water flows, while bacteria and cells interact by chemical signaling and protein adhesions, and on an even smaller scale actin filaments interact through physical collisions, however all of theses systems show some similar long range collective behaviors in the form of velocity or position correlations.

Collective motion is an essential part of our lives and the world around us. When we move as part of a crowd or our cells move together during tumor formation or tissue development, the system behaviors are classified as collective motion. It is therefore important to study and understand collective motion, not only for learning about the world around us but also for health and safety, from escaping crowds and riots to preventing tumor spread. Further, we can learn from the strategies that have evolved in nature, to find efficient algorithms for drone swarms to improve performance for things like searching, foraging, exploring, or even reintroduction of essential factors for environmental health where they may have been wiped out such as reforrestation in burnt areas.

1.2 Background

When physicists began to gain interest in collective motion it was focussed particularly on the case where long range polar order is established. This occurs in bird flock when all of the birds align to fly in a consensus direction, or in fish schools, wildebeest herds and many

others. In 1995 Tamas Vicsek showed that a very simple model, where agents interact by aligning their direction of travel with neighboring agents, can result in a novel noise driven phase transition between an ordered and disordered state in two dimensions [16]. An analogy to a flocking system like these birds, but without self propulsion, i.e. agents simply reorient to align with neighboring agent directions but do not actively propel themselves, would be a magnetic system. This analogous system is the classic XY-model, where magnetic spins rotate to point the same direction as their neighbors. In the passive magnet XY-model in two dimensions, it is impossible to get an ordered phase or a phase transition with decreasing noise or temperature, so the fact that one exists in active systems is a surprising consequence of allowing aligning agents to propel themselves. After Vicsek showed the possibility of such a transition, Toner and Tu were able to analytically prove that the out of equilibrium nature of active systems allows for long range order to be established and a noise driven transition to exist in two dimensions [17].

The discovery of novel noise driven phase transitions in out of equilibrium active matter led physicists to study collective motion to find new phases and behaviors in collective motion. There are two main theoretical approaches to studying active matter. One is agent based modeling where each individual and it's interactions with other agents are modelled individually and positions are advanced with time. The second is hydrodynamic modeling where collective motion is described by a set of equations which represent the density and polarization of the agents with space and time.

1.2.1 Agent based modeling

Agent based models are implemented by defining a set of interactions and update rules for individuals and then letting the system evolve in time, according to a simple set of rules. Such systems show phase transitions driven by a wide variety of quantities including noise, density [11], environmental disorder [18], behavioral heterogeneities [19, 20, 74], and cohesive interaction details [21, 22]. They have also been used to study how swarms use cooperation to achieve specific goals which are useful to biological systems, such as cooperative decision making [23], agent segregation [24], and obstacle avoidance [25].

1.2.2 Hydrodynamic modeling

Hydrodynamic models define the local density and polarization through continuum equations which can then be numerically integrated to model the behavior of collective motion with time. They seek to understand the bulk properties of systems by utilizing periodic boundaries and studying thermodynamic properties. Studies of such systems in the thermodynamic limit of infinite size have revealed a number of interesting features including long-range, scale-free correlations and a discontinuous phase transition [26]. These thermodynamic limit studies have spurred interest in hydrodynamic and mean field theories to describe such phenomena [27], and have revealed interesting defect dynamics, phase transitions and collective behaviors in infinite size systems.

1.3 Collective motion with finite sizes and behavioral heterogeneity.

In nature, collective systems have boundaries and finite sizes which can have important effects of the collective motion of the system. Additionally, there is no reason that all agents in a collective systems in nature should behave identically. In this dissertation I implement these two features of natural collective motion systems that are often neglected in theoretical studies. From the perspective of finite system sizes I study behavioral variability using two slightly different approaches. The first is looking at systems of mixed populations where some subpopulation displays different behaviors than the remainder of the population throughout the simulation due to disease or malfunction. The second is by looking at environmentally driven behavioral variability where agents modify their individual behavior based on local environment.

1.3.1 Mixed population heterogeneity

Disorder can exist in the form of variability in behavior among members of the group, which has been modeled using agents with varying velocities [19, 28] or differing noise sensitivity [29], agents that stochastically switch off social interactions [20] and migratory groups of agents with varying sensitivity to external directional cues [30, 31]. An interesting manifestation of such behavioral heterogeneity would be swarms with agents that have varying abilities to process social cues. A specific scenario could be swarms with sub-populations of non-aligners that either refuse or are unable to participate in utilizing shared information with their neighbors resulting in significant impacts on the collective. For example, it has been observed in colonies of the quorum sensing bacteria *P. aureginosa* that colony collapse can occur if mutant cheaters (those that do not secrete signaling compounds to sustain colony swarming) are introduced into the swarm even though there are sufficient nutrients in the environment [32, 33, 34, 35, 36]. Differential behavior can also be a result of disease in organisms. For example, in locust swarms, the introduction of parasites (*Paranosema locustae*) inhibit the production of aggregation pheromones that promote gregarious behavior, thus resulting in a transition to an individualistic state [37]. In analogy to these biological systems, non-alignment behaviors could also arise in robotic drone swarms [38, 39], where software viruses or hardware failures could cause agents to malfunction, leading to an inability to swarm effectively and requiring the development of novel algorithms to alleviate this problem [40, 41, 42]. In chapter 2.1 we investigate the effects of non-alignment on swarming systems and find that swarms which are able to fracture exist at a critical carrying capacity of non-aligners and are able to adjust the non-aligner carrying capacity on the fly by changing speed, or spacing.

Another consequence of disease, mutation or malfunction, as described above, could be agents with variable diffusivities. In chapter 2.2 we examine several different models and the effects of heterogeneous diffusivities on swarming ability. We find that depending on the mechanism of cohesiveness interactions and alignment, increasing cohesive interaction strength can either promote or hinder swarming ability with increasing noise, and a high fraction of noisy agents will destroy a systems ability to align in an ordered cohesive unit.

1.3.2   Environmentally driven behavioral variability

Groups of individual organisms can self-organize to form cohesive clusters with directed motility in a spontaneously chosen consensus direction, for example a school of fish [43], cluster of cells during tumor spread, tissue development and repair [44, 45], or a herd of wildebeests [8]. These types of swarming systems will often encounter a change in the environment, such as a flock of birds flying into a cloud or area of lower air temperature, or a cluster of tumor cells invading changing tissue types [46]. Single cells have been shown to change their speed and direction when crossing sharp interfaces [47]. Swarms can also use collective dynamics to find and localize themselves to preferred niches or microenvironments. For example it has been observed that golden shiners, *Notemigonus crysoleucas*, which prefer low lighting, will spend more time in dark areas if they are part of a school, due to cooperative sensing capabilities of the group [48]. Bacteria have also been shown to take less time to reach a target with noisy chemical concentration gradients in the environment when they are part of a cluster [49]. Also, *e. coli.* clusters modify their own environment by secreting chemicals to create an environmental change between the inside and outside of the cluster in order to trap the *e. coli.* and maintain clustering behaviors [50]. It is therefore important to understand the effects of spatial environmental changes on a cohesive swarming group.

In chapter 3.1 we investigate finite swarming clusters moving through heterogeneous environments where agents change their speeds by exerting different propulsive forces within each environment. Such changes could arise from the agent's sensing and response to a variety of environmental factors such as temperature, substrate stiffness, or chemical composition. How is the path that a swarm takes affected by the presence of a boundary between different environments, and how does it depend on the properties of the cluster and the environmental change? We investigate these questions through a unique analytic model for swarming systems which treats the entire population as a single solid unit with self propulsion that can vary across the area of the flock, and show that under some realistic conditions the cluster exhibits a behavior with a remarkable resemblance to Snell's Law for light.

In chapter 3.2 we investigate cohesive cell clusters with agents which vary their behavior depending on transient local environment properties, specifically their local density, and find that this kind of heterogeneity can lead to unique phases of motion. We use an agent-based swarming model, which only allows short-range, nearest-neighbor interactions and unconfined space, similar to previous models found in the literature [23, 24, 51], to address the phenomenon of transient rotations in unconfined clusters. I show that a possible mechanism for driving cluster rotations is density-dependent cell propulsion. This density-dependent propulsion may be caused by contact inhibition of locomotion (CIL), whereby cell protrusions are inhibited by the adhesions between cells [52, 53]. Taken together, our results suggest a novel form of frustrated interactions between behaviorally different parts of the same cluster that can lead to unique collective dynamics – a finding that may have applications beyond the context of cellular clusters. I discuss the effects of environmentally dependent behavioral variation in Chapter 3.

Chapter 2

Mixed population heterogeneity

In collective motion systems, agents can experience malfunction, sickness, or energetically favorable fitness conditions which can lead to subpopulations which behave differently from the rest of the collection. These bahavioral variations can also be caused by mixed species or abilities within a swarm. In these systems when two different populations mix it can lead to interesting system behaviors. In this chapter I discuss the effects of errant individuals which refuse or are unable to participate in social alignment interactions in section 2.1, and mixtures of populations with differing noise, or rotational diffusivity in section 2.2.

2.1 Self-organized sorting limits behavioral heterogeneity in swarms

Collective motion in natural systems is a well studied phenomena that spans many spatial and temporal time scales [11, 12], ranging from protein filaments driven by molecular motors [6, 7], to swarming bacteria [9] and active colloidal crystals [14], to fish [3], birds [1], and even robot swarms [38, 54]. Such collective phenomena rely on the sharing or transmission of local information by constituents of the group leading to global consensus. Information flow and information fidelity are therefore critically important for collective systems to persist, especially in situations where disorder is an issue.

Disorder may exist in the environment and it has been recently shown that topological disorder in the form of obstacles can have significant detrimental effects on the ability for systems to move collectively [18, 25, 49]. Disorder can also exist in the form of variability in behavior among members of the group, which has been modeled using agents with varying velocities [19, 28] or differing noise sensitivity [29], agents that stochastically switch off social interactions [20] and migratory groups of agents with varying sensitivity to external directional cues [30, 31]. An interesting manifestation of such behavioral heterogeneity would be swarms with agents that have varying abilities to process social cues. A specific scenario could be swarms with sub-populations of non-aligners that either refuse or are unable to participate in utilizing shared information with their neighbors resulting in significant impacts on the collective. For example, it has been observed in colonies of the quorum sensing bacteria *P. aureginosa* that colony collapse can occur if mutant cheaters (those that do not secrete signaling compounds to sustain colony swarming) are introduced into the swarm even though there are sufficient nutrients in the environment [32, 33, 34, 35, 36]. Differential behavior can also be a result

of disease in organisms. For example, in locust swarms, the introduction of parasites (*Paranosema locustae*) inhibit the production of aggregation pheromones that promote gregarious behavior, thus resulting in a transition to a non-swarming state [37]. In analogy to these biological systems, non-alignment behaviors could also arise in robotic drone swarms [38, 39], where software viruses or hardware failures could cause agents to malfunction, leading to an inability to swarm effectively and requiring the development of novel algorithms to alleviate this problem [40, 41, 42].

Since differential behavior or non-alignment can be fairly ubiquitous in swarming systems and too many such non-aligners will have a deleterious effect on the ability to swarm, it poses a number of significant questions regarding how natural swarms deal with non-aligners or more generally variations in alignment ability. Is there a maximum fraction of non-aligners that a finite swarm can carry and is there a simple predictive relation between the maximum non-aligner carrying capacity and the characteristics of the swarm? Could there exist robust mechanisms that allow the whole group to increase its non-aligner carrying capacity? Are there mechanisms that allow swarms to limit the spread of non-aligning? Do these same mechanisms operate if the alignment abilities have a more natural continuous spread? If there are fitness advantages associated with non-aligning how does it affect the evolutionary dynamics? To address these issues, we study an agent based model of finite swarms with local aligning and cohesive interactions between neighbors and a sub-population of non-aligning agents within the group that do not align with their neighbors and do not have a defined internal preferred velocity.

2.1.1 The model

Agents exist in a continuous two dimensional space where each agent interacts with other agents in its immediate neighborhood defined by a vision radius d_v. At any given time, t, each agent has a position $\vec{x}_i$, and a direction of travel $\hat{d}_i$. The direction of travel of the agent at the next time step is computed by taking into account both alignment and cohesive interactions with its neighbors as well as noise. This is implemented by computing an alignment interaction vector, $\vec{d}_A$ and a cohesive interaction vector, $\vec{d}_{LJ}$. Here, $\vec{d}_A$ for an agent is the sum of the direction vectors of its nearby neighbors, which is proportional to the mean consensus direction (see methods for details). The form of the alignment interaction we use is common in studies of swarming systems and can be found in many variants of the standard Vicsek model [16, 55, 56], which was formulated originally to study a thermodynamic phase transition of aligning agents resulting from an increase in temperature or noise of the system. The form of the cohesive interaction is modeled as arising from a Lennard-Jones (LJ) interaction which is attractive at large distances and repulsive at close range (see methods for details). The effect of the LJ interaction in our model is to encourage agents to maintain a preferred distance (R) thus providing an overall cohesiveness as well as collision avoidance within the swarm, as seen in similar swarming systems [42, 22, 57]. In what follows, we set $R \sim 0.8d_v$, so that each agent sees only its first nearest neighbors on average, consistent with prior flocking models. The updated travel direction vector is then

$$\vec{d}_i(t) = \alpha \vec{d}_A + \epsilon \vec{d}_{LJ} + \vec{\eta} \tag{2.1}$$

where $\vec{\eta}$ represents noise. Noise is implemented as an angular adjustment to the calculated travel direction vector and is described in detail in the methods section below.

Here the parameters α and ϵ measure the importance of alignment and cohesiveness respectively (equation (3.14)). Directional updates are only performed in time intervals of δt corresponding to the physical reaction time of agents within the system. In contrast, positions are updated every simulation time-step, Δt, which can be made arbitrarily small. It is to be noted that velocity is encoded by a new length scale, d_r, the reaction distance, which determines how far an agent moves before reprocessing information, i.e. in time δt. Our model for the swarm produced expected stable collective dynamics [16], including order-disorder transitions as a function of noise (Fig. 2.1), which have been studied using both hydrodynamics [27, 58], and agent based models [26]. Although such agent based models are quite simple and leave out many microscopic details, they have been shown to produce a rich and complex phase space of collective motion that mimics the behavior of real physical and biological swarming systems [26, 5, 21, 43].
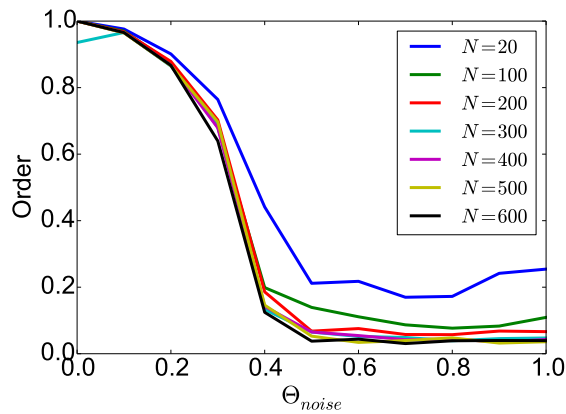
Figure 2.1: Order transition with noise for various system sizes.

To introduce behavioral heterogeneity in the form of non-aligners who refuse, or are unable, to participate in utilizing local alignment cues to guide their movements, we choose, at random, a fraction f of the swarming agents to be non-aligners after a transient time period where collective motion is established. Non-aligner agents follow the same update procedures as aligners, except that the alignment interaction is suppressed by setting $\alpha = 0$, so they no longer have any intrinsic tendency to align with their neighbors. Thus the only forces the non-aligners feel arise from the LJ potential.

The alignment interaction is implemented by the agent choosing an updated direction of travel that, in the absence of cohesive interactions or noise, is the sum of the direction vectors all its nearby neighbors, which is proportional to the mean consensus direction. In our model, at each reaction time step (δt), agents compute the summed direction $\vec{d}_A(t)$ (equation (2.2)) of all their neighbors (nbr) within a specified "vision" distance, d_v. δt is the physical reaction time of agents within the system, rather than the timestep of the simulation (Δt).

$$\vec{d}_A(t) = \sum_j^{nbr} \hat{d}_j(t - \delta t) \tag{2.2}$$

The cohesive interaction is modeled as arising from a Lennard-Jones (LJ) interaction (equation (2.3)) between nearest neighbor agents which is attractive at large distances and repulsive at close range. To calculate the LJ interaction, $\hat{s}_{ij}$ is a unit vector pointing between the ith and j^{th} agents and s is the separation between them.

$$\vec{d}_{LJ}(t) = -12 \times \sum_j^{nbr} \left[\frac{R^{13}}{s^{13}} - \frac{R^7}{s^7} \right] \hat{s}_{ij} \tag{2.3}$$

The standard Lennard-Jones force is equated to a LJ velocity due to the overdamped dynamics of the system. The agents calculate the alignment direction vector $\vec{d}_A$ as well as the LJ direction vector $\vec{d}_{LJ}$, dictated by the cohesive LJ interactions with all their neighbors (equation (2.3)) at each timestep. For our simulations the equilibrium separation between agents (R in equation (2.3)) is set to a distance, relative to the vision distance d_v, such that each agent will see, on average, only their first nearest neighbors. A new direction of travel for the agent in the next time step is determined by the vector formed by adding $\alpha \vec{d}_A(t)$ with $\epsilon \vec{d}_{LJ}$, where the parameters α and ϵ measure the importance of alignment and cohesiveness respectively (equation (2.1)).

New positions are then calculated for each agent according to equation (2.4), where d_r is the reaction distance, or how far an agent moves in each timestep.

$$\vec{x}_i(t + \Delta t) = \vec{x}_i(t) + \frac{d_r}{\delta t} \hat{d}_i(t) \Delta t \tag{2.4}$$

To mimic the response of real swarming individuals, we need to account for errors, either in processing local orientation information or in the execution of movement. Errors are modeled as noise that is added to the calculation of the updated direction $\vec{d}(t + \Delta t)$ by adding a randomly selected angle into the calculated direction, $\theta_i = \arctan d_{i,y}/d_{i,x} \pm \eta/2$. In our model we set $\eta = 0.2$, $d_v = 1$, $R = 0.7887$, $\Delta t = \delta t = 1$, and $\alpha = 1$.

Swarms are generated by randomly seeding N agents in a circle with radius equal to the vision radius of agents, d_v and then allowing the swarm to set its own size by following the dynamics dictated by equation (2.1) and equation (2.4). The system has infinite boundaries and varying the initial density, and simulation time step have little effect on the resulting transitions. The time during the simulation when the non-aligners are introduced makes little difference to the resulting transitions as seen below (Fig. 2.2). Initially the system is at $f = 0$, with no non-aligners, then at time t_0, a fraction of the system f is converted to non-aligners, and the order is measured after the system has reached steady state. Typically it takes less than 1000 time steps for the system to reach steady state, we wait until $t = 12000$ to measure the order to allow plenty of time for the system to stabilize.
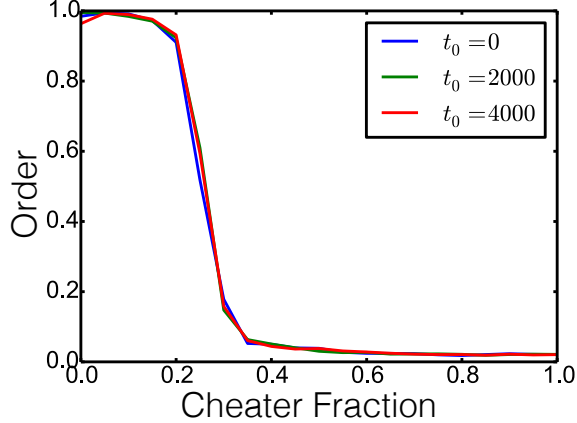
Figure 2.2: Order transition with non-aligner fraction where the non-aligners are introduced t_0 time steps into the simulation.

2.1.2 Results.

Large inter-agent cohesiveness limit.

We first consider the limit where the cohesive interactions are strong enough to produce a single swarm that cannot break apart and shows no rearrangements over time. This happens when $\epsilon \sim \alpha$, which is high enough to prevent the swarm from fracturing. Thus, once a random spatial distribution of non-aligners is established in the swarm, it remains fixed in a *locked-in* state thereafter. We begin by focusing on the effects of adding a fixed fraction of non-aligners, f, to our system and analyzing how the addition of these non-aligners affects the ability of the agents to swarm. To quantify the degree of order in the swarm we use the group polarization of all the agents, $\mathcal{O}$, defined by,

$$\mathcal{O} = \frac{1}{N} \left| \sum_{i=1}^{N} \hat{d}_i \right| \tag{2.5}$$

Fig. 2.5 (A) shows that as f increases, the swarm undergoes a sharp transition from an ordered swarming state where $\mathcal{O} \approx 1$ to a static disordered non-swarming state with $\mathcal{O} \approx 0$. The transition occurs at a critical non-aligner fraction, f^*, that is very weakly dependent on the system size as seen in Fig 2.5(a) where the transition occurs near $f^* \sim 0.5$ for $\epsilon = 1$, $d_v/d_r = 100$, and various different system sizes. On the left of the transition the system has a low non-aligner fraction and all agent directions are aligned with each other, shown by the black arrow heads in Fig. 2.5(B) with non-aligners in red and aligners in blue, while on the right of the transition the system is no longer able to form an ordered state, and agents instantaneously have random directions (Fig. 2.5(C)), resulting in a state with no net movement. It is to be noted that the time at which non-aligners are introduced does not affect the results shown and there appears to be very little hysteresis in the system (Fig. 2.2 and Fig. 2.3), suggesting a possible first order transition [20], which implies that the results for a fixed non-aligner fraction are fairly unique.

Hysteresis

Initializing the system with all non-aligners and introducing aligners has a slightly different effect on the order of the system than vice versa. To examine the difference we measured the order of the system as non-aligners are gradually added and then removed from the system with time. Initially the system has no non-aligners and $N = 100$ aligners and then one aligner is converted to non-aligner at a time and the system is allowed to relax for 100 time steps between each agent conversion. When only one non-aligner is being added at a time it takes much less time for the system to adjust accordingly and less than 100 time steps are necessary for the system to reach steady state. When the system reaches $f = 1$ the same process is repeated in reverse, converting one non-aligner to aligner at a time, allowing 100 time steps for the system to equilibrate between each step. This results in a slight hysteresis, Fig. 2.3, with a lower order when non-aligners are being removed from the system rather than added.
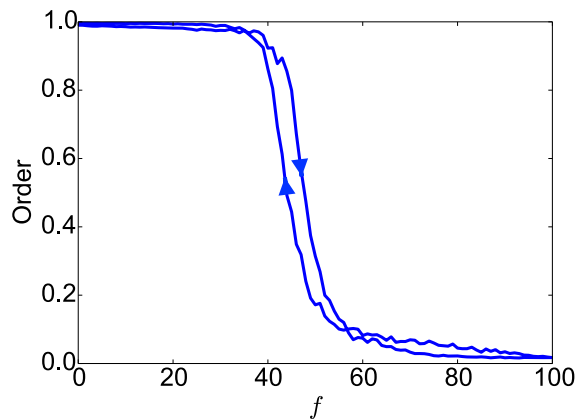
Figure 2.3: The order transition for the system when non-aligners are gradually added and then removed, resulting in a slight hysteresis.

Percolation driven transition

As information flow is crucial for the system to reach a consensus direction, a posible cause for the transition is the connectivity or percolation of aligning agents accross the system. Fig. 2.5 (b) shows snap shots of typical swarms in the ordered (top) and disordered (bottom) states. It is clearly visible that in the ordered state all of the directions of agents, shown as black arrows, are aligned and there is a high amount of connectivity between aligning agents (blue) within the swarm, shown as black connecting lines. In the disordered state the agent velocities are uncorrelated and there is very little connectivity of the non-cheaters within the swarm. How much connectivity is required for a system to swarm?

To understand if connectivity of the particles is the underlying mechanism that controls the order-disorder transition, we compare our system to standard models of percolation, including site percolation and $m = 3$ bootstrap percolation. Site percolation is a measure of the probability of randomly selecting an aligning agent that is part of the largest connected cluster in the system. Typically this should be the probability of any aligner being in a spanning cluster, but to avoid edge effects of our finite swarms we removed this restriction with the reasoning that if there is a spanning cluster it would be the largest cluster.

The probability that an aligning agent belongs to the largest site percolated network is shown in Fig. 2.5(c)(green-dashed line) as a function of the non-aligner fraction. This transition occurs at $f \approx 1/2$, which is near the transition value for site percolation in an infinite triangular lattice. Bootstrap percolation is similar to site percolation but with the added requirement that not only must a randomly selected aligning agent be part of the largest connected cluster, but to be considered part of a connected cluster it must have m aligning agent neighbors as well. Bootstrap percolation with $m = 3$ is shown in Fig. 2.5(c)(cyan) as well, and the transition occurs at $f \approx 0.4$ which is also the transition value for $m = 3$ bootstrap in an infinite triangular lattice. Comparing these two predicted behaviors, site and $m = 3$ bootstrap percolation, with that of the order-disorder phase transition our aligner and non-aligner mixed system (Fig. 2.5(c) (blue-solid)) over the range of non-aligner fractions implied that the level of connectivity for the aligners is much higher. We then counted the average number of like neighbors that each aligner has (red in Fig. 2.5(c)) and found that on average in an ordered system each aligning agent has at least four aligning neighbors.

The shape and position of the transitions for both site and $m = 3$ bootstrap percolation do not match the shape of the order transition. Additionally, the order transition depends on other parameters of the system such as speed and spacing which do not effect the percolation transitions, which depend purely on the relative positions of agents within the system, prompting us to examine other posible driving mechanisms for the order to disorder transition in swarms with non-aligning agents.
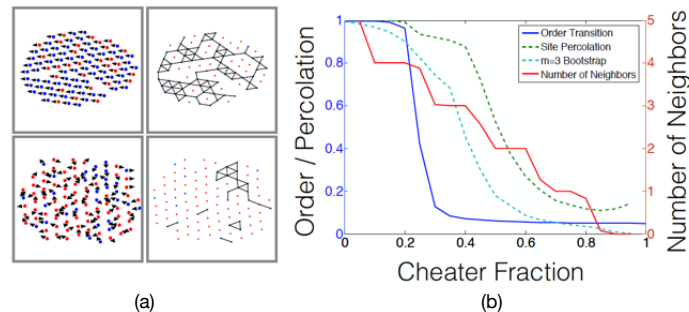
Figure 2.4: (a) With values of f below the order transition the particles all travel in the same direction (black arrow heads) and aligning agents show a high degree of connectivity (connecting lines shown in the image on the right) across the system (top). When the cheater fraction is larger than the transition value the system does not exhibit a high degree of connectivity and the particles all move in different directions (bottom). (b) The order transition occurs at an f value lower than that required for site or m=3 bootstrap percolation to stop. The average number of like neighbors that each non-cheater has in the ordered state is four or higher.

Mean field approximation of the phase transition

Intuitively, increasing the fraction of non-aligners, f, while keeping the swarm together as a single unit, decreases net alignment with different parts of the swarm trying to go in different directions which results in a disordered stationary state. With cohesive strength being fixed at a high value, the non-aligner carrying capacity, f^*, then depends sensitively

on the ratio, d_v/d_r, where $d_v \sim R$ is the vision radius or agent-spacing and d_r is the reaction distance. Fig. 2.5(D) shows the value of f^* where the system transitions from an ordered to a disordered state (blue) increasing with the ratio d_v/d_r.

To identify the cause for this behavior, we looked at the average magnitude of the alignment interaction, $\alpha\langle|\vec{d}_A|\rangle$, over all agents in the swarm, and the average magnitude of the cohesive interaction, $\epsilon\langle|\vec{d}_{LJ}|\rangle$. As the non-aligner fraction f increases, we found that the average magnitude of the alignment interaction, $\alpha\langle|\vec{d}_A|\rangle$ decreases as the non-aligners do not contribute to alignment and that the transition occurs at a value of $f \sim f^*$ when $\alpha\langle|\vec{d}_A|\rangle$, becomes less than $\epsilon\langle|\vec{d}_{LJ}|\rangle$. Fig. 2.5(D) shows the value of f where the measured value of $\langle|\vec{d}_A|\rangle$ in the simulation becomes less than $\langle|\vec{d}_{LJ}|\rangle$ (green) and we see that it compares well with the measured value f^* for the order disorder transition. Comparing the alignment interaction and cohesive forces as defined in the equations of motion allows us to derive a simple analytic approximation for the value of f^* with no adjustable parameters

$$f^* \sim 1 - C \times \frac{\epsilon}{\alpha}\frac{d_r}{d_v} \tag{2.6}$$

Here, C is a constant set by the form of the cohesive interaction as well as the average number of neighbors per agent (See section 'Analytic approximation for the ordered to disordered state of the system' below for derivation). The agreement between our analytical estimate and the simulation values is shown by the red curve in Fig. 2.5(D).

The fact that f^* changes from about 10% to about 90% in just over a decade in the parameter d_v/d_r is of significance. Higher values of d_v/d_r correspond to situations where agents are spaced much further than they move before updating directions, resulting in agents being able to quickly correct for deviations from their perfect swarming formation. Thus a potential mechanism for swarms to accommodate more non-aligners or malfunctioning agents is to increase d_v/d_r, which can be accomplished either by increasing their separation (increases d_v) or by moving slower and/or processing information more quickly (decreases d_r). The other mechanism to potentially increase the non-aligner carrying capacity f^*, is by reducing the cohesiveness ϵ/α.
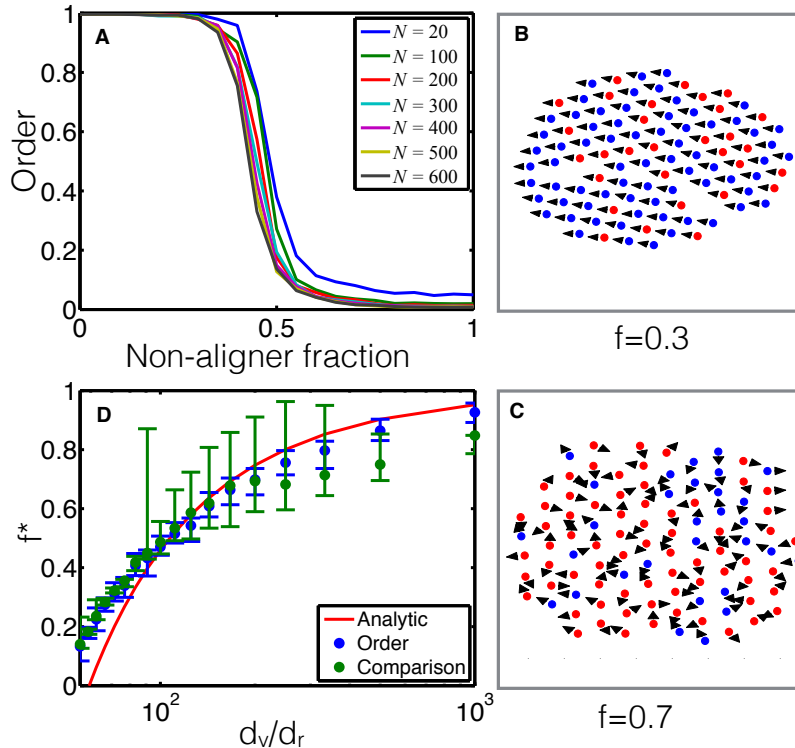
Figure 2.5: (a) Order vs non-aligner fraction of swarms with varying system sizes, $\epsilon = 10^0$. There is a clear transition from an ordered state with $\mathcal{O} \approx 1$ to a disordered state with low $\mathcal{O}$ at non-aligner fractions above a critical value, f^*. (b) Simulation snapshot with a value of f below the critical value, the agents (aligners shown in blue and non-aligners in red) all travel in the same direction (black arrow heads). (c) When the non-aligner fraction is larger than the critical value, the agents try to move in different directions, resulting in a net zero polarization. (d) f^* for the order-disorder transition (blue) as a function of d_v/d_r compared to the non-aligner fraction at which the measured average cohesion becomes greater than that of the average alignment (green). The red curve is the result of our analytical approximation comparing average alignment and cohesiveness.

Tuning cohesiveness between agents allows for enhanced swarming.

Reducing the cohesiveness results in a situation where the disorder is no longer quenched and the agents are able to rearrange themselves within the swarm or allow the swarm to fracture. To study these cases, the system is initialized with a high $\epsilon = 1$ in the *locked-in* state and a high value of $f > f^*$ so that the system is in a static disordered state by default. After a transient time period allowing the system to reach a steady state, ϵ is reduced, allowing for potential rearrangements and fracture. When ϵ is reduced, we found that the system fragments into smaller clusters which can individually be ordered swarming clusters or disordered static clusters. Fig. 2.6(a) shows the weighted average of the steady state order parameter $\mathcal{O}$ of the fragmented clusters of the system for a fixed non-aligner fraction $f = 0.8$ versus the relative strength of the LJ interaction, ϵ, for a system size of $N = 100$. A modest reduction in ϵ appears to have a dramatic effect. When $\epsilon = 10^{-1.0}$

it appears that the polarization in the swarm is greatly amplified where swarming was completely suppressed in the quenched configuration case ($\epsilon \sim 1$). Thus, the previously immobile single cluster has now broken up into smaller clusters, many of which are mobile. As ϵ is decreased further, the polarization begins to decay slightly suggesting that the cohesiveness has become so weak that some of the clusters begin to fracture into individual agents and thus are no longer part of ordered clusters. This suggests that there is some optimal regime of ϵ for collective motion in the presence of non-aligners.

We next probed the dynamics associated with the cluster reorganization. Fig. 2.6(A inset) shows the percent change in the fraction of aligners (blue) and non-aligners (green) which are part of moving clusters as the simulation time progresses. The mobility fraction of non-aligners steadily decreases while the mobility fraction of aligners steadily increases. This suggests a sorting mechanism whereby non-aligners are being left behind allowing for clusters with more aligners to become ordered and move collectively. This can be visualized in Fig. 2.6 (B and C) which illustrates how the system starts out as a single disordered group and then breaks apart into smaller ordered clusters with mixtures of non-aligners and aligners, as well as disordered clusters consisting of mostly non-aligners.

To examine the relative contribution of rearrangements within single clusters to the overall sorting, we measured the probability distribution of the angle between the direction of travel of the non-aligners and the cluster average, as well as the same probability distribution for aligners. We then calculated the difference in these two probability distributions (Fig. 2.6(D)). We observe that aligners contribute predominantly to angles close to zero (purple bar) within the spread due to noise (red shaded region), while non-aligners are more likely to travel at angles around $\pi/2$ (blue bars) with respect to the cluster average. This implies that non-aligners will gradually move towards the sides and backs of the clusters before getting left behind. By sorting out non-aligners, the over all average alignment interaction strength in the cluster increases due to the higher fraction of aligners present, and the smaller cluster is able to swarm.

We now consider the full range of behaviors exhibited by our system as the parameters, including cohesion and non-aligner fraction, are varied. Fig. 2.7 (A) shows a phase diagram of the system in the non-aligner fraction/cohesion (f, ϵ) plane where the colors indicate the value of the order parameter $\mathcal{O}$. We see that if the non-aligner fraction exceeds a critical value $f^*(\epsilon)$ predicted by equation (2.6) (solid white line), the system is in a disordered, *static* state - denoted "St". Here, the cohesive forces dominate over the alignment, leading to the static state with no net order, due to the frustration of agents attempting to travel in differing directions exceeding a value which can be resolved by aligning to reach a consensus direction. Below the line, we see that the system is able to achieve order. There are, however, two very different behaviors within this region. For low values of f, the system is stable and achieves a high degree of polarization ($\mathcal{O} \sim 1$) as a *single* cohesive swarm, relieving frustration by aligning to reach a consensus direction. This is clearly shown by the *swarming* region labelled "Sw" in Fig. 2.7(B) where the colors now indicate the probability that the system fractures into two or more clusters. Now, as the non-aligner fraction is increased, we enter the sorting regime ("So") that we examined earlier in this section, where the system begins to fracture into smaller clusters, leaving behind non-aligner rich clusters, allowing aligner rich clusters to swarm and thereby increasing the net polarization. It is of interest to note here that the transition between the swarming and sorting phases roughly occurs at a constant value of the non-aligner fraction, f^c equal to the critical non-aligner fraction, f^*, when the alignment and cohesion constants become equal, $\epsilon = 1$ (in

units of α), which is shown by the dashed white line, suggesting that at non-aligner fractions above f^c frustration within the system is relieved by fracture as well as alignment. The existence of these three regimes and their locations relative to the predicted transition lines turn out to be completely general and work over the range values of d_v/d_r feasible in our simulations with no adjustable parameters (see Additional results and discussion - Phase diagrams section below).
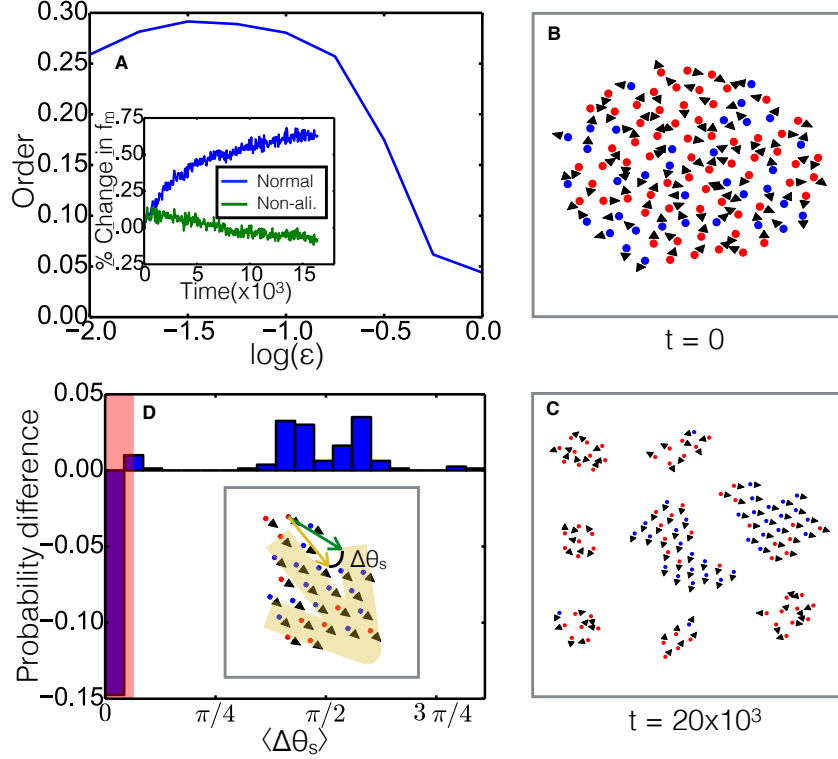
Figure 2.6: (A) The weighted average steady state order of all clusters against ϵ, for a fixed value of non-aligner fraction, $f = 0.8$ and system size of $N = 100$. (A inset) Plot of the percent change in mobility fraction for aligners and non-aligners against time after the initial transient phase with fixed $\epsilon = 10^{-1}$ and $f = 0.8$. (B) At values of non-aligner fractions near the transition the system sorts from one single swarm without any order, to (C) smaller clusters with ordered clusters and disordered clusters. Separation shown between clusters in (C) is chosen for convenience and is much smaller than the actual separations by the end of the simulation (clusters are shown to scale but their relative positions are not). (D) Difference in the probability distribution of the angle between the direction of travel of non-aligners from the average cluster direction and the direction of aligners from the average cluster direction. Red shaded region is the angles which are within the range of the noise of the system.

Self-organized sorting.
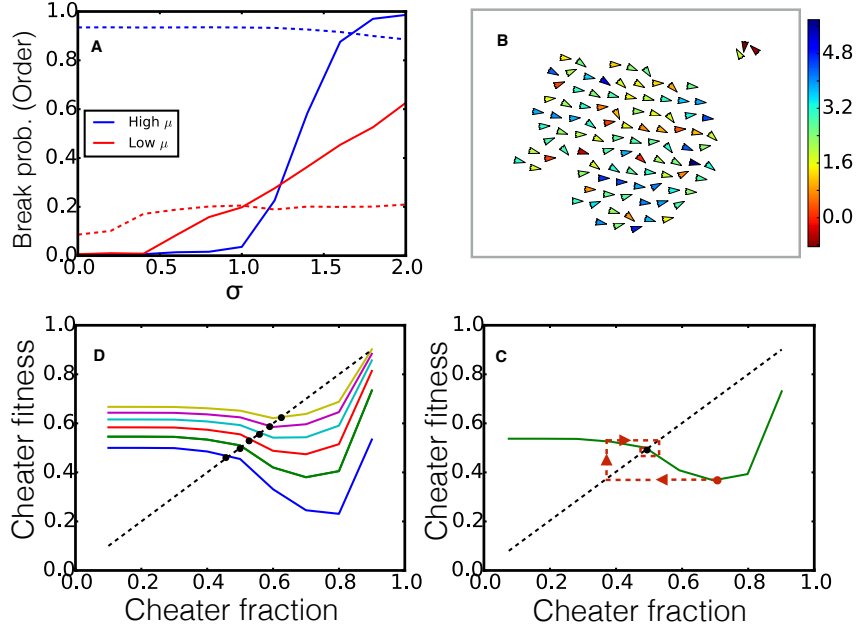
Figure 2.7: (A) The order parameter of the system with $d_v/d_r = 100$ plotted by color against ϵ and f. (B) The probability of the system fracturing into two or more clusters plotted against ϵ and f. The three phases, swarming (Sw), sorting (So), and static (St) are labeled on the phase diagram, with the predicted ordering transition (from equation (2.6)) as a solid white line and the dashed white line corresponding to the critical non-aligner fraction at $\epsilon = 1$. (C) The non-aligner fraction within small clusters which are ordered in steady state vs. the initial non-aligner fraction f, with $N = 100$, and $\epsilon = 10^{-0.5}, 10^{-1.0}, 10^{-1.5}$, and $10^{-2.0}$, corresponding to the blue, green, red, and black curves respectively. The dashed green line shows the value of $f^* = 0.5$ with $d_v/d_r = 100$. The purple curve corresponds to $f^* = 0.75$, purple horizontal dashed line, with $d_v/d_r = 200$, and $\epsilon = 10^{-1.0}$. The yellow curve corresponds to $f^* = 0.3$, yellow horizontal dashed line, with $d_v/d_r = 67$, and $\epsilon = 10^{-1.0}$. The light blue line shows the non-aligner fraction in the system if it were unable to fracture. (C inset) The fraction of the system that is in ordered clusters for $N = 500$. (D) The spread of non-aligner fractions within the sorted swarming clusters for several different systems sizes. The shaded area shown for each system size represents the average $\pm$ one standard deviation, for final cluster sizes in bins of size 10. Green dashed line as in (C).

Starting with a cluster with a high non-aligner fraction, we showed that, for low enough cohesive energies, the swarm dynamics spontaneously cause the re-organization and break-up of the cluster. What, then, is the non-aligner fraction of the sub-clusters that are now mobile and able to swarm? To answer this question, we looked more closely at the fragmented clusters and measured the average non-aligner fraction of all swarming clusters which have $\mathcal{O} > 0.9$. Fig. 2.7 (C) shows the final fraction of non-aligners averaged over all swarming sub-clusters as a function of the initial non-aligner fraction in the system, for

three different values of f^c of $\sim 0.3, 0.52,$ and, 0.75, which is set by changing the value of d_v/d_r according to Fig. 2.5(D). For low values of the initial non-aligner fraction, f, the final non-aligner fraction appears to follow linearly with a slope of unity, implying that little sorting or fracturing occurs for low non-aligner fractions. This is as expected, since for non-aligner fractions below the transition for a single crystallized swarm, at f^c, are within the "Sw" region of the phase diagram in Fig. 2.7(A, B), and no fracturing is necessary to relieve frustrations within the system.

Then, as the initial non-aligner fraction continues to increase and approach $f \approx f^c$, we enter a region where the final non-aligner fraction seems to level off. In this regime, the value of f is high enough that, if the cohesiveness, ϵ, were very high (> 1), the system would be in a frustrated state with no overall alignment and different agents trying to go in different directions but being held together. But since the cohesiveness is actually low, the frustration can be relieved by the cluster fragmenting into smaller pieces that can have a net alignment. The same logic holds for resulting smaller clusters that still have too high of a non-aligner fraction f - and they will continue to fragment. If a resulting cluster has a non-aligner fraction less than $\sim f^c$, it is within the "Sw" region of the phase diagram in Fig. 2.7(A, B), so it can move collectively by reaching a consensus direction to relieve frustrations without fragmenting further. Thus the aligners have effectively self-organized into small clusters with an average non-aligner fraction close to the critical value f^c. This picture is confirmed by Fig. 2.7(C inset) which shows the fraction of the system which is contained in ordered moving clusters. For low initial non-aligner fractions, almost the entire cluster is mobile, while beyond the critical non-aligner fraction, the mobility fraction decays linearly as predicted by the simple picture where non-aligners in excess of the critical fraction f^c are simply left behind.

To examine how robust our results are, and, in particular, if they are sensitive to the initial system size, we fix ϵ and the non-aligner fraction at $\epsilon = 10^{-1.0}$, and $f = 0.8$, and examined the final swarming clusters for a range of initial system sizes. We also measured the spread of non-aligner fractions within final clusters of different sizes, again for a few systems sizes. Fig. 2.7(D) shows the average $\pm$ standard-deviation of the non-aligner fraction over the different final cluster sizes. We can see that both the average non-aligner fraction and its variance within the final clusters are fairly independent of initial system size.

One can now imagine a generic swarm where the fraction of non-aligners (or defective/diseased agents) increases over time. This could be due to the spreading of a disease among organisms or the breakdown/malfunctioning over time of individual robotic agents, or simply the tendency of entropy to increase. As time goes on, the system will reach a state where the fraction of non-aligners exceeds the critical fraction, f^c, thus entering the sorting regime, if the cohesive forces are in the right regime. Our results indicate that the system can then shed almost the entire excess non-aligner population (above the critical threshold) and revert to a fraction close to but just below f^c. Then as the system evolves again over time the non-aligner fraction increases past the threshold and the process begins again. Thus, dynamical sorting can compete against natural processes that drive increases in the non-aligner fraction and provide a mechanism for the system to reach a dynamic equilibrium, regulating its composition so that it sits at the edge of criticality in behavior; reminiscent of a self-organized critical system.

Swarms with a distribution of alignment behaviors.

So far, we have considered behavioral variability to be binary in character with agents being either aligning or non-aligning ($\alpha = 1, 0$). It is, however, quite reasonable to expect that many naturally occurring swarms might display a spectrum of behaviors that corresponds to natural abilities differing from individual to individual. We showed before that the phase behavior of the swarm is controlled by the mean level of alignment as compared to cohesion. Here we consider what happens if, instead of changing the mean level of alignment accomplished by changing the fraction of non-aligners in a binary system, we keep the mean value fixed and change the spread in a system with continuous values of the alignment interaction strength α. To implement this, we selected α for each agent from a Gaussian distribution with mean, μ, and standard deviation, σ. We consider two types of systems, one with a high value of μ that would result in an ordered swarming system in the $\sigma = 0$ case and one with a low value of μ which would result in a static system with $\sigma = 0$. Keeping these two values of μ fixed, we vary the spread σ.

Fig. 2.8 (A) shows both the low μ (blue) and high μ (red) cases and we can see that as σ increases there exists a critical threshold, σ_c, beyond which the system will be likely to fracture (solid lines show probability of fracture), however the reason for fracture is different in both cases. The average order parameter (dashed line) for the high μ case starts out high and as σ increases and fracture begins to occur, the order decreases slightly because some individuals now have a low enough α that they behave like non-aligners and break off of the main body of swarmers to form static clusters. In the case where μ is low the system has very low order at low σ and as the spread of α values increases the system begins to fracture and the average order increases. In this case some agents are reaching high enough α values to form an ordered state and will create clusters of ordered moving agents which break off from or fragment the static main body of agents. Fig. 2.8(B) shows a snapshot from the simulation that started off as one swarming cluster. Here σ is high enough to allow fracture resulting in the sorting out of a smaller, static cluster of agents with a predominantly low value of α. Thus the increase in the spread of α has similar consequences whether one starts with a high or low average α. There is a self-organized separation of the population leading to clusters of similar "phenotype" providing a mechanism for a natural limitation to the extent of variability in any swarming population.

Evolving populations.

We now examine the idea that dynamical sorting could be a mechanism for *evolving* swarms to robustly sustain a certain composition over longer timescales. For swarms, over sufficiently long timescales, one could imagine that the non-aligner population fraction increases due to some fitness advantage that the non-aligners derive by not participating in orientational information processing. For example, in [30], an agents ability to decide on a preferred travel direction due to social interactions or migratory tendency is assumed to come at some cost due to energy expenditure or reduced predator awareness during directional information processing. In this case the non-aligners would be cheaters in the evolutionary sense which can lead to some interesting dynamics. To model the evolutionary dynamics we considered a model replicator system [59] where agents replicate themselves at a rate that is determined by their fitness, with the fitter species (cheater or non-cheater) being able to reproduce more quickly and increasing its proportion in the population over

time. The assigned fitness of an individual agent depends on whether an agent is a cheater and whether it is in a swarming cluster. We take the fitness of an agent i at any point in time to be given by,

$$\mathcal{F}_i = \phi_{\mathcal{O}} \times \mathcal{O}_{cl} + \phi_c \times \sigma_i \tag{2.7}$$

Here, $\mathcal{O}_{cl}$ is the polarization of the cluster that agent i belongs to, $\phi_{\mathcal{O}}$ represents the fitness advantage that agents gain by being in ordered clusters and ϕ_c is the fitness advantage gained by cheating agents (say by avoiding energy expenditures associated with orientational processing or signaling) and σ_i is equated to 0 for non-cheaters and 1 for cheaters. These fitness advantages are similar qualitatively to those postulated to study evolution in migratory populations where there were costs associated with obtaining directional cues from the environment and an overall fitness associated with migrating close to the desired direction [30, 60, 61]. We start with a system of $N = 500$ agents with $\epsilon = 10^{-0.5}$ with periodic boundary conditions at different total cheater fractions. For each simulation, the system is allowed to evolve until a steady state is reached and the relative fitness of all cheaters, $\mathcal{F}_{rel}$, given by

$$\mathcal{F}_{rel} = \frac{\langle \mathcal{F}_{ch} \rangle_t}{\langle \mathcal{F}_{nc} \rangle_t + \langle \mathcal{F}_{ch} \rangle_t} \tag{2.8}$$

is measured. Here $\langle \mathcal{F}_{ch/nc} \rangle_t$ is the time averaged fitness of all cheaters/non-cheaters given by Eq 2.7. As an example, fig. 2.8(A) shows how the relative fitness of cheaters $\mathcal{F}_{rel}$ varies with cheater fraction for the ratio of fitness advantage constants $\Phi = \phi_c/\phi_{\mathcal{O}} = 0.2$. In our evolutionary dynamics, we take the relative fitness of all cheaters, $\mathcal{F}_{rel}$, to be the expected fraction of cheaters in the subsequent generation. The red dashed line in fig. 2.8(A) shows a typical evolutionary trajectory. Here, a population that starts with a cheater fraction $f = 0.7$ has $\mathcal{F}_{rel} \sim 0.39$ which results in a cheater fraction $f \sim 0.39$ in the subsequent generation which has $\mathcal{F}_{rel} \sim 0.55$ and so on. A fixed point at which the initial cheater fraction is equal to that in the next generation is then given by the intersection between the curve and the diagonal (black dot in fig. 2.8(A)). An evolutionarily stable fixed point is obtained when a fixed point is an attractor of all evolutionary trajectories, as is the case here. Fig. 2.8(B) shows how the relative fitness of cheaters $\mathcal{F}_{rel}$ varies with cheater fraction for several different values of the ratio of fitness advantage constants Φ. We observe a unique stable fixed point for each value of Φ, that increases with Φ, suggesting that in any system where both cheating and swarming are advantageous, competing pressures can result in stable populations of cheaters that are dynamically regulated by self-organized sorting.
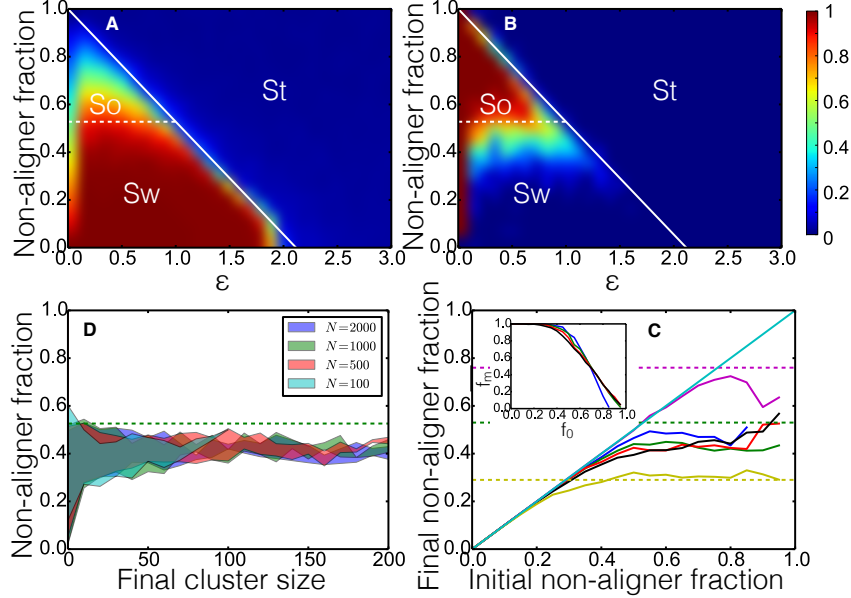
Figure 2.8: (A) Probability of fracture (solid), and order parameter (dashed) plotted against σ for a high value of $\mu = 2.5$(blue) and a low value of $\mu = 0.5$(red). (B) Snapshot from a simulation with $\mu = 2.5$, and $\sigma = 1.2$ showing fragments of a larger cluster that has sorted itself into an ordered cluster with a higher mean α and static, disordered cluster with $\alpha \sim 0$ for most agents. Arrowheads signify direction of motion, and the color bar shows the value of α for each individual agent. (C) The relative fitness of all cheaters, $\mathcal{F}_{rel}$, as a function of cheater fraction, f for $\Phi = 0.2$. The point where the dashed diagonal line crosses the fitness curve is a fixed point where the cheater fraction and fitness of the system become equal representing an equilibrium fixed point for the evolutionary dynamics. Red dashed line shows an example trajectory an evolving system would follow starting at $f = 0.7$ and approaching the fixed point after several generations. (D) The relative fitness of all cheaters, $\mathcal{F}_{rel}$, in the system as a function of cheater fraction for different values of the ratio of fitness advantage constants $\Phi = \phi_c/\phi_{\mathcal{O}} = 0, 0.2, 0.4, 0.6, 0.8$, and 1 corresponding to the blue, green, red, cyan, purple and yellow lines respectively. The points were the dashed diagonal line crosses the fitness curves are evolutionary fixed points. For this system $N = 500$, $d_v/d_r = 100$, and $\epsilon = 10^{-0.5}$.

2.1.3   Methods

Individual's behavior

In this section we discuss the details of the behavior of each individual. Particles were initialized with random positions and directions within a circle of radius d_v, or the vision radius of particles. Then directions are updated according to Eq. 2.1.

$$\vec{x}_i(t + \Delta t) = \vec{x}_i(t) + d_r \hat{d}_i \Delta t \tag{2.9}$$

The alignment and cohesiveness interactions are given in Eq. 2.10 and Eq. 2.11

α	1	r	0.7887	N	20 - 600
R	1	d_r	0.01	f	0 - 1
Δt	1	η	0 - 1	ϵ	$10^{-3} - 10^0$

Table 2.1: Parameters

respectively where n.n. signifies all neighbors within a vision radius of $d_v = 1$, including itself for the alignment interaction, but not including itself for the Lennard-Jones interaction.

$$\vec{d}_A = \sum_j^{n.n.} \vec{v}_j(t) \tag{2.10}$$

$$\vec{d}_{LJ} = -12 \sum_j^{n.n.} \left(\frac{R^{13}}{s_{ij}^{13}} - \frac{R^7}{s_{ij}^7} \right) \hat{s}_{ij} \tag{2.11}$$

We set $\alpha = 1$ to set the scale for interaction strengths so that we can vary ϵ in units of α. We also set $R = 0.7887$, which allows for each particle to see on average their first nearest neighbors when the system has reached equilibrium. $\hat{s}_{ij}$ is a unit vector pointing between the ith and j^{th} particles and s_{ij} is the distance separating them. New positions are then calculated for each particle according to Eq. 2.9, where d_r is the reaction distance of each particle and held constant across the swarm at $d_r = 0.01$, i.e. over damped dynamics. In real systems the value of d_r can be determined from the speed of agents motion and the reaction time of the agents, vt_r, and therefore can be varied for specific systems by varying either of these quantities as well. The simulation time step, which for this model is equivalent to the reaction time, is set to $\Delta t = 1$, though varying the simulation time step while holding the reaction time constant does not effect the results presented. Individuals also have some physical limitations in the form of an angular noise which is added to the calculated direction of travel. This noise is set to $\eta = 0.2$ and a random angle is selected from $[-\eta/2, \eta/2]$ and added to the new direction. Simulations were run for 10^5 time steps, and data was averaged over 200 samples.

Additional results and discussion

Initial density and simulation timestep dependence.

Varying the initial number of agents per unit area (d_v^{-2}) has very little effect on the resulting phase transitions over a wide range as shown in Fig. 2.9(a) where ρ_0 is the agent initial density. The simulation time step also has very little effect on the system dynamics as can be seen in Fig. 2.9(b). Note that this time step (Δt is the simulation time step and not the processing time for interactions (δt).
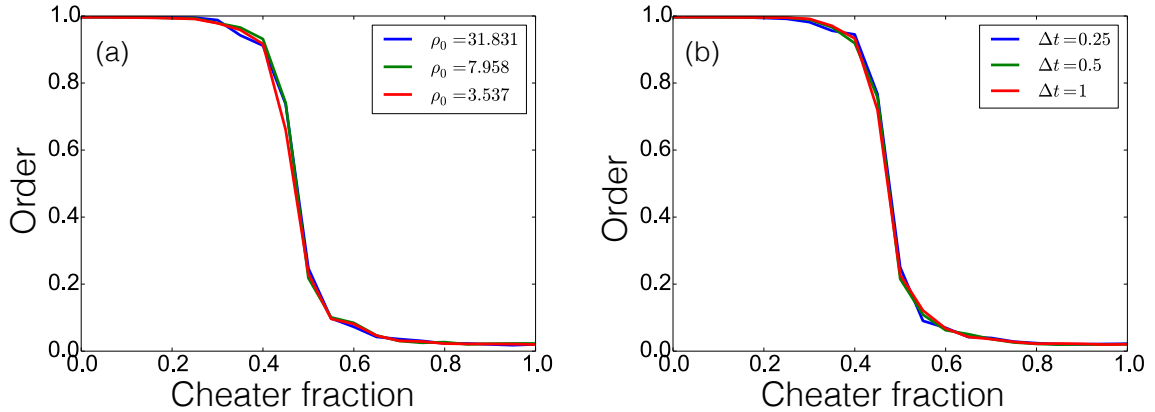
Figure 2.9: The order transition for the system with non-aligner fraction for varying initial system density (a), and simulation time step (b).

Sorting

To examine the amount of rearrangement that is taking place within the swarm when the cohesiveness is reduced we measured the amount of sorting that is taking place according to Eq. 2.12. This is the fraction of neighbor pairs within the whole system which are of the same type (like-like neighbor pairs) at time t, normalized by the fraction of like-like neighbor pairs at the initial time. This allows us to look at how the system is rearranging to put particles of the same type next to each other as the simulation evolves through time.

$$S(t) = \frac{n.n._{same}/n.n.(t)}{(n.n._{same}/n.n.)_0} \tag{2.12}$$
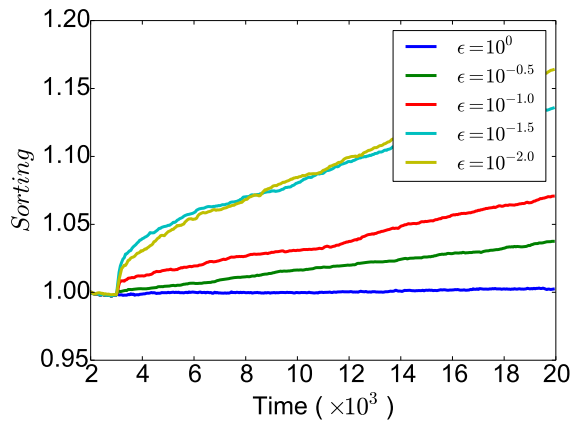
Figure 2.10: The system rearranges with time causing agents to have more neighbors of the same type as themselves resulting in an increase in the sorting measurement.

Analytic approximation for the ordered or disordered state of the system

We found that the average magnitude of the alignment interaction on any agent chosen at random, must be greater than the average magnitude of the Lennard-Jones interaction in order for the system to be ordered, satisfying the inequality in Eq. 2.13.

$$\langle A \rangle_i > \langle LJ \rangle_i \tag{2.13}$$

The average magnitude of the alignment interaction is the chance of an agent, chosen at random, being a aligner, $(1 - f)$, multiplied by the number of agents it is interacting with, n, and the alignment interaction strength, α, as seen in the left hand side of Eq. 2.14. The average magnitude of the Lennard-Jones interaction is due to the fluctuations of each agent (regardless of whether it is a non-aligner or not) around the bottom of the potential well that it is in. In any time step an agent can move a distance up to d_r away from the bottom of the well, resulting in a Lennard-Jones force (of the form given in Eq. 2.3) at a separation of $R - d_r$ on average from each of it's n neighbors, as seen in the right hand side of Eq. 2.14. However, due to the fact that the n Lennard-Jones forces acting on an agent from each neighbor will point in effectively random directions, and the average magnitude of the Lennard-Jones force on the agent will be equivalent to the root mean squared distance travelled by a classic 2D random walk with n steps, resulting in the factor of $\sqrt{n}$.

$$(1 - f)n\alpha > \sqrt{n}\epsilon \times 12 \Big[\frac{R^{13}}{(R - d_r)^{13}} - \frac{R^7}{(R - d_r)^7} \Big] \tag{2.14}$$

$$(1 - f)n\alpha > \sqrt{n}\epsilon \times 12 \Big[\frac{1}{(1 - d_r/R)^{13}} - \frac{1}{(1 - d_r/R)^7} \Big]$$

$$(1-f)n\alpha > \sqrt{n}\epsilon \times 12 \Big[\Big(1 + \frac{12}{1!}d_r/R + \frac{12 \times 13}{2!}(d_r/R)^2 + ... \Big) - \Big(1 + \frac{6}{1!}d_r/R + \frac{6 \times 7}{2!}(d_r/R)^2 + ... \Big) \Big]$$

Since d_r/R is small we can drop higher-order terms.

$$\frac{\alpha(1 - f)}{\epsilon} > \frac{12}{\sqrt{n}}[6d_r/R]$$

Ignoring defects and considering the mostly hexagonal lattice of agents in our system, we take the coordination number to be $n = 6$ and find

$$\frac{\alpha(1 - f)}{\epsilon} > 12\sqrt{6}\frac{d_r}{R}$$

From this result we have a simple linear relationship between interaction energy scales (α, ϵ) and physical system parameters $(d_r, R(d_v))$, which we can use the predict the value of f^*,

$$f^* = 1 - \frac{12\sqrt{6}}{0.8}\frac{\epsilon}{\alpha}\frac{d_r}{d_v} \tag{2.15}$$

where the average magnitude of the alignment interaction and the average magnitude of the Lennard-Jones interaction within the system become equal and the order disorder transition occurs.

Phase diagrams

The analytic prediction of the phases of the system holds for a wide range of parameters feasible in our simulations. Fig. 2.10 shows the three phases (swarming "Sw", static "St", and sorting "So") shown in the (f,ϵ) plane for three values of $d_v/d_r = 67, 100,$ and 200. The predicted transition lines are derived from Eq. 2.15 (solid white line), and the calculation of f^c, the critical non-aligner fraction, f^*, when $\epsilon = 1$ (dashed white line), and are accurate over a wide range of d_v/d_r as shown.
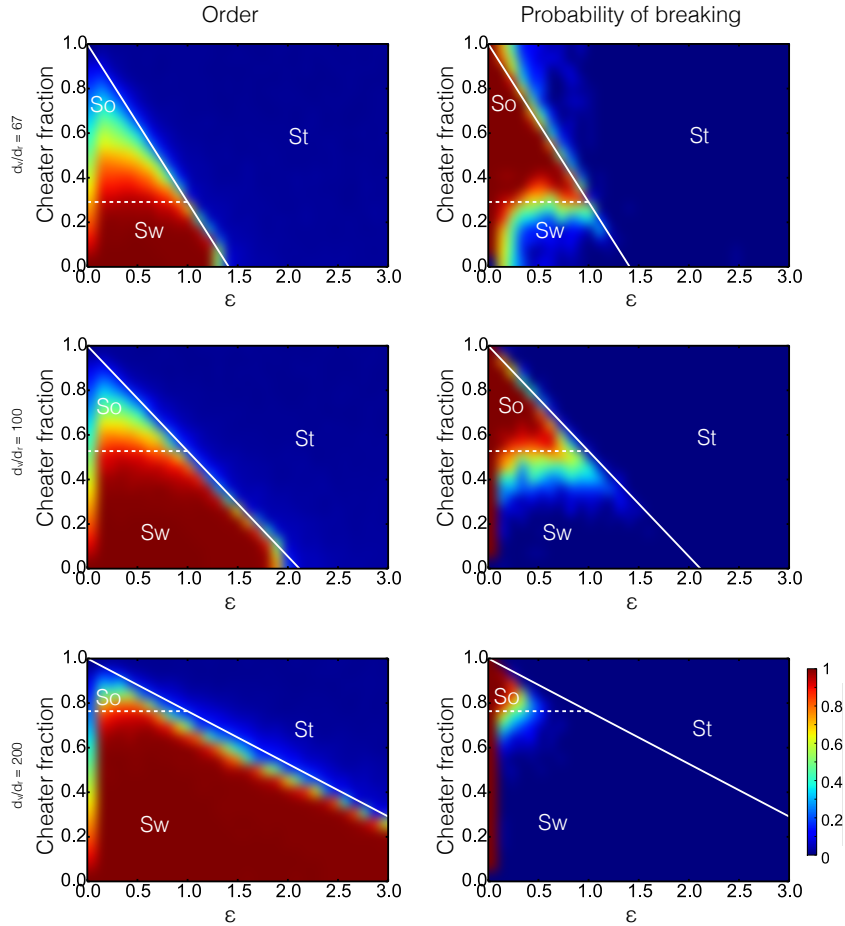
Figure 2.11: The phase diagram for the system with the analytically derived phase boundaries for three values of $d_v/d_r = 67, 100,$ and 200.

Determining Interaction Strengths from Separation Measurements

The value of ϵ can be inferred by looking at how well crystalized and solid the swarm is and hence how regular the spacing between agents is. Therefore in an ordered swarm, a lower value of ϵ will result in a larger variance in agent-agent separation. In the case where ϵ is increased above the swarming threshold (see Fig. 3(a)) the dynamics of the swarm are dominated by random agent motion around the potential minimum due to the active forces exerted by agents and the relationship between ϵ and separation variance no longer holds.

Fig. 2.12 shows the variation in separation plotted against ϵ for several values of d_v/d_r, within the ordered regime, which can be directly measured in a given swarm and a clear relationship between increasing ϵ and decreasing separation variance can be seen, allowing for ϵ to be extracted from direct swarm measurements in natural systems.

Figure 2.12: Variance of the separation between each agent and it's neighbors plotted against ϵ.

2.1.4 Discussion

Within a group of swarming or flocking animals there may exist intrinsic behavioral heterogeneities that can effect the ability of the group to remain cohesive and move collectively. Behavioral differences can arise from natural individual variations, diseases or genetic mutations that occur randomly as the group of animals produces progeny. In artificial systems, such as robotic drones, 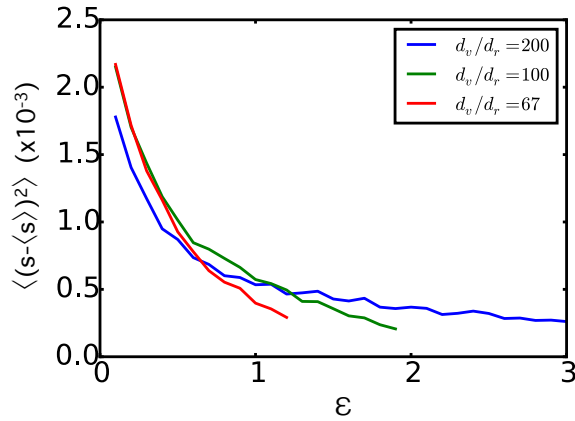differences can manifest as malfunctioning hardware or compromised software. In natural systems, therefore, it seems likely that there could exist collective mechanisms that allow the whole group to carry a subgroup of individuals that do not participate collective decision making (i.e non-aligners or cheaters).

We studied a system of swarming agents that display individual variations in their alignment strength. For the binary case of mixtures of aligners and non-aligners, we found that when the cohesion is strong, there is a critical fraction of non-aligners f^* above which collective motion of the whole group can no longer be achieved. We call this critical non-aligner fraction, the maximum non-aligner carrying capacity. We showed that there is a simple predictive relation between the maximum non-aligner carrying capacity and the length and interaction strength scales that characterize the swarm. We showed that swarms can increase their non-aligner carrying capacity f^* by increasing the separation between agents, moving slower and/or processing information more quickly. These simple robust mechanisms could allow for a swarm or flock to adapt to increased non-aligner loads "on the fly" and our results also suggest optimal designs of parameters for "non-aligner tolerant" artificial swarms.

Alternatively, we found swarming could be enhanced in an unusual manner by lowering the cohesive attraction between agents. We showed that, as cohesion is lowered, there exists a regime where the clusters can actively sort out and leave behind the excess non-aligning population. We find that the newly sorted clusters that emerge after segregating are capable

of swarming and carry a fraction of non-aligners that is near a fixed critical non-aligner carrying capacity that we are able to predict from measurable swarm parameters. Thus the dynamics of the swarm naturally weeds out non-aligners above the critical capacity and maintains the non-aligner fraction in the swarm close to this value, reminiscent of a self-organized critical behavior. This result highlights a simple, robust and efficient mechanism that allows heterogeneously mixed populations to naturally regulate their composition and remain in a collective swarming state despite the natural tendency for cheating/diseased/defective population fractions to increase.

It is to be noted that lowering the value of cohesiveness too much can also lead to deleterious effects with the swarming clusters unable to hold themselves together. This suggests that, if such a sorting and segregation mechanism is utilized in nature, the relative magnitudes of cohesiveness and orientational alignment need to be tuned to lie within an optimal range. It is also interesting to note that though we considered cheaters or defective agents as having a negative effect on swarming, one could also consider situations where a swarm needed to break up or segregate between two populations. Our results indicate that a simple mechanism to achieve this would be for one group to simply become "non-aligners" and allow the swarm dynamics to automatically segregate and expel them from the swarm.

It is to be noted that we were able to map out the entire phase space of behaviors in these heterogeneous systems including swarming, static and sorting phases and relate them to simple relations between the swarm parameters. Furthermore, these swarm parameters can be directly observed or inferred from measurements of real swarms (see Supplementary Information 4). Thus our results provide us with predictive power about real swarms including their maximum non-aligner carrying capacity, their ability to sort and the critical non-aligner fraction that sorting leads to. It is also intriguing in this context that if there is a natural tendency for non-aligners to increase, we would expect to measure, in a real swarm, a composition of non-aligners close to a critical fraction that we can predict based on measurable swarm parameters.

We were also able to show that our notions of sorting extend to swarms with a continuous distribution of individual alignment preferences. In fact, the existence of outliers, whether they were non-aligners or "super-aligners" or both triggered the sorting process. This is suggestive of a natural means of separating different types of behavior which could have implications not only for limiting variability in populations but also more generally for the division of labor in collectively moving systems.

Finally, we pursued the idea of competing cheating and sorting by considering the evolutionary dynamics of a replicator system, where there was a fitness advantage associated with being in a collectively moving swarm and an advantage for being a cheater. We showed that the system has a globally stable evolutionary fixed point corresponding to a particular fraction of cheaters that is set by relative fitness advantage of cheating and the swarm parameters. It is interesting to note that evolutionary equilibria between successful strategies can thus be tuned by changing the physical parameters of the swarm. Our work therefore makes connections to studies of evolutionary dynamics in structured populations and networks [62, 63] and specifically to work that shows that both network structure [64] and its dynamics [65] can influence the success of cheating or defection. In the broadest sense, our results suggests the idea that the spread of a non-aligner/defector/cheater strategy within a population beyond a critical threshold can spontaneously trigger large-scale re-organization of the collective that expels outliers and effectively limits the spread of behavioral variability.

2.2 Noise heterogeneity

Collective motion is a phenomenon that exists in nature across a wide range of length scales from actin fibers within cells to bacteria [7], bird flocks [2], and crowds of people [15]. Artificial collective motion has more recently emerged in the form of active colloids, drone swarms and simulations. The mechanism for propulsion and interaction between agents varies widely from system to system, but there are common collective behaviors that are carried over between systems. Natural systems such as birds, fish, bacteria, and cells often show some polar order on length scales longer than that of the individual constituents, which can also be a desireable feature in drone flocks, and has been recreated in synthetic swarms of actin fiber active nematics, and colloidal systems. Other systems that can show collective motion may not necessarily align into ordered flocks, such as fly swarms, and isotropic active colloids. Several simple models exist that can simulate these collective motion systems and have been used to shed light on many of the behaviors seen.

Pairwise interactions and noise are two key components of agent based models that lead to many collective behaviors, including milling in fish schools, flocking birds, swarming flies, and colloidal clustering. At sufficiently low noise and high density, most agent based swarming models show a highly polarized flocking phase, and increasing noise drives a transition into a disordered isotropic phase, the nature of this transition depends on the details of noise implementation. Typical pairwise interactions include some form of alignment interaction and a distance dependent attractive / repulsive or volume exluding interaction, both of which can be either physical or cognitive. Physical interactions are associated with collisions or adhesions between agents or reorientations driven by contact between agents, such as cells or colloids bumping into eachother and forming adhesions. Physical alignment interactions exist in rod shaped bacteria or active colloids which align by pushing against eachother, while cognitive alignment occurs in flocks of birds, schools of fish or crowds of people where agents have a preference to travel in the average direction of their neighbors, and cognitive cohesive interactions occur between birds or fish which adjust their orientation to maintain some desired spacing. From a modeling perspective, cognitive interactions effect the well defined direction in which agents propel themselves while physical interactions are treated separately from propulsion and affect the actual motion of the agents.

In natural systems, the amount of noise, or rotational diffusivity, may vary from individual to individual, as seen in bacteria with mutations, malfunctioning drones, and manufacturing errors in colloids. In simulations, collective motion is generally studied in a very controlled consistent environments with identical agents accross the system. What happens to the collective behaviors of systems with mixtures of high and low noise agents, and under what conditions can a system stay as a single cohesive unit? What are the effects of physical vs. cognitive interactions on a systems ability to tolerate heterogeneity in noise level?

To answer these questions we adapt popular swarming models from the literature to examine finite sized clusters of swarming agents with noise heterogeneity, and combinations of both physical and cognitive alignment and cohesive interactions. We find that in all cases there exist four general phases of motion, a cohesive disordered cluster similar to a crystal or liquid, a single flock of cohesive polarly aligned cluster similar to a flying crystal or bird flock, and two fracturing states consisting either of a gas of individual agents, or small polarly ordered clusters. Unsurprisingly, an increase in noise is associated with loss

of polar order, while an increase in cohesive interaction strength results in a decrease in cluster fracture. We also find that noise levels above the order disorder transition suppress cluster fracture as it will be in stationary liquid- or solid-like states, with no polar order, rather than lower noise where locally ordered domains form and pull apart the swarm even in the presence of higher cohesive interaction strength.

With mixed populations we find that when alignment is driven by physical collisions, the system is able to remain ordered with a higher fraction of noisy individuals at higher cohesive interaction strengths, while the opposite is true for cognitive alignment interactions where the cohesive and alignment interactions are more competitive than cooperative as in the physical alignment model.

In this section we compare several swarming models and the effects of hetergeneous populations with variable noise levels. We discuss the similar behaviors that are seen in all models as well as some of the differences between model choices and the behaviors that these differences highlight in natural systems. Providing strategies for model selection as well as properties that hold across models.

2.2.1 Model

In order to understand the effects of heterogeneous populations, for several different models, all agents are initialized as a single cohesive unit and they interact according to the following general equations of motion:

$$\dot{\vec{x}}_i = \vec{F}_i \tag{2.16}$$

Where $\vec{x}_i$ is the position of agent i with respect to a common origin and $\vec{F}_i$ are the forces acting on it. The agent motion is overdamped in continuous two dimensional space which is why the force is equated to velocity. The forces that act on each agent originate from the self propulsion of the agent as well as any physical interactions as shown in eq. 2.17.

$$\vec{F}_i = v\frac{\vec{d_i}}{|\vec{d_i}|} + k\vec{P}_i \tag{2.17}$$

Here, v is the strength of self propulsion compared to k, the strength of the physical forces. $\vec{d_i}$ is the direction of self propulsion and $\vec{P}_i$ are any physical forces acting on the agent by neighboring agents. The forms of $\vec{d_i}$ and $\vec{P}_i$ depend on the model specifics and are presented below for each model studied. All models presented here utilize a Lennard-Jones force as the cohesive interaction shown in eq. 2.3 for the pair of agents i and j.

$$\vec{LJ}_{ij} = -12\Big(\frac{R^{12}}{s_{ij}^{13}} - \frac{R^6}{s_{ij}^7}\Big)\frac{\vec{s}_{ij}}{|\vec{s}_{ij}|} \tag{2.18}$$

Here, R is the equilibrium separation between agents and $\vec{s}_{ij} = \vec{x}_j - \vec{x}_i$ is a vector connecting the centers of agent i and j. Agents are all initialized as a cohesive unit and then allowed to move freely with no boundaries for $\sim 10^6$ timesteps and the final state of the system is then analyzed.

The group polarization of the system is taken as the weighted average of all clusters (with greater than 1 agents) of the order parameter shown in eq. 2.19.

$$\mathcal{O} = \frac{1}{N} \sum_{i=0}^{N} \dot{\vec{x_i}} / |\dot{\vec{x_i}}| \tag{2.19}$$

Simulations are run for ten samples and the largest cluster size for each sample is averaged ($\mathcal{N}$) to examine the amount of fracture occuring in the system, the average largest cluster size is also normalized by the total system size. So the value of $\mathcal{N}$ will be 1 if the system does not fracture and close to 0 for a system that fragments into individual agents. The system can be classified into one of four phases: 1. A flock with high $\mathcal{O}$ and high $\mathcal{N}$, 2. Stationary swarm with low $\mathcal{O}$ and high $\mathcal{N}$, 3. Fragmented flock with high $\mathcal{O}$ and low $\mathcal{N}$, or 4. A gas with low $\mathcal{O}$ and low $\mathcal{N}$. These four phases are illustrated in Fig. 2.13, (A, B, C, and D) respectively.
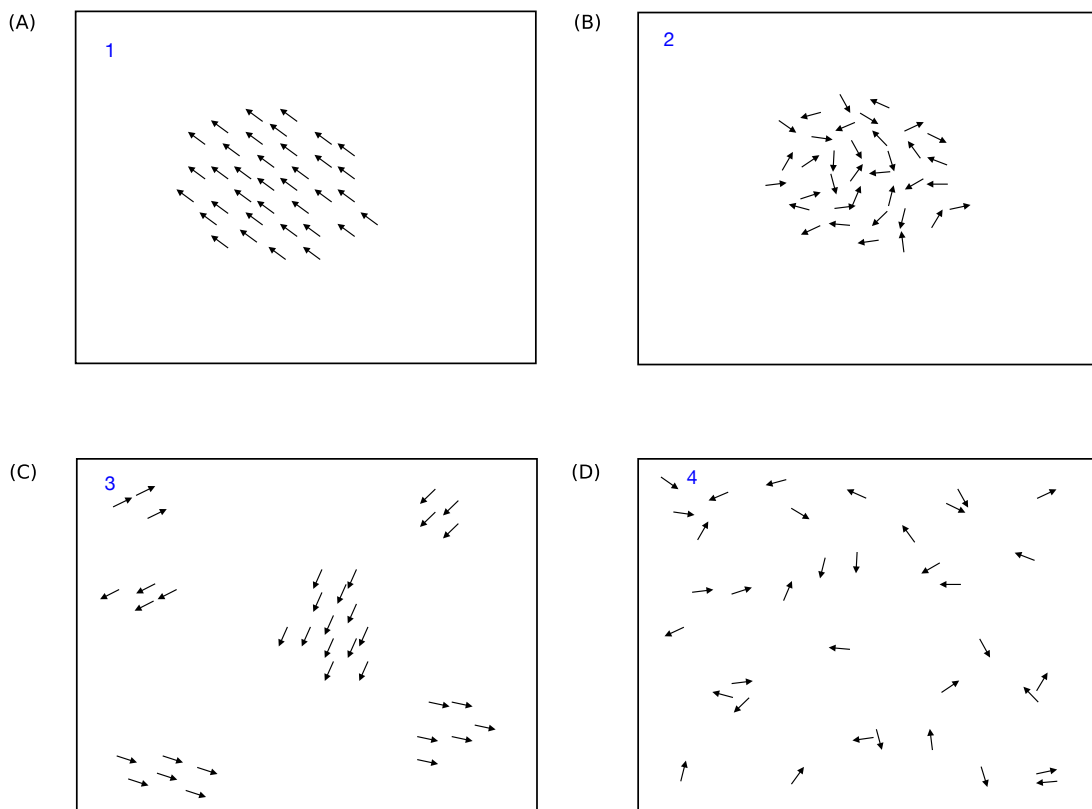
Figure 2.13: The four phases the clusters can take are illustrated here. (A) Flocking phase where all agents form one cohesive group traveling in the same direction. (B) Static swarm where agents remain in one unfragmented group but are unable to reach an ordered state, so the cluster overall stays stationary. (C) Fragmented flocks, where the system fractures into smaller groups which remain ordered, and (D) where the entire system evaporates into individual disordered clusters or individual agents.

Physical collision models

Active Brownian Particles (ABP)

Active brownian particle models are mostly used to simulate colloidal particles or those that interact through phsyical collisions while the direction of self propulsion undergoes angular diffusion. Since the particles only interact through physical collisions, alignment interactions are in the form of a torque or rotation towards the instantaneous direction of travel, similar to what would happen when active rods collide with each other and push against each other until they are reoriented to be aligned. This can result in a collective flock if the particle density is sufficiently high.

To impliment this model the direction of self propulsion is equal to the instantaneous velocity of the particle with angular diffusion as denoted by $\vec{\eta}$. Noise is included as a random angular adjustment from a Gaussian distribution with variance equal to η. This is the case for both physical cohesive interaction and alignment, as would occur in colloids or bacteria.

$$\vec{d_i} = \dot{\vec{x}}_i + \vec{\eta}$$

Active Colloids (AC)

In a case where the alignment interaction is cognitive and agents process direction information and reorient based what their neighbors are doing the self propulsion direction comes from a standard Vicsek alignment interaction again with angular diffusion, as shown below.

$$\dot{\vec{d_i}} = \sum_j^{nbr} \vec{d_j} + \vec{\eta}$$

As with the active brownian particle model the physical interactions or $\vec{P}$ are due to a cohesive interactions, in our case we used a Lennard-Jones potential shown in eq. 2.18. The Lennard-Jones force acting on a particle acts from all neighboring particles and summed up as shown below.

$$\vec{P_i} = \sum_j^{nbr} \vec{LJ}_{ij}$$

Vicsek-like models

Normalized alignment (NA)

We also looked at a model where both the alignment and colision avoidance is a cognitive process and contribute to the direction of self propulsion $\vec{d}$. We still use a Lennard-Jones interaction as the cohesive interaction as shown in eq. 2.3 but now all of the interactions go into the propulsion direction and are normalized so agents always move at a constant speed.

$$\vec{d_i} = \sum_j^{nbr} (\alpha \frac{\dot{\vec{x}}_j}{|\dot{\vec{x}}_j|} + \epsilon \vec{LJ}_{ij}) + \vec{\eta}'$$

Alignment (AL)

We also examined a model where the alignment interaction is not normalized, so agents with more neighbors, or neighbors that are more aligned with eachother, will more strongly prefer a direction of travel equal to the average of the neighbors when compared to the Lennard-Jones interaction and noise:

$$\vec{d_i} = \sum_{j}^{nbr}(\alpha\dot{\vec{x}}_j + \epsilon\vec{L}J_{ij}) + \vec{\eta'}$$

In this case the noise $\vec{\eta'}$ is a randomly oriented vector with magnitude η'. Since the agents now use some cognitive process to reorient in order to avoid collisions and maintain a prefered distance to neighbors the physical interaction vector does not take effect in either of these models (NA, or AL).

$$\vec{P_i} = \vec{0}$$

2.2.2   Results

Homogeneous systems

Typically an increase in noise is associated with a transition from an ordered (flocking) to a disordered (static) state, and we expect a decrease in cohesive interaction strength to lead to system fracture. For all four models we see a flocking to static transition with increasing noise for a wide range of cohesive interaction strengths. Fig. 2.14(A) shows the noise driven transition for each model with a fixed reasonable cohesive interaction strength of $\epsilon = 0.5, 0.5, 0.004, 0.004$ for AL, NA, AC, and ABP respectively. In all four cases there is a noise driven transition from a flocking to a static state with increasing noise. Fig. 2.14(B) shows the critical noise value where the order parameter passes through 0.5 against the cohesive interaction strength ϵ. If we look at how this noise driven transition depends on the cohesive interaction strength we see that in the cognitive cohesive interaction models (AL, and NA) when ϵ is sufficiently high the ordered state is unreachable for any amount of noise, so there is effectively a transition from a flocking to a static state with increasing cohesive interaction strength. For the AC model with physical collisions and cognitive alignment the transition is almost completely independent of cohesiveness and entirely driven by increasing noise, as seen by the horizontal red line in Fig. 2.14(B). In the ABP model the alignment interaction is closely tied to the cohesive interaction, as it is due to reorientation with the instantaneous velocity, which is in turn dependent on collisions with other particles. For this model the noise driven transition is sensitive to the cohesive interaction strength. The steep decrease in the critical noise value with increasing cohesive strength at low cohesion is most likely due to the cluster sizes, as the system fragments into extremely small 1, 2 or 3 agent clusters for low cohesive interaction strength. The order of these small clusters can appear artificially high if the random motion leads to the 2 or 3 agents aligning with eachother, when the overall system is in more of a gaseous disordered state as individual agents are disregarded when calculating average order. At slightly higher cohesive interaction above $\epsilon = 10^{-3}$ the system can no longer fracture and the critical noise value increases with increasing cohesive interaction as the two interactions are closely linked for the ABP model. While for the other three models the cohesive and

alignment interactions act more competitively that cooperatively, which leads to higher order in general but a decreasing trend between critical noise and cohesion.

We can also look at the amount of fracture occuring in the system by calculating the normalized average largest cluster size. Fig. 2.14(C) shows the average largest cluster plotted against the cohesive interaction strength with fixed noise $\eta = 1, 1, 3, 0.5$ for AL, NA, AC, and ABP respectively. For low cohesion the cluster fragments into small clusters or individual agents, and with increasing cohesion the cluster transitions into a state where it no longer fractures and the average largest cluster is the system size ($\mathcal{N} = 1$). We define the fracture transition as when at least 50% of the agents are in the largest cluster, which is where this average largest cluster ($\mathcal{N}$) passes through 0.5. We can then look at how the fracture transition depends on the amount of noise in the system. For the AL and NA models with both cognitive alignment and cohesion the fracture transition is independent of noise. In the AL model the fracture transition happens at $\epsilon = 2 \times 10^{-1}$ which is also associated with a sharp increase in the critical noise value seen in Fig. 2.14(B), which is different than the NA model where the fracture transition at $\epsilon = 2 \times 10^{-2}$ leads to a decrease in the critical noise value. This implies that the smaller fractured clusters in the AL model will have lower order than the unfractured system, while in the NA model the small fractured clusters are able to flock with higher noise than the unfractured cluster. This is due to the fact that in the AL model the alignment interaction is unnormalized so agents with more neighbors will have an effectively larger alignment interaction which will occur more in unfractured clusters than the smaller fractured ones. In the NA model the alignment is normalized and so neighbor number does not effect the alignment interaction and smaller clusters show higher critical noise values.

The ABP model also has a fracture transition that is independent of noise. While the AC model shows a very strong dependence of fracture transition on noise. The high fracture transition for noise values below 2.0 in the AC model are below the constant noise driven transition seen in Fig. 2.14(B) AC model, meaning the system is more likely to fracture while it is in the ordered state. This is due to locally ordered domains which form and then pull apart from eachother.
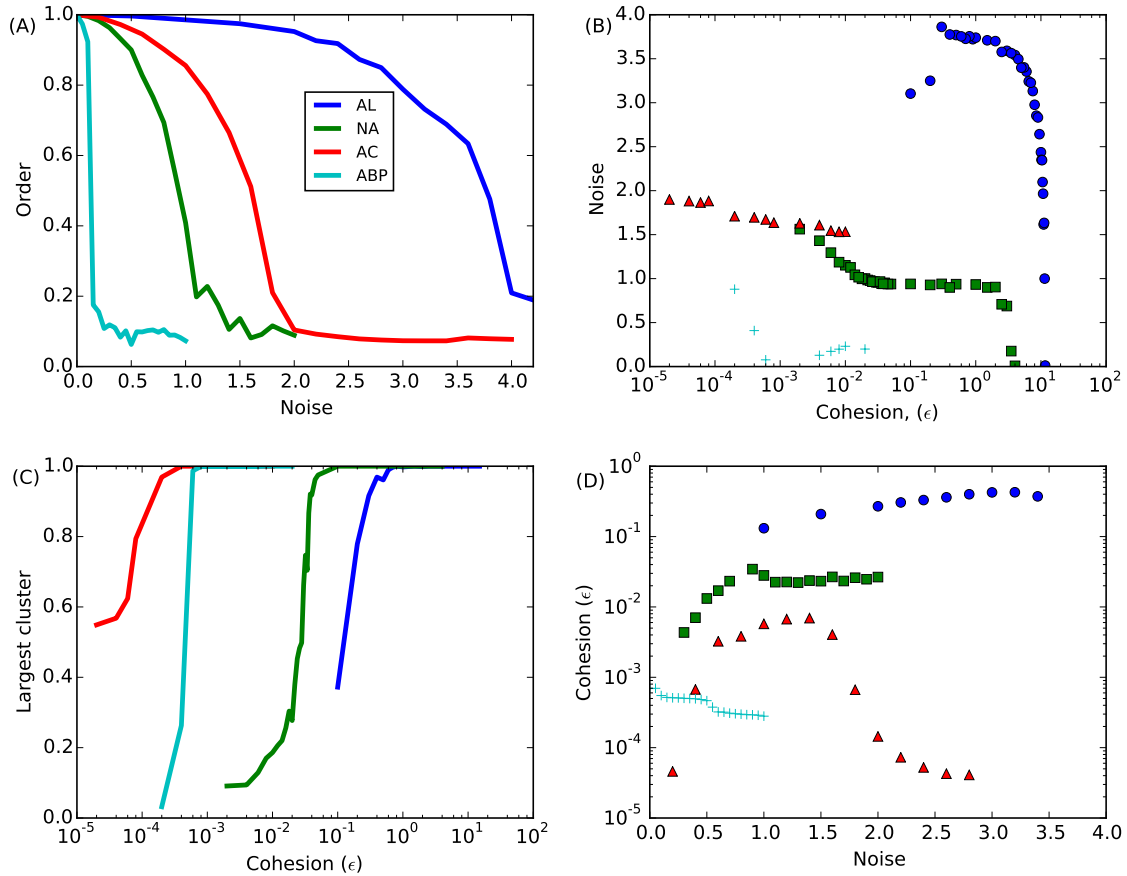
Figure 2.14: AL - Vicsek alignment where the alignment interaction is unnormalized. NA - Standard Vicsek model with normalized alignment. AC - Active colloids which align by a normalized Vicsek alignment and self propulsion is separate from physical collisions. ABP - Active Brownian Particle model where propulsion is in the direction of instantaneous velocity, which leads to alignment. (A) Order vs. noise plot for all four models with $\epsilon = 0.5, 0.5, 0.004, 0.004$ for AL, NA, AC, and ABP respectively. (B) The critical point for the noise transition for various cohesive interaction strengths (ϵ). (C) The chance of the cluster fracturing vs. the cohesive interaction strength (ϵ) with Noise $= 1, 1, 3, 0.5$ for AL, NA, AC, and ABP respectively. (D) The critical transition point for the chohesive interaction strength vs. the noise in the system.

Heterogeneous system

In order to study systems with noise heterogeneity we randomly select a subpopulation of a fraction f of the system to be high noise while the remainder of the system is a low noise population. The fraction f of high noise agents is the heterogeneity fraction. We selected two values of noise η, one above and one below the order transition for the uniform system and then assigned a fraction f of the agents the high η value and the remainder the lower value of η. By increasing the fraction of high noise agents we see an effect similar to increasing the noise of the uniform system. For all four models there are a couple

consistencies between the phase diagrams in the cohesion (ϵ) / heterogeneity fraction (f) parameter space. Fig. 2.15 (A, B, C, and D) show this phase diagram for AL, NA, AC, and ABP respectively. The AL, and NA models are very similar as in the uniform system case due to the similarity in the model details.

The increase in f leads to a transition between ordered flocks, either fragmented or cohesive to a disordered state. In the AL model the f driven order transition below a critical ϵ is independent of ϵ while in the fragmenting regime at low cohesion of the NA model the f driven transition is sensitive to the cohesive interaction strength. This suggests that fragmentation in the NA model leads to more ordered small clusters, while in the AL model the ordered state drives fracture to occur for low f as ordered domains form with differing polarization that pull apart from eachother. This does not occur in the AL model because as an ordered state is reached with decreasing noise or f the alignment interaction does not become strong enough to pull the system apart until there is sufficient order within the system for a flocking state to be reached without fracture, due to the fact that the alignment interaction is not normalized.

In all four models there is a static cohesive cluster phase for high ϵ and high f, and a fragmented flock phase when f and ϵ are sufficiently low. For the AC and ABP models the phase transitions become more complicated and fracture transition is not simply driven by ϵ and order is not primarily dependent on f. In the cases where the propulsion and physical interactions are separated (AC, and ABP) and the agents do not necessarily always travel at constant velocity, the fracturing and order transitions become much more tied together. For the AC model, both system fracture and the order to disorder transition occur with increasing f, with only a small region of flocking for high cohesion and low f and a small region of evaporation between the static swarm and fragmented flocking regimes. Conversely the ABP model shows a similar transition but much more driven by an increase in cohesion than an increase in heterogeneity fraction. The heterogeneity does however drive the system from an ordered flocking phase to a static swarming phase at high cohesion. The amount of heterogeneity sustainable by the flock increases with increasing cohesion because of the close tie between cohesion and alignment in the ABP model.

By fixing the fraction and varying the value of noise in the high noise population we were also able to determine if the phases that occur in the heterogeneous system are dependent on the overall meanfield noise within the system or simply the fraction of high and low noise agents. What we found was that for the AL and ABP models the phases are dependent on the average noise level in the overall system, while for the NA and AC models simply the fraction of high and low noise agents are important for driving transitions.
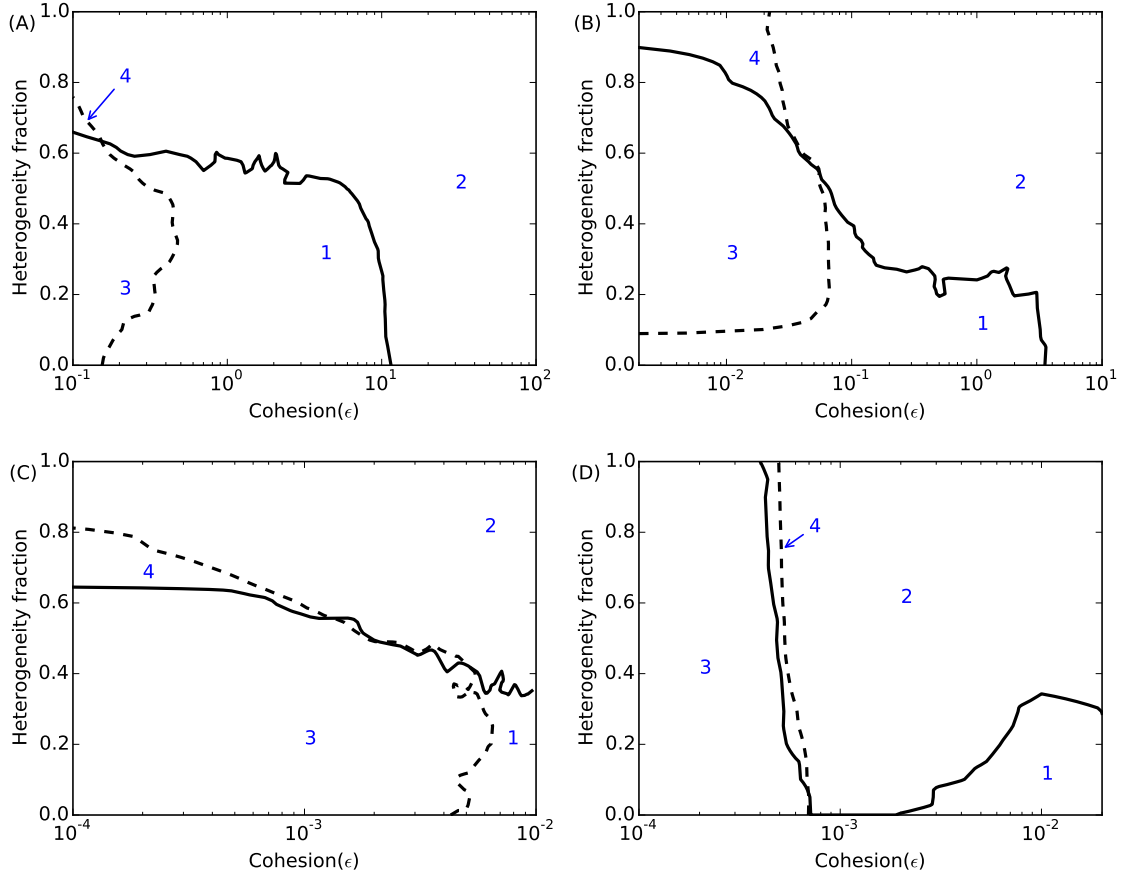
Figure 2.15: Phase diagrams for the fraction of high noise agents present against the cohesion for each of the four models. The four phases are marked 1 - flocking, 2 - static, 3 - fragmented flocks, and 4 - gaseous. The solid line represents the order transition while the dashed line shows the fracture transition. (A) Shows the AL model phase diagram. (B) NA phase diagram. (C) AC phase diagram, and (D) ABP phase diagram.

2.2.3 Discussion

Swarming systems in nature can have behavioral heterogeneity, which can come in many different forms including noise heterogeneity. We utilized four swarming models found in the literature to examine the effects of noise heterogeneity on swarming systems. By classifying the distance dependent cohesion interaction as cognitive or physical we can separate the models into two categories. In the models where the cohesion is cognitive an increase in cohesive interaction can drive a transition from an ordered into a disordered state. While models where the physical cohesion insterations are not normalized along with the alignment interaction as a cognitive process, the increase in cohesive interaction strength either does not effect the order transition which is only driven by noise, or an increase in cohesive interaction can lead to more stable flocking, and an increase in the order transition point with noise. Specifically the ABP model which is used to model active brownian particles, such as colloids, the alignment mechanism is closely tied to the cohesive

interaction and leads to an increase in alignment with high cohesive interaction strength.

When noise heterogeneity is introduced, in the cognitive cohesive models (AL and NA) the order to disorder transition is still driven by an increase in noise while fracture is driven by a decrease in cohesive interaction strength. Interestingly with an unnormalized alignment interaction the average noise of the system drives the transition between order and disorder however typical Vicsek like swarming models have a normalized alignment interaction, in this case the order to disorder transition with increasing heterogeneity fraction of the high noise population is driven by the fraction of high noise particles.

Models where the cohesiveness and collisions are separate from the propulsion of the agents (AC and ABP) the fracture and order transitions lie almost entirely on top of eachother, when the alignment is from a Vicsek like interaction an increase in high noise fraction on particles can drive the system from a fractured flocking phase into a cohesive static state while in the ABP model where the alignment is driven by reorientation with instantaneous velocity the fracture transition results from a decrease in cohesion, and once fracture begins to occur the system forms small ordered clusters. While for high cohesion where the system is unable to fracture, the increasing fraction of high noise agents drives the system from a cohesive flock to a static phase.

Our results show that a Vicsek alignment interaction leads to a system where the order to disorder transition with noise occurs at a lower noise value with increaseing cohesion while an alignment interaction driven by particles reorienting with their own instantaneous velocity results in the opposite, where an increase in cohesive interaction leads to an increase in the amount of noise that can be sustained within the system. This holds for both uniform and heterogeneous noise systems. When the cohesive interaction is grouped with the alignment interaction and then normalized and particles move with constant velocity an increase in cohesive interaction strength beyond a certain point leads to an order to disorder transition. This also results in the fractured state existing as small flocks rather than a gaseous state.

Chapter 3

Environmentally driven behavioral variability

Collective motion systems may also display transient variations in behaviors between individuals driven by local environment changes. A flock of birds can fly into a cloud or an area of different air temperature, fish schools can swim into colder water or cells can move across substrates with variable stiffness which effects the speed at which they move. Individual agents may also experience different local environments when changing relative position within a flock. For example, a cell moving between the interior or exterior of a cluster, or a bird moving from the outside into the center of a flock. Cells in the core of a cluster become completely surrounded by other cells and as a result will move slower which effects the motion of the cluster as a whole. In this chapter we discuss the effects of agent behavioral variability driven by environmental changes. In section 3.1 we discuss flock motion as it moves from one environment to another, in section 3.2 we examine the effects of agent behavior which is dependent on local density, such as when cells move between the interior and exterior of a cluster, this work was done in collaboration with an experimental research group.

3.1 Active matter clusters at interfaces

Swarming is a widespread biological phenomenon characterized by long range order emerging in a system from local interactions between agents[13], such as a swarm of flies[4, 5], or flock of birds[1]. Typically, a group of flocking individual organisms self-organize to form a cohesive cluster with directed motility in a spontaneously chosen consensus direction, for example a school of fish[43], cluster of cells during tumor growth, tissue development and repair[44, 45], or herd of wildebeests[8]. These types of swarming systems will often encounter a change in the environment, such as a flock of birds flying into a cloud or area of lower air temperature, or a cluster of tumor cells invading different tissue types[46]. Single cells have been shown to change their speed and direction when crossing sharp interfaces [47]. Swarms can also use collective dynamics to find and localize themselves to preferred niches or microenvironments. For example it has been observed that golden shiners, *Notemigonus crysoleucas*, which prefer low lighting, will spend more time in dark areas if they are part of a school due to cooperative sensing capabilities of the group[48]. Bacteria have also been shown to take less time to reach a target in

the presence of noisy chemical concentration gradients in the environment when they are part of a cluster[49]. Also *e. coli.* clusters modify their own environment by secreting chemicals to create an environmental change between the inside and outside of the cluster in order to trap the *e. coli.* and maintain clustering behaviors[50]. It is therefore important to understand the effects of spatial environmental changes on a cohesive swarming group. In this paper we investigate finite swarming clusters moving through heterogeneous environments where agents change their speeds by exerting different forces within each environment. Such changes could arise from the agent's sensing and response to a variety of environmental factors such as temperature, substrate stiffness, or chemical composition. So, how is the path that a swarm takes affected by the presence of a boundary between different environments, and how does that depend on the properties of the cluster and the environmental change?

Agent based models[16] and hydrodynamic continuum models[17] have been used with great success to model natural collective systems[13, 12], and reveal phases and transitions which emerge from the active, far from equilibrium nature of these systems[66, 26]. Agent based models are implemented by defining a set of interactions and update rules for individuals and then letting the system evolve in time, such systems show phase transitions driven by a wide variety of quantities including noise, density[11], environmental disorder[18], behavioral heterogeneities[19, 20], and cohesive interaction details [21, 22]. They have also been used to study how swarms use cooperation to achieve specific goals which are useful to biological systems, such as cooperative decision making[23], agent segregation[24], and obstacle avoidance[25]. Hydrodynamic continuum models on the other hand do not treat each agent as an individual, but instead study an average alignment and density profile within the system[27]. Hydrodynamic swarming models have established active matter as a type of nonequilibrium complex fluid[67, 58] and provided a unified framework to study phase transitions[68, 27], instabilities[69] and pattern formation[70] in active systems.

To answer the question of swarms crossing from one environment into another, we utilize a simplified model for a swarm that assumes a polarized ordered state with velocities correlated across the system[2] and finite system size, which allows us to examine the overall behaviors of the swarm crossing an interface without necessitating details about individual agent motion as in agent based models, or infinite system sizes as in hydrodynamic models. We consider a swarm as a single cohesive disk-shaped unit, or cluster, each individual agent within the swarm manifests as a force per unit area applied to the disk in the direction of polarization. We then allow the cluster to cross an interface between two differing environments where the portion of the swarm in each environment may apply stronger or weaker forces to the cluster depending on the substrate, resulting in a torque and therefore a curved trajectory. We can then map the trajectories of the cluster and measure the resulting relationships between the cluster motion before and after crossing the interface. We find four catagories for cluster behavior which depend on two important cluster parameters. The two important parameters are cluster speed, i.e. low speed (overdamped) vs. high speed (underdamped) clusters, and the ratio of the rotational damping to translational friction. It is to be noted that though a prescribed amount of rotational damping arises from the translational friction on the disk, the ratio is a parameter that could be smaller (or bigger) depending on whether the cluster exerts torques to maintain (or resist) rotation.

Our model has predictive capabilities for determining the curved path of a cell cluster at an interface between substrates. The results of which could be extended to suggest

possible methods of patterning substrates to direct cell cluster motion. Other regimes of our model provide insight into the behaviors of faster swarms, such as bird flocks and fish schools, moving between heterogeneous environments. Finally, for swarms that exert torques to maintain turning, we show that swarms can display circular paths and trapping at interfaces.
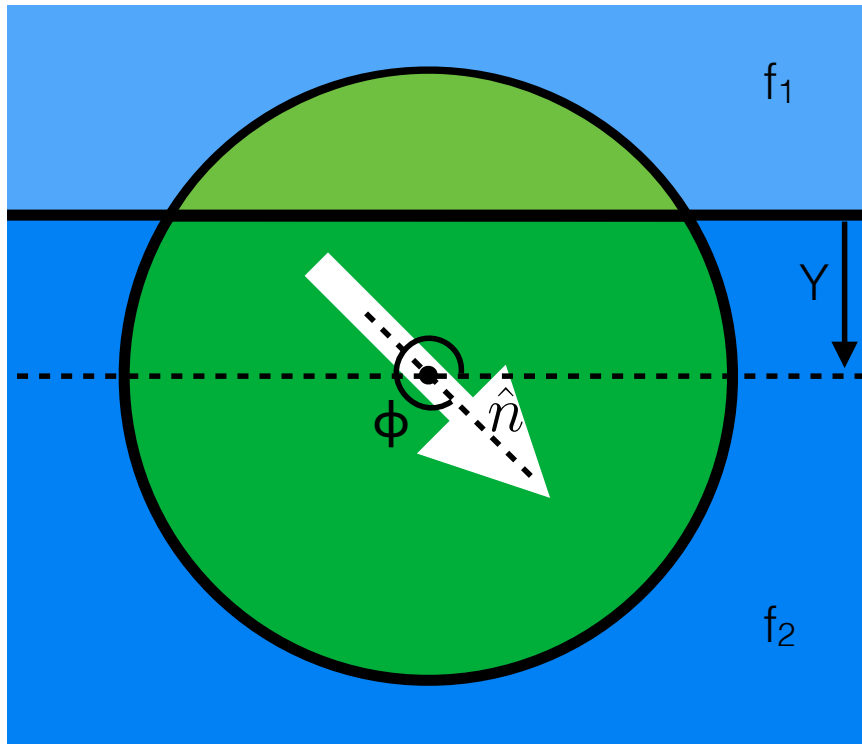
3.1.1   The Model.

Figure 3.1: View from above showing the two regions one above (light green) and below (dark green) the interface between two different substrates shown in light and dark blue respectively. Each region of the cluster propels itself along the polarization direction ($\hat{n}$ at an angle of Φ with the positive x-axis) with a force per unit area of f_1 for the top region and f_2 for the bottom region. The cluster center is at a height Y above the interface (in the diagram shown Y is negative because the center of the cluster is below the interface).

We use a mathematical model for a swarming cluster (Fig. 3.1) that treats it as a single cohesive unit that moves on a two dimensional substrate by exerting a force per unit area in some cluster polarization direction (at an angle Φ with respect to the positive x-axis). We then examine a single cluster moving across an interface between two different substrates where the area of the cluster contained on substrate 1 (shown in light green above the solid horizontal line in Fig. 3.1) exerts a force per unit area of f_1 and the portion on substrate 2 (shown by the dark green area in Fig. 3.1) exerts a force per unit area of f_2. The force applied on the cluster by every portion of the cluster is in the direction of polarization with a magnitude that depends on the areas within each substrate and the substrate dependent forces. The cluster also experiences a friction-like damping force resisting translational

motion. Utilizing these details we can calculate a force on the cluster at any height Y above a horizontal substrate interface (See appendix for details).

If the cluster is polarized at an angle which is not normal to the interface there is an asymmetry of the forces on either side of the interface, which results in a torque on the direction of polarization of the cluster which in turn rotates the direction of the force on the cluster and can result in a curved trajectory or a bend in the path of the cluster as it crosses the interface. This torque can be calculated from the force per unit area of the cluster on each substrate along with the distance from the cluster center. From the derived expressions for force and torque (see appendix) we can find the non-dimensionalized equations of motion for the cluster shown in eqs.3.1-3.3, where v_1 and v_2 are the equilibrium speeds of the cluster in the top and bottom substrates respectively, and C is the ratio of the angular damping to the translational friction on the disk. In the non-dimensionalized forms of the equations shown below the translational/frictional damping constant is incorporated into the equilibrium speeds v_1 and v_2.

$$\frac{d^2\Phi}{dT^2} = \frac{4}{3\pi}\sqrt{1-Y^2}(1+Y^2)(v_2 - v_1)\cos(\Phi) - C\frac{d\Phi}{dT} \tag{3.1}$$

$$\frac{d^2X}{dT^2} = \left(1/2(v_1 + v_2) + 1/\pi(v_1 - v_2)\left(\arcsin(Y) + Y\sqrt{1-Y^2}\right)\right)\cos(\Phi) - \frac{dX}{dT} \tag{3.2}$$

$$\frac{d^2Y}{dT^2} = \left(1/2(v_1 + v_2) + 1/\pi(v_1 - v_2)\left(\arcsin(Y) + Y\sqrt{1-Y^2}\right)\right)\sin(\Phi) - \frac{dY}{dT} \tag{3.3}$$

We can then use finite difference methods to solve these equations of motion and examine the system subjected to different substrates and initial conditions. In the model the lengthscale is set by the cluster radius, and the timescale is set by the time taken for the cluster to accelerate from rest to the fraction $(1 - 1/e) \sim 0.63$ of its equilibrium speed. The active nature of the system allows the angular damping and translational friction to not be equal, implying $C \neq 1$. Physically we can expect $C > 1$ for situations when swarms exert torques to resist turning, and $C < 1$ for cases where swarms exert torques to maintain or persist in turning as seen in systems like the persistent turning walker model for *K. Mugil* fish[71]. How, then, does the incident angle and ratio of equilibrium speeds in each substrate affect the transmitted angle of the swarm? What is the effect of exerted torques which promote turning?
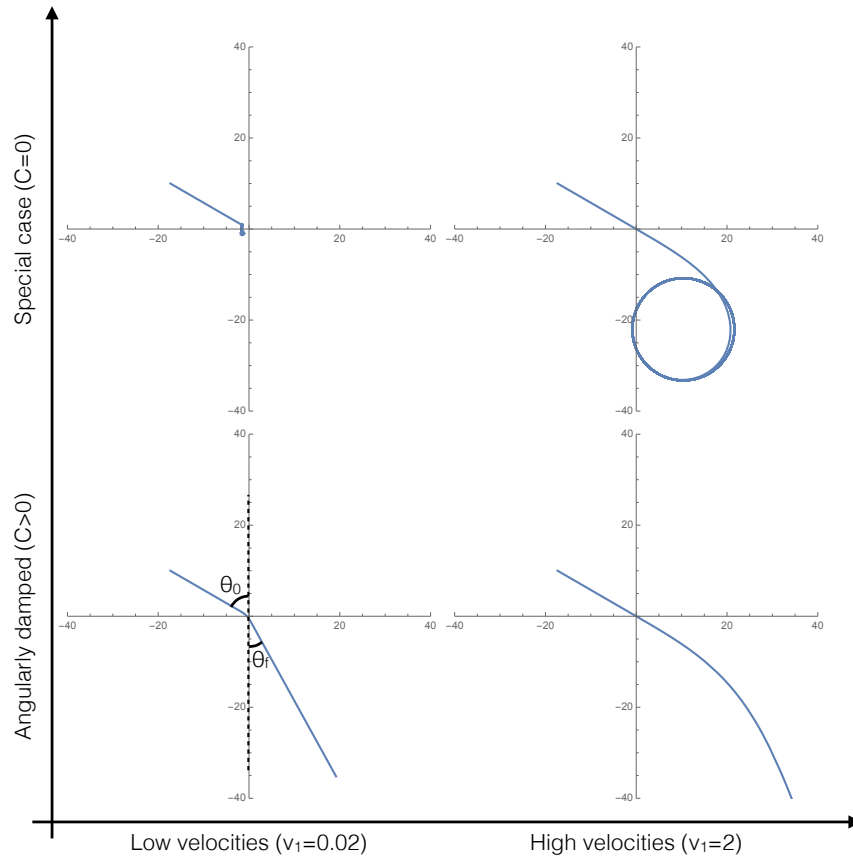
3.1.2   Results.

Figure 3.2: Representative trajectories of the system in each of the four limitting behaviors of the system. In all four cases $v_1 = 2v_2$.

Fig. 3.2 shows the four characteristic trajectories for limits of the two important parameters: low velocities (overdamped, friction dominated behaviors), high velocities (underdamped, inertia dominated behaviors), and clusters with angular damping ($C > 0$). At the end we consider a special limiting case where $C = 0$, relevant/applicable to agents that apply torques to promote turning which exactly cancel out any angular damping, resulting in unique cluster behaviors.
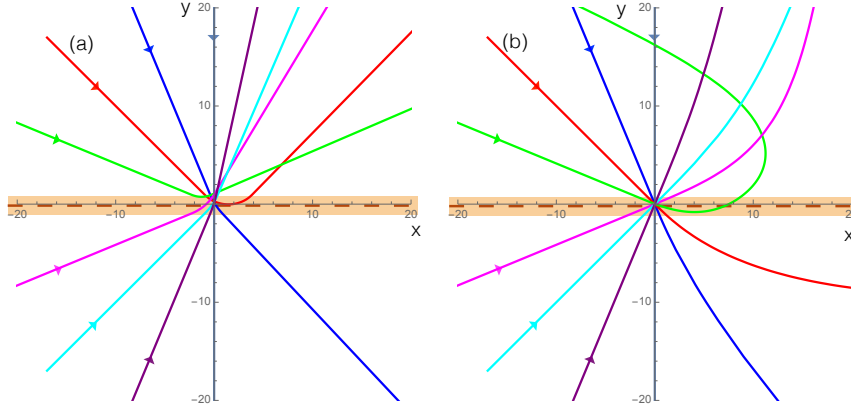
Cluster trajectories.

Figure 3.3: Example trajectories of the cluster, each color is a different incident angle where the incoming cluster is shown by the straight lines entering from the left of each plot ($x < 0$) directed towards the origin, and the clusters are in contact with the interface, which is at $y = 0$ (maroon dashed line), when the trajectory is within the orange band. The substrate on the bottom half ($y < 0$) has twice the equilibrium speed as the top substrate ($v_2 = 2v_1$) in both cases. (a) For low speeds, where friction dominates cluster motion, the cluster curves while it is in contact with the interface (orange band), and once it leaves the interface it has a well defined straight path along some rotated polarization direction. (b) High velocities, when inertia dominates, result in the cluster starting to curve when it comes into contact with the interface and then large sweeping curves away from the interface as the momentum of the cluster causes it to persist along the previous direction before gradually adjusting to the new substrate.

The overall behaviors of the cluster in the presence of angular damping fall into two different categories: refraction/reflection (Fig 3.3(a)), and large sweeping curves (Fig 3.3(b)). In both cases the direction that the cluster actively propels itself in ($\hat{n}$ at angle Φ) can only accelerate due to torques experienced while it is in contact with the interface. This means that while the cluster is on a single substrate the angular speed of $\hat{n}$ can only decrease due to rotational damping.

In the low velocity cases ($v_1 = 0.01$ in Fig. 3.3(a)) friction dominates the cluster motion and the cluster moves in a direction parallel to the active propulsion of the cluster ($\vec{v}||\hat{n}$) at nearly all times. In this friction dominated limit, the system can refract or reflect off of the interface and only comes into contact with the interface once allowing us to measure the incident and refracted angle and make predictions about the behaviors and interactions of the cluster with an interface.

The high velocity case ($v_1 = 5$ in Fig. 3.3(b)) is characterized by the fact that the cluster's translational inertia dominates the direction of cluster motion ($\vec{v}$), for an extended period of time after crossing the interface. In this high velocity case, as the cluster leaves the interface it will move in a direction which is not necessarily parallel to the direction of $\hat{n}$, resulting in the apparent angular acceleration away from the interface. However, after some time the system will reach equilibrium where $\vec{v}||\hat{n}$ and the cluster will move in a straight line in some well defined direction. In this case the momentum of the cluster carries it away

from the interface even if the direction of $\hat{n}$ is such that the cluster should be propelled towards the interface meaning that the cluster can rotate and return to the interface a finite number of times before reaching a stable straight trajectory within a single substrate. This high velocity (inertia dominated) case could model the motion of a bird flock crossing an interface between hotter and colder air where their momentum will continue to carry the flock in one direction and the speed and trajectory will gradually stabilize as the flock adjusts to the new environment, potentially traveling in a different direction from that with which it entered.
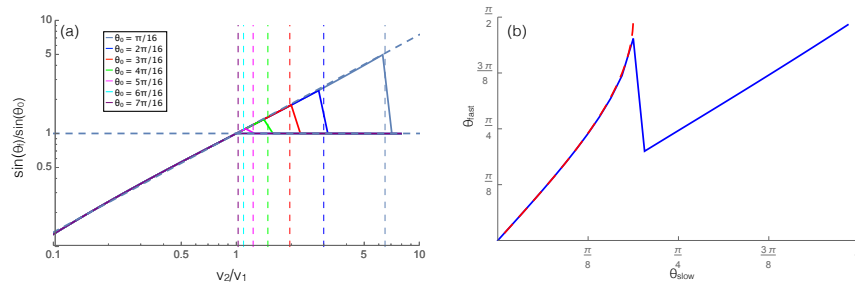
Refraction and reflection at an interface.

Figure 3.4: (a) The ratios of the sines of the incident (θ_0) and refracted (θ_f) angles plotted against the ratios of the equilibrium speeds in each material, with $v_1 = 0.001$. The vertical lines show the value of velocity ratio where the refracted angle would become greater than $\pi/2$, resulting in a reflection, for each initial angle shown in the legend. When the cluster is reflected (right side of the vertical dashed lines) the horizontal line at $\sin\theta_f / \sin\theta_0 = 1$ shows that the reflected angle is equal to the incident angle. (b) The angle that the trajectory makes (with respect to the normal to the interface) on the faster (θ_{fast}) and slower (θ_{slow}) substrates for a cluster moving from the slower substrate to the faster one shown in blue, and the similar angles for a cluster moving from the faster to the slower substrate shown in red dashed line. In both these cases $v_1 = 0.001$, and $v_2 = 0.002$, and $C = 1$.

In this section we examine the case where the velocity on each substrate is low enough that friction dominates, and the cluster experiences rotational damping ($C > 0$). The cluster in this regime is representative of slow moving natural swarming systems, including cell clusters, and bacteria swarms. A cluster approaching an interface at an angle will begin to turn when it comes into contact with the interface and when contact with the interface is lost it will travel in a straight line in a new direction. We can then measure the resulting angle and the incident angle (labeled θ_f and θ_0 respectively in Fig. 3.2) and compare them to the velocity ratio on the two substrates. To do this we plot the ratio of the sines of the refracted and incident angles against the ratio of the equilibrium velocities on each substrate. Fig. 3.4 (a) shows the relationship between these ratios for many initial angles (see legend), along with a fit line to the numerical data for the refraction angle which leads to the predicted reflections. Applying a similar fit to systems with different values of C leads to the relationship shown in Eq. 3.4. This relation bears a remarkable resemblance to Snell's law for optical paths except with an exponent of $0.87/C$ instead of unity. Additionally, when moving from a slower substrate to a faster one the cluster will be reflected off the interface

if the transmitted angle should be $\pi/2$ or greater, i.e. total internal reflection. The velocity ratio where reflection should begin to occur is shown as vertical dashed lines for different incident angles according to the color legend. The predicted reflections align well with the plotted data, where the ratio of the sines for each incident angle begins to reflect at the same point as the vertical dashed lines. The reflection is shown by the horizontal dashed line at 1, which implies that the reflected angle is equal to the incident angle beyond the velocity ratio which would result in $\theta_f > \pi/2$.

$$\frac{\sin\theta_2}{\sin\theta_1} = \left(\frac{v_2}{v_1}\right)^{0.87/C} \tag{3.4}$$

The trajectories of these clusters are also reversible in time as can be seen in Fig. 3.4(b) which shows the cluster trajectory angle with respect to normal on the faster substrate plotted against the angle of the trajectory on the slower substrate. The blue solid line shows the case where the cluster is moving from the slower substrate onto the faster one, and drops down to the diagonal line when reflection begins to occur. The red dashed line shows the angles for the faster to slower case. The overlap of these two curves shows that whether moving from faster to slower or vice versa the angles depend only on the substrates and angles and not on the initial substrate of the cluster. The refraction of the cluster into the slower medium while approaching at a large angle from the faster medium is similar to the reported behavior of the golden shiners that collectively turn into darker regions where they move slower[48].

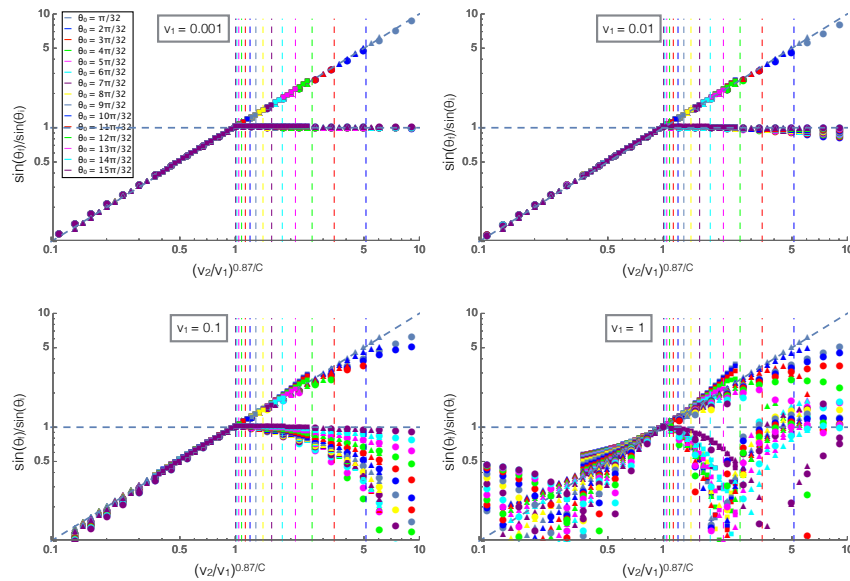**Fast swarms and swarms with exerted torques to promote turning.**

Figure 3.5: The ratios of the sines of the initial and final trajectory angles measured with respect to the normal to the interface. The velocity on the top substrate (v_1) is labeled for each plot and the color legend for incident angle is consistent across all four plots. Squares are for $C = 2$, triangles for $C = 1$ and circles for $C = 0.5$. The diagonal line is a fit for the low velocity case and the vertical lines are predicted values for the reflections to begin for each incident angle shown by color according to the legend.

In the case where the velocity on each substrate is high enough for interia to dominate cluster motion, the cluster will still adjust its direction as it passes through the interface but its own momentum will carry it straight across the interface before slowly adjusting it's angle depending on the rotations caused by the interface which we can see qualitatively in Fig. 3.3(b). This results in the cluster often returning to the interface and interacting with it multiple times making the refracted angle vary from the predictions made for the friction dominated case.

Fig. 3.5 shows the ratio of the incident and refracted angles of clusters versus the ratio of velocities scaled by angular damping similar to Fig. 3.4(a). In this plot the collapse at low velocities for different values of C is shown by the shapes of the markers, $C = 0.5$ for the circles, $C = 1$ (rotational damping arising from translational friction only) for the triangles and $C = 2$ for the squares, the shapes and color legend are consistent across all four plots shown. We can see that at high velocities the reflected angle varies greatly from the low velocity case where reflected angle was equal to incident angle. This is due to the fact that the cluster passes through the interface before turning around and then passes through the interface again resulting in multiple interactions with the interface and final reflected angles that don't relate in a well defined way to the incident angles. The refracted angle also differs from the low velocity case due to the effects of momentum and inertia at high velocities, the trajectories become complicated and cease to follow a well defined relationship. This behavior could be related to the complex fluid-like motions of starling flocks as they swoop

and change directions in large arcing trajectories, possibly due to changing environments from flying over trees or through different altitudes and air temperatures.
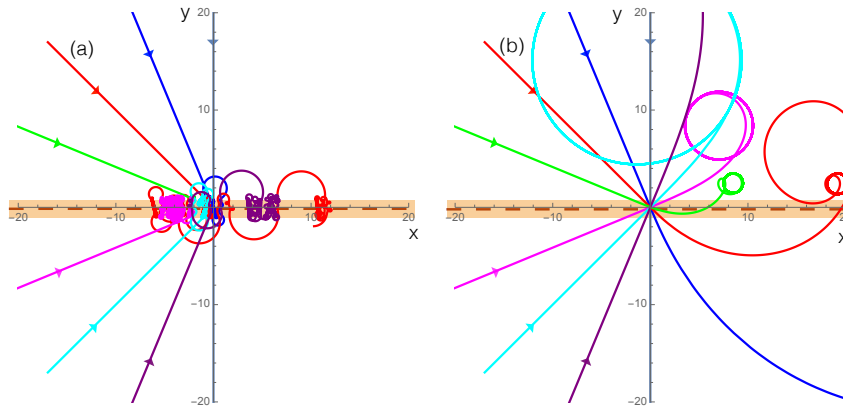

Figure 3.6: (a) Trajectories for the $C = 0$ case with low velocities. $v_1 = 0.001$ and $v_2 = 0.002$, the incident trajectories are the straight lines coming from the left. (b) Same as (a) but for the high velocity case where $v_1 = 5$ and $v_2 = 10$. The cluster is in contact with the interface while the trajectory is shown in the orange band.

Finally we consider a special case of a swarm that actively promotes rotations by exerting a torque that exactly cancels out any rotational resistance from friction-like damping (resulting in $C = 0$). In this case two very different behaviors emerge. The first is in the low velocity case where friction dominates the translational motion, though angular momentum is always important due to the fact that $C = 0$ independent of velocity. In this case the cluster will again begin to rotate as it crosses the interface, and experience no angular acceleration once it loses contact with the interface, however it will continue to rotate along a circular curve and return to the interface some time later. This causes the cluster to become trapped at the interface by always rotating around and returning to the interface without being able to escape as seen in Fig. 3.6(a). The second case is for high velocities where the inertia of the cluster will carry it past the interface and it may return to the interface or escape but the initial crossing of the interface starts the cluster rotating and the cluster will move in a circle somewhere away from the interface typically on the slower substrate as seen in Fig. 3.6(b).
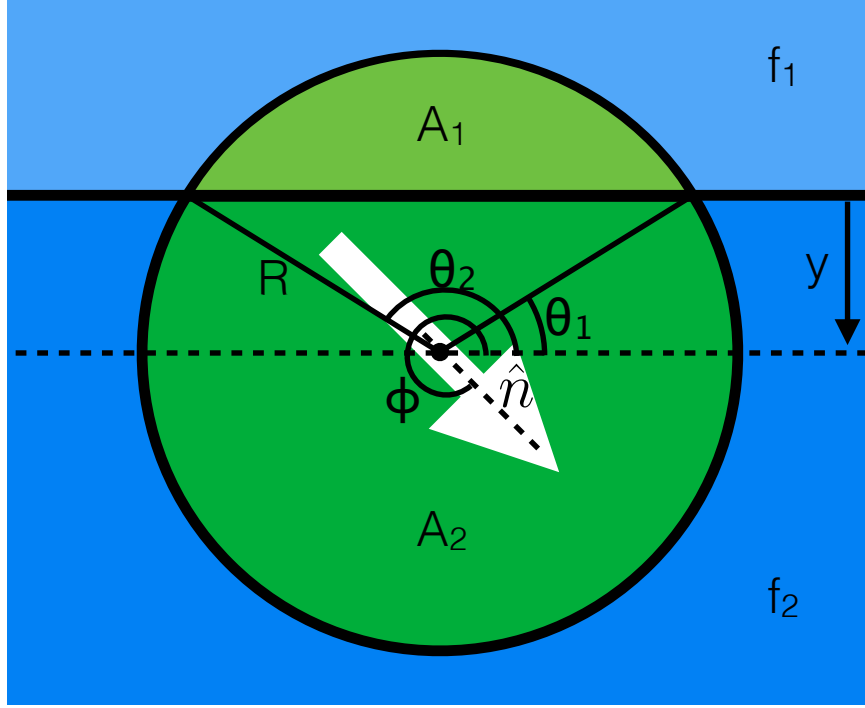
3.1.3   Detailed derivation

Figure 3.7: Diagram of cluster setup, the parameters are described below.

We use a mathematical model for a swarming cluster that treats it as a single cohesive unit that moves on a two dimensional substrate by exerting a force and torque per unit area whose magnitude depends on the nature of the substrate. Here we examine the effects of a single cluster moving across an interface between two different substrates where each portion of the cluster exerts a force per unit area depending on which substrate it is on. The force exerted on the cluster in direction of polarization ($\hat{n}$) is equal to the substrate dependent force per unit area ($f_{1(\text{or } 2)}$) multiplied by the area of the cluster on each respective substrate ($A_{1(\text{or } 2)}$), with damping constant b.

$$\mathbf{F} = (f_1 A_1 + f_2 A_2)\hat{n} - b\vec{v} \tag{3.5}$$

The area of the partial circles within each region at any heigh y above the substrate interface can be calculated by the interagrals shown below, where R is the radius of the cluster, and θ_1 and θ_2 are the angles to the intersections of the interface line and the rim of the cluster as shown in Fig. 3.7. Integrating and simplifying results in Eq. 3.6 as the net force on the cluster with radius R at height y above the interface.

$$\mathbf{F} = \left(f_1 \int_{\theta_1}^{\theta_2} \int_{\frac{y}{\sin\theta}}^{R} r\,dr\,d\theta + f_2 \int_{\theta_2}^{2\pi+\theta_1} \int_{\frac{y}{\sin\theta}}^{R} r\,dr\,d\theta \right)\hat{n} - b\vec{v}$$

$$\mathbf{F} = \left(f_1 \int_{\arcsin\left(-\frac{y}{R}\right)}^{\pi-\arcsin\left(-\frac{y}{R}\right)} \frac{1}{2}\left(R^2 - \frac{y^2}{\sin^2\theta}\right)d\theta + f_2 \int_{\pi-\arcsin\left(-\frac{y}{R}\right)}^{2\pi+\arcsin\left(-\frac{y}{R}\right)} \frac{1}{2}\left(R^2 - \frac{y^2}{\sin^2\theta}\right)d\theta \right)\hat{n} - b\vec{v}$$

$$\mathbf{F} = \frac{1}{2}\left(f_1\left(R^2\theta + y^2\cot\theta\right)_{\arcsin\left(-\frac{y}{R}\right)}^{\pi-\arcsin\left(-\frac{y}{R}\right)} + f_2\left(R^2\theta + y^2\cot\theta\right)_{\pi-\arcsin\left(-\frac{y}{R}\right)}^{2\pi+\arcsin\left(-\frac{y}{R}\right)}\right)\hat{n} - b\vec{v}$$

$$\mathbf{F} = \frac{1}{2}\Bigg(f_1\Big(R^2(\pi - \arcsin(-\frac{y}{R})) + y^2\cot(\pi - \arcsin(-\frac{y}{R}))$$
$$- (R^2(\arcsin(-\frac{y}{R})) + y^2\cot(\arcsin(-\frac{y}{R})))\Big)$$
$$+ f_2\Big(R^2(2\pi + \arcsin(-\frac{y}{R})) + y^2\cot(2\pi + \arcsin(-\frac{y}{R}))$$
$$- (R^2(\pi - \arcsin(-\frac{y}{R})) + y^2\cot(\pi - \arcsin(-\frac{y}{R})))\Big)\Bigg)\hat{n} - b\vec{v}$$

$$\mathbf{F} = \frac{1}{2}\Bigg(f_1\Big(R^2(\pi + 2\arcsin(\frac{y}{R})) + 2y\sqrt{R^2 - y^2}\Big)$$
$$+ f_2\Big(R^2(\pi - 2\arcsin(\frac{y}{R})) - 2y\sqrt{R^2 - y^2}\Big)\Bigg)\hat{n} - b\vec{v}$$

$$\mathbf{F} = \frac{1}{2}R^2\Bigg(f_1\Big(\pi + 2\arcsin(\frac{y}{R}) + 2\frac{y}{R}\sqrt{1-(y/R)^2}\Big)$$
$$+ f_2\Big(\pi - 2\arcsin(\frac{y}{R}) - 2\frac{y}{R}\sqrt{1-(y/R)^2}\Big)\Bigg)\hat{n} - b\vec{v}$$

The expression for force on the cluster due to the active force per unit area exerted by the cluster and damping is shown below.

$$\mathbf{F} = \frac{1}{2}R^2\Big(\pi(f_1 + f_2) + 2(f_1 - f_2)\big(\arcsin(\frac{y}{R}) + \frac{y}{R}\sqrt{1-(y/R)^2}\big)\Big)\hat{n} - b\vec{v} \qquad (3.6)$$

In addition to the substrate dependent force applied on the cluster, the polarization direction of the cluster will also be subject to a torque due to the asymmetry of the variable forces on each area of the cluster. The net torque on the cluster can be calculated by integrating the torque per unit area over the portions of the cluster on each substrate similar to the calculation of force above. The torque per unit area is due to the force per unit area at each point on the disk, i.e. $f_{1(\text{or }2)}\hat{n}\times\vec{r}$, with angular damping $-c\boldsymbol{\omega}$.

$$\boldsymbol{\tau} = \int_{A_1} f_1\hat{n}\times\vec{r}dA + \int_{A_2} f_2\hat{n}\times\vec{r}dA - c\boldsymbol{\omega} \qquad (3.7)$$

The area of the portions of the cluster on each substrate is integrated as in the force case above, and simplified to get the expression for torque on the cluster shown in Eq. 3.8.

$$\boldsymbol{\tau} = \int_{\theta_1}^{\theta_2}\int_{\frac{y}{\sin\theta}}^{R} f_1\hat{n}\times\vec{r}rdrd\theta + \int_{\theta_2}^{2\pi+\theta_1}\int_{\frac{y}{\sin\theta}}^{R} f_2\hat{n}\times\vec{r}rdrd\theta - c\boldsymbol{\omega}$$

$$\boldsymbol{\tau} = \left(\int_{\theta_1}^{\theta_2} \int_{\frac{y}{\sin\theta}}^{R} f_1 r \sin(\theta - \phi) r \, dr \, d\theta + \int_{\theta_2}^{2\pi+\theta_1} \int_{\frac{y}{\sin\theta}}^{R} f_2 r \sin(\theta - \phi) r \, dr \, d\theta \right) \hat{z} - c\boldsymbol{\omega}$$

$$\boldsymbol{\tau} = \left(\int_{\theta_1}^{\theta_2} f_1 \sin(\theta - \phi) \frac{r^3}{3} \Big|_{\frac{y}{\sin\theta}}^{R} d\theta + \int_{\theta_2}^{2\pi+\theta_1} f_2 \sin(\theta - \phi) \frac{r^3}{3} \Big|_{\frac{y}{\sin\theta}}^{R} d\theta \right) \hat{z} - c\boldsymbol{\omega}$$

$$\boldsymbol{\tau} = \left(\int_{\theta_1}^{\theta_2} f_1 (\sin(\phi)\cos(\theta) - \cos(\phi)\sin(\theta)) \left(\frac{R^3}{3} - \frac{y^3}{3\sin^3\theta} \right) d\theta \right.$$
$$\left. + \int_{\theta_2}^{2\pi+\theta_1} f_2 (\sin(\phi)\cos(\theta) - \cos(\phi)\sin(\theta)) \left(\frac{R^3}{3} - \frac{y^3}{3\sin^3\theta} \right) d\theta \right) \hat{z} - c\boldsymbol{\omega}$$

$$\boldsymbol{\tau} = \left(\int_{\theta_1}^{\theta_2} f_1 \frac{R^3}{3}(\sin(\phi)\cos(\theta) - \cos(\phi)\sin(\theta)) - y^3 \frac{\sin(\phi)\cos(\theta)}{3\sin^3(\theta)} + y^3 \frac{\cos(\phi)}{3\sin^2(\theta)} d\theta \right.$$
$$\left. + \int_{\theta_2}^{2\pi+\theta_1} f_2 \frac{R^3}{3}(\sin(\phi)\cos(\theta) - \cos(\phi)\sin(\theta)) - y^3 \frac{\sin(\phi)\cos(\theta)}{3\sin^3(\theta)} + y^3 \frac{\cos(\phi)}{3\sin^2(\theta)} d\theta \right) \hat{z} - c\boldsymbol{\omega}$$

$$\boldsymbol{\tau} = \left(f_1 \left(\frac{R^3}{3}\sin(\phi)\sin(\theta) + \frac{R^3}{3}\cos(\phi)\cos(\theta) + \frac{y^3\sin(\phi)}{6\sin^2(\theta)} - \frac{y^3\cos(\phi)\cos(\theta)}{3\sin(\theta)} \right)_{\arcsin(-\frac{y}{R})}^{\pi-\arcsin(-\frac{y}{R})} \right.$$
$$\left. + f_2 \left(\frac{R^3}{3}\sin(\phi)\sin(\theta) + \frac{R^3}{3}\cos(\phi)\cos(\theta) + \frac{y^3\sin(\phi)}{6\sin^2(\theta)} - \frac{y^3\cos(\phi)\cos(\theta)}{3\sin(\theta)} \right)_{\pi-\arcsin(-\frac{y}{R})}^{2\pi+\arcsin(-\frac{y}{R})} \right) \hat{z} - c\boldsymbol{\omega}$$

$$\boldsymbol{\tau} = \hat{z}\Big(f_1 \times$$

$$\left(\frac{R^3}{3}\sin(\phi)\sin(\pi-\arcsin(-\frac{y}{R})) + \frac{R^3}{3}\cos(\phi)\cos(\pi-\arcsin(-\frac{y}{R}))\right.$$

$$\left. + \frac{y^3\sin(\phi)}{6\sin^2(\pi-\arcsin(-\frac{y}{R}))} - \frac{y^3\cos(\phi)\cos(\pi-\arcsin(-\frac{y}{R}))}{3\sin(\pi-\arcsin(-\frac{y}{R}))}\right)$$

$$- f_1\left(\frac{R^3}{3}\sin(\phi)\sin(\arcsin(-\frac{y}{R})) + \frac{R^3}{3}\cos(\phi)\cos(\arcsin(-\frac{y}{R}))\right.$$

$$\left. + \frac{y^3\sin(\phi)}{6\sin^2(\arcsin(-\frac{y}{R}))} - \frac{y^3\cos(\phi)\cos(\arcsin(-\frac{y}{R}))}{3\sin(\arcsin(-\frac{y}{R}))}\right) + f_2\times$$

$$\left(\frac{R^3}{3}\sin(\phi)\sin(2\pi+\arcsin(-\frac{y}{R})) + \frac{R^3}{3}\cos(\phi)\cos(2\pi+\arcsin(-\frac{y}{R}))\right.$$

$$\left. + \frac{y^3\sin(\phi)}{6\sin^2(2\pi+\arcsin(-\frac{y}{R}))} - \frac{y^3\cos(\phi)\cos(2\pi+\arcsin(-\frac{y}{R}))}{3\sin(2\pi+\arcsin(-\frac{y}{R}))}\right)$$

$$- f_2\left(\frac{R^3}{3}\sin(\phi)\sin(\pi-\arcsin(-\frac{y}{R})) + \frac{R^3}{3}\cos(\phi)\cos(\pi-\arcsin(-\frac{y}{R}))\right.$$

$$\left.\left. + \frac{y^3\sin(\phi)}{6\sin^2(\pi-\arcsin(-\frac{y}{R}))} - \frac{y^3\cos(\phi)\cos(\pi-\arcsin(-\frac{y}{R}))}{3\sin(\pi-\arcsin(-\frac{y}{R}))}\right)\right) - c\boldsymbol{\omega}$$

$$\boldsymbol{\tau} = \hat{z}\Big(f_1\left(\frac{R^3}{3}\sin(\phi)(-y/R) + \frac{R^3}{3}\cos(\phi)(-\sqrt{R^2-y^2}/R)\right.$$

$$\left. + \frac{y^3\sin(\phi)}{6y^2/R^2} - \frac{y^3\cos(\phi)(-\sqrt{R^2-y^2}/R)}{3(-y/R)}\right)$$

$$- f_1\left(\frac{R^3}{3}\sin(\phi)(-y/R) + \frac{R^3}{3}\cos(\phi)(\sqrt{R^2-y^2}/R)\right.$$

$$\left. + \frac{y^3\sin(\phi)}{6y^2/R^2} - \frac{y^3\cos(\phi)\sqrt{R^2-y^2}/R}{3(-y/R)}\right)$$

$$+ f_2\left(\frac{R^3}{3}\sin(\phi)(-y/R) + \frac{R^3}{3}\cos(\phi)(\sqrt{R^2-y^2}/R)\right.$$

$$\left. + \frac{y^3\sin(\phi)}{6y^2/R^2} - \frac{y^3\cos(\phi)\sqrt{R^2-y^2}/R}{3(-y/R)}\right)$$

$$- f_2\left(\frac{R^3}{3}\sin(\phi)(-y/R) + \frac{R^3}{3}\cos(\phi)(-\sqrt{R^2-y^2}/R)\right.$$

$$\left.\left. + \frac{y^3\sin(\phi)}{6y^2/R^2} - \frac{y^3\cos(\phi)(-\sqrt{R^2-y^2}/R)}{3(-y/R)}\right)\right) - c\boldsymbol{\omega}$$

$$\boldsymbol{\tau} = \hat{z}\left(f_1\left(-2\frac{R^2}{3}\cos(\phi)(\sqrt{R^2-y^2}) - 2\frac{y^2\cos(\phi)(\sqrt{R^2-y^2})}{3}\right)\right.$$

$$\left. + f_2\left(2\frac{R^2}{3}\cos(\phi)(\sqrt{R^2-y^2}) + 2\frac{y^2\cos(\phi)\sqrt{R^2-y^2}}{3}\right)\right) - c\boldsymbol{\omega}$$

$$\boldsymbol{\tau} = \hat{z}\frac{2}{3}\sqrt{R^2-y^2}\cos(\phi)\left(f_1(-R^2-y^2) + f_2(R^2+y^2)\right) - c\boldsymbol{\omega}$$

The equation below shows the torque on the cluster due to the active forces on each substrate, and rotational damping.

$$\boldsymbol{\tau} = \hat{z}\frac{2}{3}\sqrt{R^2-y^2}\cos(\phi)(f_2 - f_1)(R^2 + y^2) - c\boldsymbol{\omega} \tag{3.8}$$

From eq. 3.6 for force and eq. 3.8 for torque we can write down the equations of motion for the orientation as well as the x and y coordinates of the cluster, as shown below.

$$\frac{1}{2}mR^2\ddot{\phi} = \frac{2}{3}\sqrt{R^2-y^2}\cos(\phi)(R^2+y^2)(f_2 - f_1) - c\dot{\phi}$$

$$m\ddot{x} = \frac{1}{2}R^2\left(\pi(f_1 + f_2) + 2(f_1 - f_2)\left(\arcsin(\frac{y}{R}) + \frac{y}{R}\sqrt{1-(y/R)^2}\right)\right)\cos(\phi) - b\dot{x}$$

$$m\ddot{y} = \frac{1}{2}R^2\left(\pi(f_1 + f_2) + 2(f_1 - f_2)\left(\arcsin(\frac{y}{R}) + \frac{y}{R}\sqrt{1-(y/R)^2}\right)\right)\sin(\phi) - b\dot{y}$$

We can then nondimensionalize the equations of motion through the following substitutions:

$$\phi = \Phi$$

$$x = RX$$

$$y = RY$$

$$t = \frac{m}{b}T$$

$$\frac{R^2b^2}{2m}\frac{d^2\Phi}{dT^2} = \frac{2}{3}R^3\sqrt{1-Y^2}(1+Y^2)(f_2 - f_1)\cos(\Phi) - \frac{cb}{m}\frac{d\Phi}{dT}$$

$$\frac{Rb^2}{m}\frac{d^2X}{dT^2} = \frac{1}{2}R^2\left(\pi(f_1 + f_2) + 2(f_1 - f_2)\left(\arcsin(Y) + Y\sqrt{1-Y^2}\right)\right)\cos(\Phi) - \frac{Rb^2}{m}\frac{dX}{dT}$$

$$\frac{Rb^2}{m}\frac{d^2Y}{dT^2} = \frac{1}{2}R^2\left(\pi(f_1 + f_2) + 2(f_1 - f_2)\left(\arcsin(Y) + Y\sqrt{1-Y^2}\right)\right)\sin(\Phi) - \frac{Rb^2}{m}\frac{dY}{dT}$$

$$\frac{d^2\Phi}{dT^2} = \frac{4mR}{3b^2}\sqrt{1-Y^2}(1+Y^2)(f_2 - f_1)\cos(\Phi) - \frac{2c}{R^2b}\frac{d\Phi}{dT}$$

$$\frac{d^2X}{dT^2} = \frac{mR}{2b^2}\left(\pi(f_1 + f_2) + 2(f_1 - f_2)\left(\arcsin(Y) + Y\sqrt{1-Y^2}\right)\right)\cos(\Phi) - \frac{dX}{dT}$$

$$\frac{d^2Y}{dT^2} = \frac{mR}{2b^2}\left(\pi(f_1 + f_2) + 2(f_1 - f_2)\left(\arcsin(Y) + Y\sqrt{1-Y^2}\right)\right)\sin(\Phi) - \frac{dY}{dT}$$

In the limit where the cluster is entirely on one substrate, we can compute the equilibrium speed of the cluster on each substrate by letting the acceleration go to zero, and

$Y > 1$ for the first substrate or $Y < -1$ for the other substrate. Taking the real components of the equations of motion these limits of the system give us the equilibrium speeds as given below.

$$0 = \frac{mR}{2b^2}\left(\pi(f_1 + f_2) + 2(f_1 - f_2)(\pm\frac{\pi}{2})\right)\hat{n} - \vec{v}$$

$$v_{1/2} = \frac{\pi m R}{b^2}f_{1/2}$$

Substituting equilibrium velocities into the equations of motion results in the eqs. 3.1-3.3. Additionally, the value of c due only to friction-like resistance is $c = bR^2/2$. Substituting $c = CbR^2/2$, where C is the ratio of the actual rotational resistance to the frictional angular resistance, results in the following equations of motion.

$$\frac{d^2\Phi}{dT^2} = \frac{4}{3\pi}\sqrt{1 - Y^2}(1 + Y^2)(v_2 - v_1)\cos(\Phi) - C\frac{d\Phi}{dT} \tag{3.9}$$

$$\frac{d^2X}{dT^2} = \left(1/2(v_1 + v_2) + 1/\pi(v_1 - v_2)\left(\arcsin(Y) + Y\sqrt{1 - Y^2}\right)\right)\cos(\Phi) - \frac{dX}{dT} \tag{3.10}$$

$$\frac{d^2Y}{dT^2} = \left(1/2(v_1 + v_2) + 1/\pi(v_1 - v_2)\left(\arcsin(Y) + Y\sqrt{1 - Y^2}\right)\right)\sin(\Phi) - \frac{dY}{dT} \tag{3.11}$$

3.1.4 Discussion.

Collective directed motility is a phenomenon that is widespread in biological systems including cell clusters during tissue development and tumor formation, as well as bacterial biofilms and flocks of birds. In these types of systems it is reasonable to assume that clusters of collectively moving agents move through changing environments, be it a change in air temperature, stiffness in substrate or any other change which could result in speed change. We have used a model which treats a swarming cluster as a single cohesive unit with a preferred direction, to examine the effects of a swarm moving across an interface between two environments due to a change in speed that occurs in each separate environment.

We found that clusters can display different broad behaviors. The most applicable of which is for slow moving swarms with some angular damping. In this case a swarming cluster approaching an interface at an angle will undergo some form of refraction or reflection resulting in a new direction which is predictable by a simple relationship between incident and refracted angle and the ratio of the equilibrium speeds on each substrate. Clusters in this regime can also display total internal reflection at the predictable angle where the refraction angle would exceed $\pi/2$. This regime of our model could represent cell clusters on changing substrates and our predictions could be used to pattern a substrate to direct cluster motion along a desired path.

When the velocities of the cluster is increased on both substrates the trajectories gradually diverge from the predicted refraction angles and reflections found for low velocities where friction dominates cluster motion. This is due to the inertia of the clusters carrying it quickly across the interface with the inability of the cluster to change directions at a comparable rate. As the cluster velocities continue to increase the trajectories become sensitive to initial conditions and rotational damping, due to the cluster interacting multiple times with the interface or spending less time in contact with the interface than necessary for

the cluster to adjust its direction according to the torques present. These kinds of clusters display broad sweeping curved trajectories away from the interface and could provide insight into the impressive collective motion seen in starling flocks and fast moving fish schools, such as sardines.

In the special case where the cluster experiences no angular damping, possibly due to swarms exerting a torque which counter-acts the friction-like resistance that is present in the translational motion, the cluster will either become stuck on the interface for low velocities or stabilize in circular trajectories on a single substrate for high velocities. These types of behaviors may be desirable for certain systems, and our predictions could be used to engineer cell clusters, or robot algorithms to follow desired paths. Trapping a cell cluster on an interface could be useful for separating cells or subjecting them to specific conditions which could then be applied at the interface more easily to cell clusters as individual cells will not display the same kinds of collective modes at an interface. Cell cluster motion has been shown to be controllable by hard boundaries[72], and our results suggest that a similar strategy could be used with softer substrate interfaces which can be crossed to manipulate cell cluster behaviors.

Our results show possible predictive capabilities for slow moving clusters such as cells or bacteria moving across changing substrates, as well as possible insight into ongoing questions such as the behaviors of starling flocks and fish schools as they spiral and curve while they span and cross interfaces between changing environments. Additionally our results suggest possible mechanisms for directing collective systems by way of changing environmental conditions.

3.2   Frustration induced phases in migrating cell clusters

Collective motion is an emergent phenomenon in large groups of individuals where the motion can arise from purely local interactions. This phenomenon occurs across scales in systems ranging from bacteria to fish [12, 11]. Studies of such systems in the thermodynamic limit of infinite size have revealed a number of interesting features including long-range, scale-free correlations and a discontinuous phase transition [26]. These thermodynamic limit studies have spurred interest in hydrodynamic and mean field theories to describe such phenomena [27]. Finite groups display collective motion that closely model schools of fish or flock dynamics with boundaries. Their kinematics are characterized by unique behaviors including guidance by asymmetric boundaries [73] and the ability to simultaneously exhibit different phases of motion [74]. Collective motion of groups was found to exhibit three distinct phases: running, rotating and random [75, 76]. In the running phase, the individuals are all more or less aligned, leading to a large translational velocity of the cluster center of mass. In the random or disordered phase, individual velocities are uncorrelated and there is very little overall motion of the cluster. In the rotating phase on the other hand, the cluster rotates as a whole around a common center. While the running and random phases have analogs in infinite systems, the mechanisms that can give rise to rotations are less clear.

Through simulations, confinement has been shown, to be one mechanism that results in uniform populations of self propelled particles exhibiting rotational modes [45, 77, 78, 79]. Simulations of large groups of unconfined agents can also display rotational phases or milling states where the group rotates in a donut shape under certain conditions [68, 80, 66, 81, 82]. However to achieve these rotational milling states, the agents interact over a range up to tens

of times the size of an individual agent, and form a low density 'hole' at the center, where the defect in the velocity orientation field resides. Groups of cells have also been shown to display such rotations though it is unlikely that cells can interact much beyond their nearest neighbors [44, 83]. This rotational motion has been studied both experimentally and using simulations for small groups of cells confined to different geometries [84, 72, 85, 86]. Perhaps even more remarkably, unconfined cell clusters have also been observed experimentally to show transient rotational phases [87], and this behavior has been speculated to promote chemotaxis.

In this paper, we use an agent-based swarming model, which only allows short-range, nearest-neighbor interactions and unconfined space, similar to previous models found in the literature [23, 24, 51], to address the phenomenon of transient rotations in unconfined clusters. We show that a possible mechanism for driving cluster rotations is density-dependent cell propulsion. This density-dependent propulsion may be caused by contact inhibition of locomotion (CIL), whereby cell protrusions are inhibited by the adhesions between cells [52, 53]. This causes cells at the cluster core, surrounded by other cells, to move slower than those at the edge of the clusters, which have a lower local cell density [88]. This results in an outer rim of cells that move faster than central core ones and display stronger alignment interactions. We also find that decoupling the motion of the rim and central cells suppresses any rotational motion, suggesting that it is the coupling of two systems with different motilities (rim and core) that leads to rotational phases. Specifically, rotations arise in this model when the internal noise is such that the rim cells are in an ordered state with respect to velocity alignment, while the core of the cluster is disordered. The coupling of these two systems (rim around core) results in a frustrated state of the ordered rim being pinned by the disordered core. The whole coupled system is then able to relieve this frustration most effectively by existing in a rotational phase where the more ordered rim is able to pull the disordered core, which is pinning it in place, into a rotational phase. This model successfully captures the dynamics of transitions between the modes of motion and proportions of time spent in each phase observed experimentally [87]. In the experiments, when the cell clusters are subjected to a chemical gradient [50, 89] there is an increase in the proportion of running phase, and a decrease in the rotational phase. This trend is also captured by our model when a chemical gradient is introduced. Furthermore, our model predicts an increase in the proportion of rotating phase with the size of the cluster, which we confirmed with experimental data. Taken together, our results suggest a novel form of frustrated interactions between behaviorally different parts of the same cluster that can lead to different collective dynamics – a finding that may have applications beyond the context of cellular clusters.

3.2.1 Model

Cell clusters are modeled as groups of particles that move with overdamped dynamics in two-dimensional continuous space (see methods section below). Cells are initially arranged in a circular disk, with velocities pointing in random directions. Cell velocities are determined by their internal self propulsion (with magnitude p_i), as well as physical interactions between cells, such as adhesions and collisions [24, 90]. All of these interactions assume that cells communicate with each other by contact within a distance small enough to only include nearest neighbors. The cell diameter is selected from a Gaussian distribution, as uniform cell sizes lead to crystal lattice effects which are unlikely to exist in the experimental cell

system (see Additional information - Lattice indiuced rotations section below). Finally, the velocities of the cells are subject to some uniform and uncorrelated noise ($\vec{\eta}$) due to random traction forces with the substrate and the random nature of the protrusions that cells use for propulsion. Cell positions are then updated according to their individually calculated velocities.

$$\vec{x}_i(t + \Delta t) = \vec{x}_i(t) + \vec{v}_i(t) * \Delta t \tag{3.12}$$

To determine the velocity of individual cells, a couple of interactions are taken into account. First, cells propel themselves in a direction ($\hat{n}$, eq. 3.13) determined by the memory of their own previous polarization and an alignment interaction with the mean orientation of neighboring cells, $\hat{V}$, with interaction strength α.

$$\hat{n} = \frac{\hat{v}(t - \Delta t) + \alpha * \hat{V}}{|\hat{v}(t - \Delta t) + \alpha * \hat{V}|}, \; \hat{V} = \frac{\sum_{n.n.} \vec{v}_i}{|\sum_{n.n.} \vec{v}_i|} \tag{3.13}$$

Cell velocities for each cell are calculated as arising from the forces described here and illustrated in Fig. 3.8(a). The self propulsion magnitude is set by p. Additionally cells experience volume exclusion and adhesion with neighboring cells, which are modeled as arising from a Lennard-Jones force ($\vec{LJ}$) and a spring-like interaction ($\vec{S}$). The spring force is longer range and acts past their nearest-neighbors, as long as it is not interrupted by other cells (Fig. 3.8(a)). This adhesion force acts to maintain compact, cohesive, and roughly circular clusters.

$$\vec{v}_i(t) = p * \hat{n} + \epsilon * \vec{LJ} + k * \vec{S} + \vec{\eta} \tag{3.14}$$
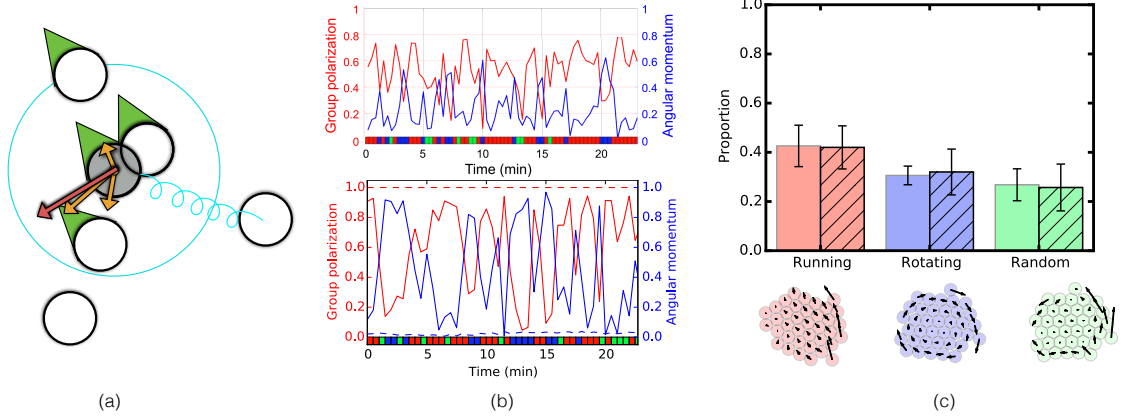
Figure 3.8: (a) Schematic for the model. Green direction indicators show the direction of the neighbors of the gray cells, and the green indicator on the gray cell shows the alignment interaction $(\hat{V})$. The orange arrows show the Lennard-Jones interaction with each neighboring cell and the red arrow is the total LJ interaction $(\vec{LJ})$ on the gray cell. Finally, the blue spring denotes the cell-cell adhesion interaction $(\vec{S})$. Note that it only exists between the gray cell and its second nearest neighbors that do not have cells interrupting the path between them. (b) Time series of the group polarization and angular momentum of the cell cluster. The colors along the bottom axis show the phase of the system with time (running – red, rotating – blue, and random – green) for experimental data (top) and simulations (bottom), for a uniform cluster (dashed) and a cluster with behavioral heterogeneity (solid, corresponding to the point marked in Fig. 3.9b). (c) The proportion of time that the cluster spends in each phase (simulations (plain) and experiments (cross-hatched)), along with a typical illustration of what each phase looks like in the simulations, with velocity vectors as black arrows. The cluster size for simulations is $N = 37$ cells, while experiments are for an average cluster size of 50.

Phase characterization

We identify the mode of motion of the cell cluster by measuring the polarization $(\mathcal{O})$ and angular momentum $(\mathcal{A})$

$$\mathcal{O} = \frac{1}{N} \sum_{i=0}^{N} \hat{v}_i \tag{3.15}$$

$$\mathcal{A} = \frac{1}{N} \sum_{i=0}^{N} \hat{v}_i \times \hat{r}_i$$

We can also calculate the average expected velocity of the cells assuming perfect alignment, or perfect rotational motion (see Additional information - Average speeds section below). We define the running phase to occur when the group polarization $(\mathcal{O})$ is greater than 0.5, and the average cell velocity is over half the expected velocity assuming perfect alignment. Similarly, the rotational phase occurs when the cluster angular momentum $(\mathcal{A})$ is greater than 0.5, and the average cell velocity is over half the expected velocity assuming perfect rotation of the cluster. Finally, the random phase is defined for all other

combinations of $\mathcal{O}$, $\mathcal{A}$, and average velocity. These definitions are made to ensure consistency with the definitions in the experimental analysis [87]. In the experiments, malignant B and T type lymphocytes were placed in a chemical gradient of CCL19, where they assemble into clusters and move towards higher CCL19 concentration. Automated analysis of video recordings of the cell clusters was utilized to extract velocity vectors of individual cells, which were then used to compute polarization and angular momentum as functions of time (see [87] for details). Using the criteria described above, we can then label the phase of motion of the cluster for each time point. We then calculate the proportion of time that the cluster spends in each of the three phases throughout a simulation in a manner that allows for experimental comparison.

3.2.2 Results

Uniform cell clusters

In the case where all cells within the cluster behave identically, the cluster remains in a single phase throughout the simulation. The dashed line in Fig. 3.8 (b, bottom) shows a time trace for a cluster in the running phase where the group polarization remains high and angular momentum remains low throughout. When compared to a time trace of the same quantities measured in experimental cell clusters (Fig. 3.8 (b, top)), the features of the time traces are very different. In the experiments, the group polarization and angular momentum fluctuate from high to low values corresponding to spontaneous transitions of the cluster between various phases of motion. In the simulations, on the other hand, the cluster undergoes a transition from a running phase to a random phase only with increasing noise or decreasing propulsion. Fig. 3.9a shows the proportion of time spent by clusters in each of the three phases plotted against noise and propulsion. The diagonal line of the transition between running at low noise and random at high noise is the well known noise-driven transition seen in Vicsek swarming models [26, 16, 91].

The running and random phases seen here are similar to those seen in experiments; however, the transition between the running and random phases in phase space is very sharp and there is very little overlap or mixing of the phases. Experimentally, cell clusters are observed to spontaneously switch between running, rotating, and random phases which means that they coexist within this parameter space. Alternatively one could say that cells change their internal parameters, such as the propulsion, p, or noise, η, so that they cross over the transition between the phases. However, it is implausible for the entire cell cluster to change internal parameters in a coordinated way. Additionally, the uniform clusters show a very low level of cell rearrangement or fluidity within the cluster, whereas, in the experiments, cells are observed to move between the rim and the core of the cluster regularly. We therefore conclude that additional features of the real system must be incorporated into the model to recapitulate a rotational phase and transitions between phases within a single set of parameter values, as well as large scale cluster rearrangement.

Introducing heterogeneous behavior

An aspect of cellular behavior that is missing in this description is the possibility that cells may behave differently in different regions of the cluster, say the periphery or the interior. Rim cells have increased propulsion compared to inner-cluster (core) cells due to reduced CIL, which causes cells adhered to other cells to form fewer protrusions than cells which

have more open space around them. We implement this effect by scaling the propulsion with the number of neighbors, increasing for cells with fewer neighbors

$$p_i = p_{core} + \frac{3}{7} * (p_{core} - p_{rim}) * (n_i - 6) \tag{3.16}$$

Here, n_i is the number of neighbors around cell i. p_{rim} and p_{core} are the propulsion of the rim cells (average of 3.67 neighbors) and core cells (average of 6 neighbors) respectively. A similar inverse relation between local density and propulsion (and therefore, alignment), was explored for a semi-infinite system in [92].

This variation of cell propulsion causes the rotating phase to emerge, and to coexist with the other phases, as seen in experiments. There is now a region in parameter space where there is a peak in the rotational phase at low values of p_{core} and intermediate noise (Fig. 3.9b). In this region, there are proportions of all three phases which are close to those seen in experiments. The point highlighted in Fig. 3.9b is an example of a location in parameter space where the simulations closely match the experiments. The time series for the group polarization and angular momentum at this point in parameter space is shown in Fig. 3.8 (b, bottom), and agrees well with the experimental time series. Furthermore, when the proportion of time spent in each of the three phases is compared to the experimentally measured values, they match very closely (Fig. 3.8c). We next investigate, more closely, the mechanism that drives the rotating phase.

Cluster rim to core coupling

The values of propulsion for individual cells in our simulation with heterogeneity are mostly close to p_{core}, except for those near the periphery where it rapidly climbs to an average of p_{rim} (see Additional information - Density dependent propulsion section below). This prompts us to consider whether the behavior of the system can be understood as arising from the coupling of two different systems – a ring-like rim with a higher propulsion and a uniform core with lower propulsion. We first examine the rim cell system by confining a ring of cells to a circular shape and assigning them a fixed value of propulsion ($= p_{rim}$) independent of neighbor number. This results in the phase diagram shown in Fig. 3.10, where the contours are boundaries of regions where the proportion of time spent in the corresponding phase exceeds 30% and 50%. This phase space shares some characteristics with the uniform cluster phase diagram (Fig. 3.9a), such as the transition from a running to a random phase with increasing noise or decreasing propulsion, and the lack of a rotational phase. Due to the lower number of neighbors in the rim case, however, the slope of the diagonal running-random transition line is smaller compared to the case with a uniform cluster.

We next couple the rim cells to the core, resulting in a ring of cells confined to a circle with propulsion $p_{rim} = 8$, positioned around a core of cells with propulsion p_{core}. The black dashed line in Fig. 3.10 shows the noise value below which a ring of cells with $p_{rim} = 8$ would be ordered (or in the running phase more than 30% of the time); while above the black solid line we expect a cluster with an average uniform p given by eq. 3.17 to be disordered (random phase greater than 30%).

$$p_{average} = \frac{p_{rim} * N_{rim} + p_{core} * N_{core}}{N} \tag{3.17}$$

We notice that there is a triangular region between the dashed and solid black lines at low p_{core} and intermediate noise where the rim should be in its ordered state while the core would be in the disordered state. This suggests the possibility that when the rim is pinned in place by the random phase of the core cells it could relieve the frustration and maximize order by existing in a rotational phase moving around the core.

Indeed, when we couple the ordered rim to the random phase core in this parameter regime, we find a peak in the rotating phase (Fig. 3.10, solid contours). The fact that the peak in the rotational phase does not exist for the rim or core alone but emerges when the two systems are coupled suggests that the rotational phase is driven by the coupling of the ordered rim to the disordered core.

There are some differences between the ring-disk confined system and the full unconfined model shown in Fig. 3.9b, but these are mainly due to affects arising from the confinement of the rim cells to a circle. Indeed, relaxing the confinement of the rim cells, while still treating the cluster as two different coupled systems of the rim cells with higher propulsion around core cells with lower propulsion recovers the original, fully heterogeneous model phase space (see Additional information - Rim/core cluster model section below). Taken together, these results suggest that it is the coupling between the disordered core and ordered rim that is the mechanism behind the cell cluster rotations seen experimentally.

Transitions into and out of rotating

While we have shown that the running, rotating, and random phases can coexist within our model with heterogeneous neighbor-dependent propulsion, we have not yet examined the dynamics of the transitions between these phases. To do this, we quantify these transitions by monitoring changes in the overall topological properties of the phases, which are easier to track. In particular, note that in condensed matter systems, including active matter [93, 94], phase transitions may be driven by the interactions and dynamics of topological defects [95]. We first take a coupled rim-core cluster with rim cells confined to a circle and project the rim cell velocities onto the confining circle. We then identify a defect in this effectively one-dimensional velocity field as a point where the velocity projections switch directions. Note that the defects, as we have defined them, exist when there is no defect in the full velocity field of the entire cluster in its running phase and vanish when there in fact is a vortex in the cluster in its rotating phase (+/- 1 defect in the director field).

Fig. 3.11a shows these defects for a cluster in the running phase and the rotating phase. In the running phase, the cluster has two defects of opposite signs at roughly opposite sides of the cluster. The formation and spreading apart of a defect pair coincides with the transition from rotating to running phase while the annihilation of the pair results in the running to rotating phase transition. By measuring the frequency of occurrence of any given number of defect pairs in each cluster phase, we investigate the correlation between the phase and number of defect pairs (Fig. 3.11b). We see a large peak in the rotating phase for zero defect pairs and a peak in the running phase for one defect pair. The random phase has a much broader peak around two or three defect pairs, suggesting that the random phase could occur when multiple defect pairs spontaneously form.

To observe the effective interactions of defects with each other, we calculate the pair distribution function ($g(r)$) for the spacing between two individual defects when a single pair exists. Fig. 3.11c shows the pair distribution function calculated over all time throughout a simulation, independent of what phase the cluster is in at any particular point in time.

We see that for parameter values when the cluster is predominantly in the running phase, the pair distribution indicates that the two defects will repel and largely exist at maximum separation. When the cluster is mostly in the rotating or random phase (Fig. 3.11c inset), there is a small peak at zero separation, implying that there may be a small effective attractive force between the defects if they get within one cell diameter of each other ($r_c \sim 30$). At longer ranges, the interaction is repulsive, though the slope is much smaller for both of these cases than in the running case, so the defects only repel weakly, increasing their chance of annihilating and transitioning out of the running phase. Thus, system-wide parameters have a significant influence on the interactions between topological defects, which in turn controls the dynamics of the defects, the formation or annihilation of which are correlated with cluster phase transitions.

Cluster size dependence

We next examine the effect of cluster size on the phase diagram. Fig 3.12a shows regions of the parameter space with a proportion of rotating phase greater than 30% for different cluster sizes. Compared to the predictions of the simulations regarding the proportion of the rotating phase, the predictions regarding the running and random phases have a very large spread across the parameters tested. Thus, we focus on the more significant rotational phase shown here (see Additional information - Size dependence section below). Again, the dashed black line shows the noise value below which the rim alone would be in an ordered phase, while the colored dashed lines show the transition between the running and random phases for a uniform system of average p (eq. 3.17), for each different system size. Our results indicate that larger clusters have a higher proportion of rotational phase while smaller clusters are less likely to rotate.

This is consistent with the idea that the coupling-induced rotational phase only exists in the area of phase space where the rim propulsion would result in an ordered state (running phase greater than 30% of the time; below the dashed black line) while the average p of the whole cluster would lead to a disordered state (random phase greater than 30% of the time; above the colored dashed lines for each size). Larger systems have a higher proportion of core cells and therefore will have a larger proportion of the phase space where the average p results in a disordered cluster (because p_{core} is always lower than p_{rim}) while the rim remains ordered, leading to a larger overlap of the two and a more stable rotational phase. Fig. 3.12(a inset) shows the comparison between experimental and simulation values, where the blue points are the experimentally measured proportions of rotating phase against cluster size, and the red shaded region shows the size dependence of the simulations with the parameter values marked by black crosses in Fig. 3.12a. Although these parameter values were chosen based solely on the proportions of all phases exhibited by a cluster of size $N = 37$, the dependence on system size seen in the simulations is very similar to that of the experiments, further supporting the idea that the rim/core coupling is a likely mechanism for experimental cell cluster rotations.

Cluster fluidity

Exchanges between the periphery and the interior of the cell clusters were proposed to have an important functional role in exposing 'fresh' cells with unsaturated receptors to the chemical gradient [87]. To examine this feature of our clusters, we look at the fluidity

of a cluster as measured by the rate of exchange between core and rim cells. A rim cell is defined as any cell with an exposed edge larger than a single cell diameter. We then average the number of cells which switch between the rim and the core in each time step to get a measurement for the cluster fluidity.

We measure this exchange rate for the original, fully heterogeneous neighbor-number-dependent propulsion model (phase space in Fig. 3.9b). Fig. 3.12(b inset) shows contours for the fluidity across parameter space. It turns out that the fluidity of the cluster is significantly higher when the cluster shows a majority of running or rotating phase compared to the random phase. This is presumably due to the fact that the large scale rearrangements or rim/core cell exchanges happen when the rim cells move past the slow moving core cells and then mix back into the cluster. This is why the fluidity drops for high p_{core} values, approaching p_{rim}. Fig. 3.12b shows the dependence of the rim/core exchange on cluster size for the simulations, as well as the experiments (cross-hatched bars). The trend of decreasing rim/core exchange with increasing cluster size is more dramatic in the simulations, but is maintained between both experiments and simulation, further supporting a rim/core coupling as the mechanism for rotational phases in cell clusters.

It should be noted that the simulations slightly overestimate the proportion of the running phase in smaller clusters at the expense of the random phase. We speculate that this might be a signature of cellular clusters maintaining a roughly constant effective p_{rim} across cluster sizes, perhaps by sensing curvature. In this case, our simulations are essentially overestimating the effective p_{rim} value because the rim cells in smaller clusters have fewer neighbors, and p increases linearly with decreasing number of neighbors. This would result in a slight overestimation of the running phase with decreasing cluster size at the expense of the random phase seen in the experiments (see Additional information - Size dependence section below). Similarly, for large cluster sizes, the simulations underestimate the effective p_{rim}, leading to a higher proportion of the random phase at the expense of the running phase, as well as an underestimation of the rim/core exchange in simulations due to the fact that about 60% of the exchanges that take place occur during the running phase in both experiments and simulations.

Cell clusters in a chemical gradient

Cell clusters can chemotax robustly up a chemical gradient [87] and it has been shown that such a collective chemotactic motion can be obtained by cells at the cluster rim having a propulsive force normal to the surface of the cluster with a magnitude that depends on the local concentration of the chemokine [87, 96, 97]. We are interested in how such a gradient would affect the proportion of time the clusters spend in each of the different phases. To implement a chemical gradient into our model, we introduce an additional term into the calculation for the cell propulsion direction, $\hat{n}$, by replacing $\alpha * \hat{V}$ by $\alpha * \hat{V} + \vec{g}$ in eq. 3.13), where

$$\vec{g}_i = gc'y \sum_j^{p.a.n.} \vec{f}_j \tag{3.18}$$

and the sum j is over each distinct pair of adjacent neighbors of cell i. $\vec{f}_j$ is a vector pointing in the direction bisecting the angle subtended by the centers of the cells of the neighbor pair at the center of cell i, with a magnitude equal to the arc length between the

two neighbors (see Additional information - Methods, chemotaxis section below). Here, g reflects the strength of the influence on propulsion direction from the chemokine gradient per unit distance, of exposed cell edge arclength, c' is the change in chemokine concentration per unit distance and y is the distance (in microns) from the 0 ng/ml concentration point. This results in a gradient force in the direction of the most vacant region around a cell, with a magnitude proportional to the size of the vacancy, causing a large outward force on rim cells and negligible force on core cells, resulting in an overall upward drift due to the unbalanced forces [87].

We introduce such a chemical gradient to a system with running, rotating and random proportions close to those measured experimentally in the absence of a chemical gradient. We find that the gradient leads to cluster motion up the gradient as anticipated, and observed experimentally. We then measure the changes in the proportion of phases as a function of the gradient (shown in Fig. 3.12c). With increasing gradient, we find an increase in the proportion of the running phase and a decrease in the amount of the rotating phase, similar to what is seen experimentally, (Fig. 3.12c inset) while the random phase proportion stays essentially unchanged.
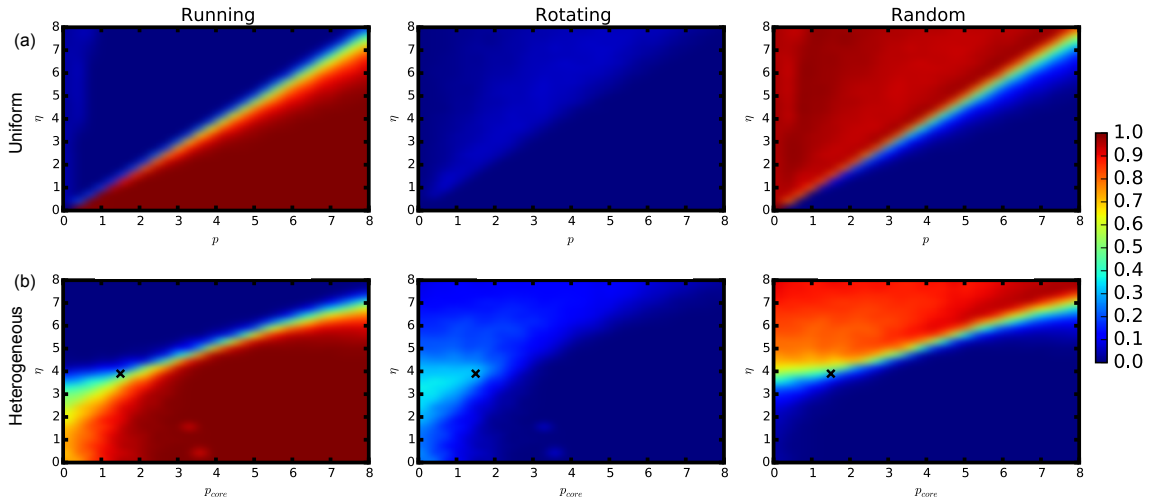

Figure 3.9: (a) Proportion of time spent by the cluster ($N = 37$ cells) in each of the three phases plotted against propusion p and noise $|\vec{\eta}|$ for a cluster where all cells behave identically. (b) Phase diagram of the proportion of time spent in each of the three phases for a system with neighbor-number-dependent propulsion where the rim cells (those with 3.67 neighbors) have a propulsion of $p_{rim} = 8$. p_{core} is the propulsion of core cells (those with 6 neighbors), and η is the magnitude of the noise. The black 'x' shows the point where the time series and phase proportions shown in Fig. 3.8 are taken.
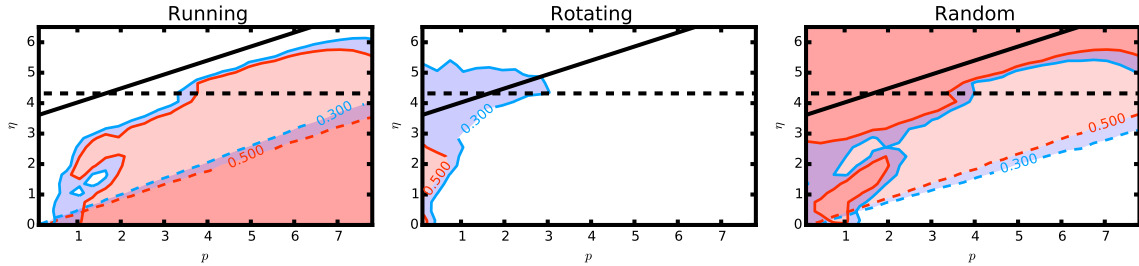
Figure 3.10: Proportion of time spent by the system in each of the three phases as a function of propulsion p and noise $|\vec{\eta}|$ for a ring of 18 cells confined to a circle with propulsion $p_{rim} = p$. Dashed contour lines indicate regions (shaded) where the proportion of time spent in the corresponding phase exceeds 30% (blue) and 50% (red). Solid contour lines show the same contours but for the rim confined to a circle with $p_{rim} = 8$ coupled with a core of cells with $p_{core} = p$, and a full cluster size of $N = 37$. Note that the rotational phase only has non-zero values for the coupled system. The horizontal dashed line marks the noise value below which the rim alone would be ordered (greater than 30% running phase) with $p_{rim} = 8$, and the diagonal solid line marks the region above which a core with an average propulsion set by eq. 3.17 (with $p_{core} = p$) is disordered (greater than 30% random phase).
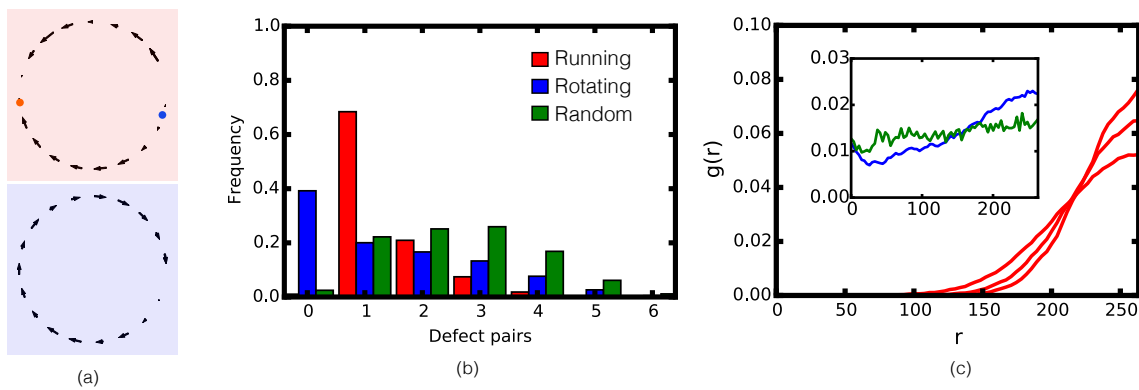

Figure 3.11: (a) Velocities of the rim cells of a 37 cell cluster which are confined to a circular shape projected onto the circle. In the running phase (red), there are two defects of opposite signs in the velocity field, denoted by the orange and blue points. There are no defects in the rotating phase (blue). (b) The proportion of the number of defect pairs for each phase, with a peak at zero defect pairs for the rotating phase (blue), and one defect for the running phase (red). (c) The pair distribution function plotted against the separation between two defects when only one defect pair exists for parameters where the cluster primarily displays a running phase (note that g(r) is calculated over the whole simulation, independent of specific phases at any given point in time). (c - inset) The pair distribution function for points in parameter space dominated by rotating (blue) and random (green) phases.
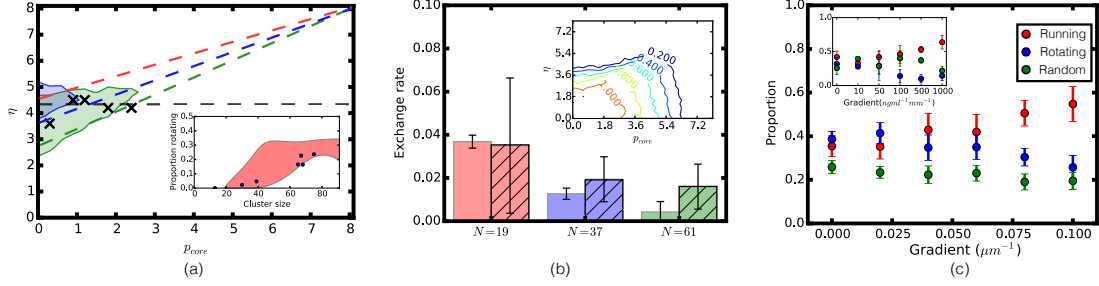
Figure 3.12: (a) Proportion of time spent in the rotating phase by a system with neighbor-number-dependent propulsion as a function of p_{core} and noise $|\vec{\eta}|$ for $p_{rim} = 8$. The black horizontal dashed line marks the noise value below which the rim alone would be ordered (corresponding to the dashed transition line in Fig. 3.10 with $p_{rim} = 8$). The diagonal lines show the noise value above which a uniform system with average propulsion p would be disordered (red: $N = 19$, blue: $N = 37$, and green: $N = 61$). The shaded regions are where the clusters spend at least 30% time in the rotational phase, with the same color scheme (blue: $N = 37$, and green: $N = 61$; note that there is no red shaded region). (a - inset) The dependence of the proportion of rotating phase on system size. The shaded red region shows the range of dependence for a spread of parameter values marked with black crosses in the main figure. The experimental measurements are shown as the blue points. (b) The fluidity of the cluster measured as the rate of exchange between the core and rim cells of the cluster, for several systems sizes, for both simulations (plain bars), and experimental data (cross-hatched bars). (b - inset) Contours for the fluidity of the cluster over the p_{core}-η parameter space. (c) Simulated proportion of each phase (see legend) plotted with increasing chemical gradient ($gc'r$ in eq. 3.18, where r is the cell diameter), along with experimental data in the inset. The concentration gradient of chemokine in the experiments is measured in (ng/ml)/mm and shown on the x-axis for the inset.

3.2.3 Methods

Basic model

The exact form of the $\vec{LJ}$ and $\vec{S}$ interactions are given below, along with parameter values used in these simulations. Here, r is the average size of the two interacting cells, and the spring interaction exists between $n.n.n.$ which are next nearest neighbors, with σ_j taking a value of 0 when there is a cell between cell i and next nearest neighbor j, and 1 otherwise.

$$\vec{LJ} = -12 * \sum_{j}^{n.n.} \left[\frac{r^{12}}{d^{13}} - \frac{r^6}{d^7} \right]$$

$$\vec{S} = - \sum_{j}^{n.n.n.} \sigma_j * \vec{d}_{ij}$$

Chemotaxis

The chemical gradient force is introduced as the sum of vectors pointing between each adjacent neighbor pair for each cell. Fig. 3.13 is a schematic demonstrating this gradient

Parameter	Description	Values
N	Number of cells	7 to 91
Δt	Time step	0.01
α	Strength of alignment interaction.	6
$|\vec{\eta}|$	Noise magnitude.	0 to 8
ϵ	Strength of Lennard-Jones interaction	18
k	Strength of spring force	0.1
p_{core}	Propulsion value for core cells.	0 to 8
p_{rim}	Propulsion value for rim cells	0 to 8

Table 3.1: Parameters

force, where the purple arrows show the force between each individual pair of adjacent neighbors and the green arrow shows the sum, or the overall gradient force on the gray cell which can then be scaled with concentration as described in the main text in the section 'Cell clusters in a chemical gradient'.
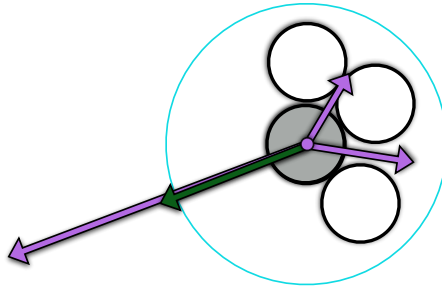

Figure 3.13: A schematic illustration of the chemical gradient force on the gray cell. The purple arrows show the force between each pair of adjacent neighbors while the green arrow shows the over all outward gradient force.

3.2.4   Additional information

Lattice induced rotations

Fig. 3.14 shows the parameter space for cell clusters with uniform cell size. The rotational phase seen at low values of noise and intermediate p_{core} is caused by lattice vibrations, which are phonon-like modes within the crystal structure of the cluster (see video S1), somewhat similar to [103]. To verify that the lattice structure is the mechanism behind the rotations we introduced polydispersity in the size of the cells. We select the sizes of the cells from a Gaussian distribution with a spread of 10% of the average size. The phase diagrams shown in the main text are for polydisperse clusters and it can be seen that these lattice induced rotations become completely suppressed when the polydispersity is introduced (see video S2, equivalent to S1 but with polydisperse cells, and Fig. 2a in main text), and only the peak in the rotational phase for intermediate noise and low p_{core} remains, though it is

slightly reduced. This suggests that the rotations seen experimentally are not induced by lattice vibrations in the structure of the cell cluster, since they would then be suppressed by the polydisperse nature of the cells.
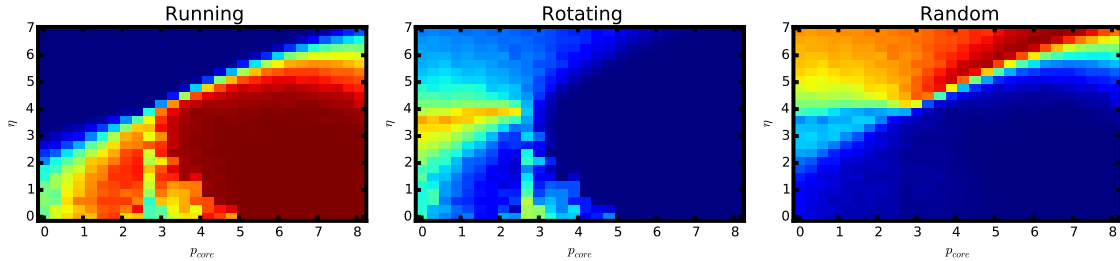

Figure 3.14: Full cell cluster model with uniform cell sizes resulting in lattice effects such as the peak in the rotational phase at low noise and intermediate p_{core} values.

Average speeds

The expected average speed of cells in the running phase is the weighted average of the propulsion of all the cells:

$$\langle v_{run} \rangle = \frac{p_{rim} * N_{rim} + p_{core} * N_{core}}{N} \tag{3.19}$$

When the cluster is in the rotational phase the average speed is adjusted to account for the relationship between cell radius from the center of the cluster (center of rotation) and the speed of the cells. This results in the following expected average speed of cells in the rotational phase:

$$\langle v_{rot} \rangle = \frac{7}{18}(p_{rim} + 2p_{core}) \tag{3.20}$$

The average speed of the cells in the cluster is then compared to these expected average speeds to identify the phase of motion along with order and angular momentum as described in the main text under the 'Phase characterization' section.

Density dependent propulsion

When cell propulsion is scaled with local density due to contact inhibition of locomotion, the core cells or those closer to the center have a propulsion close to p_{core}, while past a certain radius the propulsion rises sharply to a higher propulsion value. Fig. 3.15 shows the value of the propulsion for cells vs. the distance from the cluster center of mass (d_{com}). The blue line shows the full model with neighbor-number-dependent propulsion while the green line shows the propulsion when the rim and core cells are identified by distance from the cluster center of mass (rim/core coupled system model as described in the main text section 'Cluster rim core coupling').
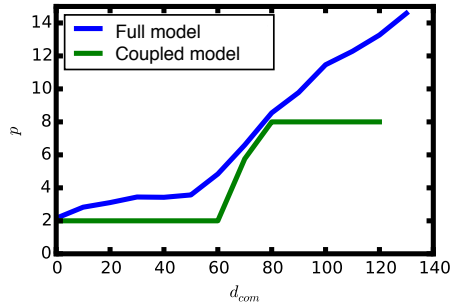
Figure 3.15: The propulsion (p) of cells plotted against distance from the cluster center of mass (d_{com}). For both the full model and the rim/core coupled model the propulsion starts low and then at distances where the cells are at the rim rather than the core, the propulsion p increases to a higher value.

Rim/core cluster model

The full phase space associated with the solid contour lines in Fig. 3 is shown in Fig. 3.16. This is for a system where the rim cells of the cluster are confined to a circle with a propulsion of $p_{rim} = 8$ and the core cells are free to move within the circle of rim cells with a propulsion p_{core} plotted on the x-axis. We can see some features similar to the full model such as the triangle of rotating phase when the core prefers a random phase while the rim prefers a running one. This supports the description of the coupled rim/core systems resulting in the rotational phase.

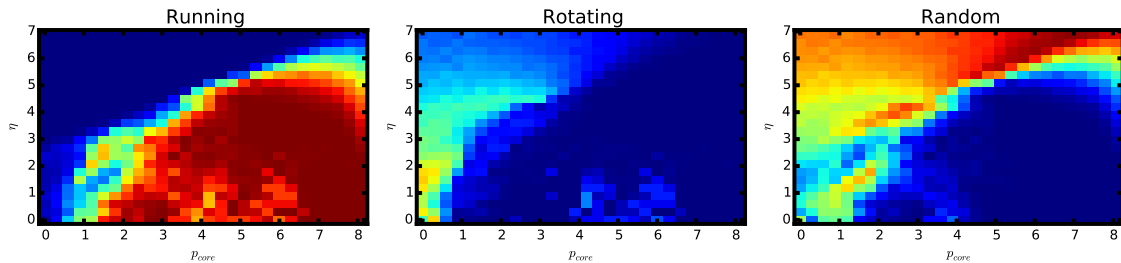Figure 3.16: The rim/core binary propulsion model with the rim cells confined to a circle.

When the circular confinement of rim cells is relaxed and the rim cells are free to move, keeping the propulsion binary between the rim cells with $p_{rim} = 8$ and the core cells with p_{core} (shown on the x-axis) independent of neighbor number, we recover a phase diagram (Fig. 3.17) very similar to the full model shown in Fig. 2b.
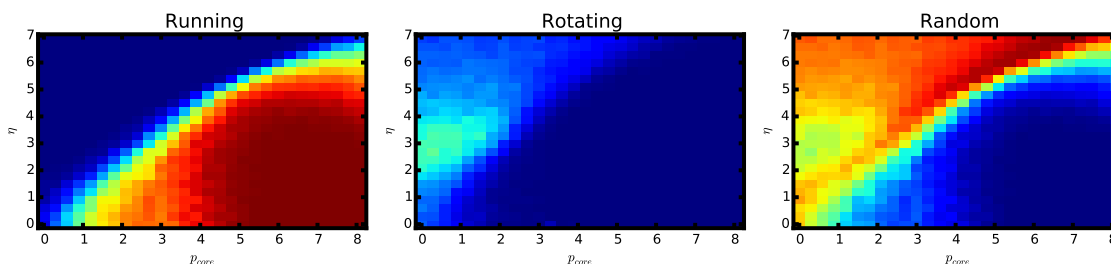
Figure 3.17: The rim / core binary propulsion model with the rim cells free to move and unconfined.

Size dependence

Fig. 3.18 shows the proportion of time spent in each of the three phases for clusters of varying sizes. The experimental clusters are shown as blue dots, and the running and random phases are noisy and have almost no correlation with cluster size. Note that the simulations for larger clusters have little predictive capabilities as evident from the large spread in the calculated values. It is also likely that very small experimental cell clusters may fracture and reform frequently which is disallowed in the model, leading to the larger discrepency between experiments and simulations for very small clusters. The rotating phase, however, has a much narrower spread of proportions in the simulations and an increase with system size. The increase in rotational phase with cluster size is also observed in the experimentally measured proportions.
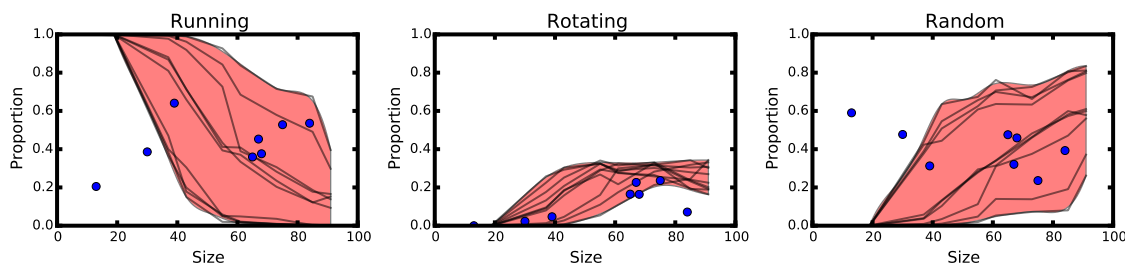

Figure 3.18: The size dependence of all three phases.

Varying rim propulsion

Fig. 3.19 shows the dependence of the phases on p_{rim}. After an initial low start of the rotational phase for low p_{rim}, the difference between p_{rim} and p_{core} becomes large enough and there is a peak in the rotational phase before it gradually decreases and the running phase gradually increases with increasing p_{rim}. If experimental cell clusters increase p_{rim} with cluster size by some rim curvature sensing mechanism in the cells, this would account for a couple of small differences in the cell clusters. The first of these is the slight overestimation of the rotational phase and the underestimation of the running phase in large clusters in the experiments. Additionally, about 60% of the rim/core exchange that takes place in cell clusters occurs during the running phase with 20% in each of the rotating

and random phases. With an increase in the running and decrease in the rotational phase in larger clusters, if they have a higher p_{rim}, the slight underestimation of cluster rim/core exchange in the simulations compared to experiments in large clusters (Fig. 5b) would be accounted for as well.
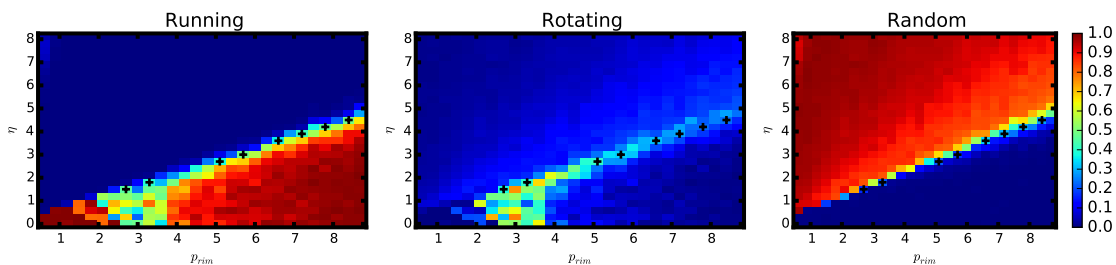

Figure 3.19: Cluster phase space with p_{core} fixed to 0.5 and scanning over p_{rim} up to 8.

Solid-body-like rotations

The rim of the cluster is able to drag the core around with it resulting in solid-body-like rotations. Fig 3.20 shows the percent difference in angular rotation speed of the core of the cluster compared to the rim. While the amount of slip occuring is slightly higher for clusters with a larger difference in p_{core} and p_{rim}, the amount of slip is still small enough that the rim is dragging the core around with it, resulting in a solid body like rotation.
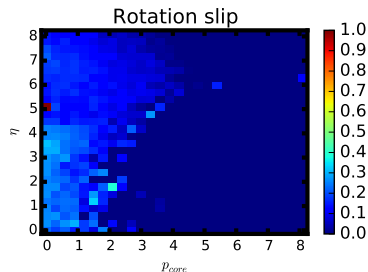
Figure 3.20: Rotational slip of outer rim around the inner core, for the full original model with no confinement.

Fluidity vs. gradient

As the chemical concentration gradient increases, the cluster spends an increasing amount of time in the running phase robustly moving up the gradient. Since the rim/core exchange takes place predominantly in the running phase, we would expect an increase in rim/core exchange with increasing gradient. This is verified by the simulations in Fig. 3.21 which shows the increasing amount of rim/core exchange that takes place with increasing chemical concentration gradient, for the simulations shown in Fig. 5c.

Figure 3.21: Amount of rim/core exchange plotted against chemical gradient.

Chapter 4

Conclusion

Hydrodynamic and agent based models have led to the discovery of many phases and transitions in active systems, typically systems are treated as homogeneous and in a controlled environment. In this dissertation I have investigated the effects of heterogeneity in agent behavior on collective motion systems with finite size. Behavioral het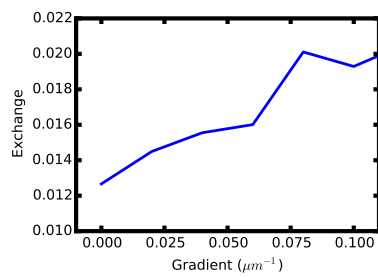erogeneity can exist in nature in the form of mixed populations with variable behavior or as a result of an environmental change. From these perspectives I have used agent based modeling to investigate collective motion with heterogeneous behavior.

Mixed populations

In systems where collective motion exists with mixtures of aligning and non-aligning agents a cluster that is unable to fracture will be able to sustain a fraction of non-aligning agents that can be estimated from a mean field calculation of relative alignment and cohesive interaction strengths. This fraction can be found from parameters of the system that can be measured experimentally in any natural collective system, such as speed, reaction time, and spacing. Natural systems can also adjust their non-aligner carrying capacity on the fly by changing properties such as their speed or spacing. Additionally if the cohesion of the system is sufficiently low for fracture to be possible the system will break apart into smaller clusters which will exist at a non-aligning fraction close to the critical non-aligner carrying capacity of unfracturing swarms. This means that in a system where non-aligning has a tendency to increase due to disease spread, malfunction, or some evolutionary fitness advantage of non-alignment, natural systems can fracture and effectively sort out excess non-aligners to self regulate composition. The carrying capacity for non-alignment can also be adjusted by natural systems on the fly by regulating properties of the system such as speed, reaction time or spacing.

A similar mixed population of heterogeneous agents can exist in the form of a mixture of high and low noise agents. We utilized four variations on common swarming models found in the literature to investigate the effects of mixed populations of different noise levels. We found that an increase in fraction of high noise agents can drive a similar order to disorder transition and the nature of this transition depends on the model details. In models where the physical collision interactions are treated separately from the self-propulsion of the agents, allowing for agents to be slowed down by collisions and not all move at equal speeds results in fracturing of clusters almost always resulting in small ordered groups rather than a gaseous state of individual agents, with random directions of travel. In models where

the cohesiveness is calculated as part of the self-propulsion direction with alignment there is a cohesion driven order to disorder transition in addition to the typical noise driven transition seen in collective motion systems. If the alignment interaction takes the form of a standard Vicsek alignment where agents follow the average direction of their neighbors and this interaction is normalized then there is an order to disorder transition which is entirely dependent on the fraction of high and low noise particles and the level of noise in the high noise population is unimportant. However in other types of alignment interactions of a reorientation towards instantaneous travel direction or an unnormalized Vicsek-like interaction there is an order to disorder transition that is driven by the average noise of the population rather than the fraction of high and low noise agents.

Environmentally driven heterogeneity

Collective systems where agents behave differently depending on their local environment can exhibit unique phases of motion and interesting collective modes. We found that treating a flock as a single cohesive unit and observing it as it crosses a boundary between multiple environments causes the flock to turn and rotate in interesting paths. We found that the important features of a flock crossing a boundary are the speed of the flock and whether agents within the flock prefer to continue rotating once they have begun or tend to settle towards a straight trajectory in the absense of outside influences. Fast moving flocks that have persistant turning behaviors will begin to rotate upon crossing a boundary between environments where agents move faster in one environment than the other, and then upon completely entering the new environment will equilibrate to travel in a circular path. If the fast moving flock does not show a preference to continue turning it will show large sweeping arcs as it crosses into a new environment but eventually settle into a straight path, somewhat eminiscent of the large sweeping arcs seen in bird flocks. Slower moving systems show very different behaviors than the fast ones. A slow moving flock crossing an interface between a fast and slow environment will become stuck at the interface always turning around and returning from the new environment to the interface if the agents persist in turning behaviors. However a slow moving flock which relaxes to a straight trajectory will turn while it is in contact with the interface and establish a new direction to travel in upon completely crossing into the new environment which depends on incident angle as well as difference in speeds in the two environments. This relationship bears a remarkable resemblance to Snell's law for light changing between media with different indices of refraction and allows us to write down a simple predictive equation for the trajectory of a swarm crossing an interface between slow and fast environments. We even observe a critical angle beyond which total internal reflection occurs. These results offer simple predictive capabilities for flock motion between varying environments as well as posible mechanisms for directing collective systems by way of patterning environments to promote travel along a desired path.

We also looked at an experimental system of cell clusters which vary their behaviors based on local environment due to contact inhibition of locomotion, which acts to slow down cells which have a higher local density. This density dependent propulsion leads to a frustrated system where cells at the rim of a cluster with lower local density move faster which prefer an ordered state while cells at the core of the cluster with high local density move slowly and are unable to reach a consensus direction. The system manages this frustration by the rim rotating around and pulling the core with it into a rotational state. Taken together, our results show that the rotations induced by rim-

core coupling hold across a range of system sizes, propulsion strengths, noise values, and even in the presence of directional forcing. They may even extend into three-dimensional rotations [99, 100, 101, 102], suggesting that the coupling between two swarming systems which are in different ordered phases can lead to interesting behaviors not seen in either system alone. Heterogeneous behavior within a single group is a robust mechanism that cells or other types of swarming organisms may use to enhance rotating phases or other phases that would be unlikely or impossible to achieve otherwise.

Bibliography

[1]   William Bialek, Andrea Cavagna, Irene Giardina, Thierry Mora, Oliver Pohl, Edmondo Silvestri, Massimiliano Viale, and Aleksandra M Walczak. Social interactions dominate speed control in poising natural flocks near criticality. *Proceedings of the National Academy of Sciences of the United States of America*, 111(20):7212–7, 2014.

[2]   A. Cavagna, A. Cimarelli, I. Giardina, G. Parisi, R. Santagati, F. Stefanini, and M. Viale. Scale-free correlations in starling flocks. *Proceedings of the National Academy of Sciences*, 107(26):11865–11870, 2010.

[3]   Iain D Couzin, Christos C Ioannou, Güven Demirel, Thilo Gross, Colin J Torney, Andrew Hartnett, Larissa Conradt, Simon a Levin, and Naomi E Leonard. Uninformed individuals promote democratic consensus in animal groups. *Science (New York, N.Y.)*, 334(6062):1578–80, dec 2011.

[4]   Akira Okubo and H. C. Chiang. An analysis of the kinematics of swarming of Anarete pritchardi kim (Diptera: Cecidomyiidae). *Researches on Population Ecology*, 16(1):1–42, 1974.

[5]   Douglas H Kelley and Nicholas T Ouellette. Emergent dynamics of laboratory insect swarms. *Scientific reports*, 3:1073, jan 2013.

[6]   Volker Schaller, Christoph Weber, Christine Semmrich, Erwin Frey, and Andreas R. Bausch. Polar patterns of driven filaments. *Nature*, 467(7311):73–77, 2010.

[7]   Tim Sanchez, Daniel T N Chen, Stephen J Decamp, Michael Heymann, and Zvonimir Dogic. Spontaneous motion in hierarchically assembled active matter. *Nature*, 491(7424):431–434, 2012.

[8]   Shay Gueron and Simon A Levin. Self-organization of Front Patterns in Large Wildebeest Herds, 1993.

[9]   J Shapiro. Thinking about bacterial populations as multicellular organisms. *Annual review of microbiology*, 52:81–104, 1998.

[10]   Gema Malet-Engra, Weimiao Yu, Amanda Oldani, Javier Rey-Barroso, Nir S. Gov, Giorgio Scita, and Loïc Dupré. Collective cell motility promotes chemotactic prowess and resistance to chemorepulsion. *Current Biology*, 25(2):242–250, 2015.

[11]   Tamas Vicsek and Anna Zafeiris. Collective motion. *Physics Reports*, 517(3-4):71–140, 2012.

[12] Iain D Couzin and Jens Krause. Self-Organization and Collective Behavior in Vertebrates. *Advances in the study of behavior*, 32:1–75, 2003.

[13] D J T Sumpter. The principles of collective animal behaviour. *Philosophical Transactions of the Royal Society B*, 361:5–22, 2005.

[14] Jeremie Palacci, Stefano Sacanna, Asher Preska Steinberg, David J Pine, and Paul M Chaikin. Living Crystals of Light-Activated Colloidal Surfers. *Science*, 339, 2013.

[15] Pierre Degond and Jiale Hua. Self-organized hydrodynamics with congestion and path formation in crowds. *Journal of Computational Physics*, 237:299–319, 2013.

[16] Tamas Vicsek, A Czirok, E Ben-Jacob, I Cohen, and O Shochet. Novel type of phase transition in a system of self-driven particles. *Physical Review Letters*, 75(6):4–7, 1995.

[17] John Toner and Yuhai Tu. Flocks, herds, and schools: A quantitative theory of flocking. *Physical Review E*, 58(4):4828–4858, 1998.

[18] Oleksandr Chepizhko, Eduardo G Altmann, and Fernando Peruani. Optimal noise maximizes collective motion in heterogeneous media. *Physical Review Letters*, 110(23), 2013.

[19] Samuel R McCandlish, Aparna Baskaran, and Michael F Hagan. Spontaneous segregation of self-propelled particles with different motilities. *Soft Matter*, 8:2527–2534, 2012.

[20] Gabriel Baglietto, EV Albano, and J Candia. Gregarious vs individualistic behavior in Vicsek swarms and the onset of first-order phase transitions. *Physica A: Statistical Mechanics and its Applications*, 392(15):3240–3247, 2013.

[21] M. DOrsogna, Y. Chuang, A. Bertozzi, and L. Chayes. Self-Propelled Particles with Soft-Core Interactions: Patterns, Stability, and Collapse. *Physical Review Letters*, 96(10):104302, mar 2006.

[22] Veysel Gazi and Kevin M. Passino. A class of attractions/repulsion functions for stable swarm aggregations. *International Journal of Control*, 77(18):1567–1579, dec 2004.

[23] Iain D Couzin, Jens Krause, Nigel R Franks, and Simon a Levin. Effective leadership and decision-making in animal groups on the move. *Nature*, 433(7025):513–6, feb 2005.

[24] Julio Belmonte, Gilberto Thomas, Leonardo Brunnet, Rita de Almeida, and Hugues Chate. Self-Propelled Particle Model for Cell-Sorting Phenomena. *Physical Review Letters*, 100(24):248702, jun 2008.

[25] David A Quint and Ajay Gopinathan. Topologically induced swarming phase transition on a 2D percolated lattice. *Physical Biology*, 0(0):0, 2015.

[26] Gregoire Guillaume and Hugues Chate. Onset of Collective and Cohesive Motion. *Physical Review Letters*, 92(2), 2004.

[27] John Toner, Yuhai Tu, and Sriram Ramaswamy. Hydrodynamics and phases of flocks. *Annals of Physics*, 318(1):170–244, jul 2005.

[28] Julien Barre, Raphael Chetrite, Massimiliano Muratori, and Fernando Peruani. Motility-Induced Phase Separation of Active Particles in the Presence of Velocity Alignment. *Journal of Statistical Physics*, 158:589—-600, 2014.

[29] Gil Ariel, Oren Rimer, and Eshel Ben-Jacob. Order-Disorder Phase Transition in Heterogeneous Populations of Self-propelled Particles. *Journal of Statistical Physics*, pages 579–588, 2014.

[30] Vishwesha Guttal and Iain D Couzin. Social interactions , information use , and the evolution of collective migration. *PNAS*, 107(37), 2010.

[31] Aviram Gelblum. Ant groups optimally amplify the effect of transiently informed individuals. *Nature Communications*, 6:9, 2015.

[32] Kelsi M Sandoz, Shelby M Mitzimberg, and Martin Schuster. Social cheating in Pseudomonas aeruginosa quorum sensing. *Proceedings of the National Academy of Sciences of the United States of America*, 104(40):15876–81, oct 2007.

[33] Kendra P Rumbaugh, Stephen P Diggle, Chase M Watters, Adin Ross-Gillespie, Ashleigh S Griffin, and Stuart a West. Quorum sensing and the social evolution of bacterial virulence. *Current biology : CB*, 19(4):341–5, feb 2009.

[34] Tamas Czaran and Rolf F Hoekstra. Microbial communication, cooperation and cheating: quorum sensing drives the evolution of cooperation in bacteria. *PloS one*, 4(8):e6655, jan 2009.

[35] Vittorio Venturi, Iris Bertani, Adam Kerenyi, Sergiu Netotea, and Sandor Pongor. Co-swarming and local collapse: quorum sensing conveys resilience to bacterial communities by localizing cheater mutants in Pseudomonas aeruginosa. *PloS one*, 5(4):e9998, jan 2010.

[36] Joao Xavier, Wook Kim, and Kevin Foster. A molecular mechanism that stabilizes cooperative secretions in Pseudomonas aeruginosa. *Molecular microbiology*, 79(1):166–179, 2011.

[37] Wangpeng Shi, Yang Guo, Chuan Xu, Shuqian Tan, Jing Miao, Yanjie Feng, Hon Zhao, Raymond St. Leger, and Weiguo Fang. Unveiling the mechanism by which microsporidian parasites prevent locust swarm behavior. *Proceedings of the National Academy of Sciences*, 111(4), jan 2014.

[38] Ali E Turgut, Hande Celikkanat, and Fatih Gokce. Self-organized flocking in mobile robot swarms. *Swarm Intell*, 2:97–120, 2008.

[39] Vinicius Santos, Mario Campos, and Luiz Chaimowicz. *On Segregative Behaviors Using Flocking and Velocity Obstacles*. Springer Berlin Heidelberg, 2014.

[40] Sifat Momen, Bala P. Amavasai, and Nazmul H. Siddique. Mixed species flocking for heterogeneous robotic swarms. *EUROCON 2007 - The International Conference on Computer as a Tool*, pages 2329–2336, 2007.

[41] Adam T. Hayes and Parsa Dormiani-Tabatabaei. Self-organized flocking with agent failure: Off-line optimization and demonstration with real robots. *Proceedings 2002 IEEE International Conference on Robotics and Automation (Cat. No.02CH37292)*, 4:1–7, 2002.

[42] A Stranieri, E Ferrante, AE Turgut, V Trianni, C Pinciroli, M Birattari, and M Dorigo. Self-organized flocking with a heterogeneous mobile robot swarm. *IRIDIA Technical Report Series*, 2011.

[43] J. E. Herbert-Read, Andrea Perna, R. P. Mann, T. M. Schaerf, D. J. T. Sumpter, and A. J. W. Ward. Inferring the rules of interaction of shoaling fish. *Proceedings of the National Academy of Sciences*, 108(46):18726–18731, 2011.

[44] Elod Mehes and Tamas Vicsek. Collective motion of cells : from experiments to models. *Integrative Biology*, 6:831–854, 2014.

[45] B. Szabo, G.J. Szollosi, B. Gonci, Zs. Juranyi, D. Selmeczi, and Tamás Vicsek. Phase transition in the collective migration of tissue cells: Experiment and model. *Physical Review E*, 74(6):1–5, 2006.

[46] Peter Friedl, Joseph Locker, Erik Sahai, and Jeffrey E. Segall. Classifying collective cancer cell invasion. *Nature Cell Biology*, 14(8):777–783, 2012.

[47] Irina V Dokukina and Maria E Gracheva. A model of fibroblast motility on substrates with different rigidities. *Biophysical journal*, 98(12):2794–803, jun 2010.

[48] Andrew Berdahl, Colin J Torney, Christos C Ioannou, Jolyon J Faria, and Iain D Couzin. Emergent sensing of complex environments by mobile animal groups. *Science (New York, N.Y.)*, 339(6119):574–6, 2013.

[49] Adi Shklarsh, Gil Ariel, Elad Schneidman, and Eshel Ben-Jacob. Smart swarms of bacteria-inspired agents with performance adaptable interactions. *PLoS Computational Biology*, 7(9):e1002177, 2011.

[50] Nikhil Mittal, Elena O Budrene, Michael P Brenner, and Alexander Van Oudenaarden. Motility of Escherichia coli cells in clusters formed by chemotactic aggregation. *Proceedings of the National Academy of Sciences of the United States of America*, 100(23):13259–13263, 2003.

[51] Katherine Copenhagen, David A Quint, and Ajay Gopinathan. Self-organized sorting limits behavioral variability in swarms. *Scientific Reports*, 6:31808, aug 2016.

[52] Juliane Zimmermann, Brian A. Camley, Wouter-Jan Rappel, and Herbert Levine. Contact inhibition of locomotion determines cell-cell and cell-substrate forces in tissues. *Proceedings of the National Academy of Sciences of the United States of America*, 113(10):2660–2665, 2016.

[53] Brian A. Camley, Juliane Zimmermann, Herbert Levine, and Wouter Jan Rappel. Emergent Collective Chemotaxis without Single-Cell Gradient Sensing. *Physical Review Letters*, 116(9):1–6, 2016.

[54] Michael Rubenstein, Alejandro Cornejo, and Radhika Nagpal. Programmable self-assembly in a thousand-robot swarm. 345(March):795–799, 2014.

[55] Cristián Huepe and Maximino Aldana. New tools for characterizing swarming systems: A comparison of minimal models. *Physica A: Statistical Mechanics and its Applications*, 387(12):2809–2822, may 2008.

[56] Vladimir Lobaskin and Maksym Romenskyy. Collective dynamics in systems of active Brownian particles with dissipative interactions. *Physical Review E*, 2013.

[57] Yao Li Chuang, Yuan R. Huang, Maria R. D'Orsogna, and Andrea L. Bertozzi. Multi-vehicle flocking: Scalability of cooperative control algorithms using pairwise potentials. *Proceedings - IEEE International Conference on Robotics and Automation*, pages 2292–2299, 2007.

[58] M. C. Marchetti, J. F. Joanny, S. Ramaswamy, T. B. Liverpool, J. Prost, Rao Madan, and R. Aditi Simha. Hydrodynamics of soft active matter. *Reviews of Modern Physics*, 85, 2013.

[59] Jorge M Pacheco, Arne Traulsen, and Martin A Nowak. Active linking in evolutionary games. *Journal of theoretical Biology*, 243:437–443, 2006.

[60] Colin J Torney, Simon a Levin, and Iain D Couzin. Specialization and evolutionary branching within migratory populations. *Proceedings of the National Academy of Sciences of the United States of America*, 107(47):20394–9, nov 2010.

[61] Darren Pais and Naomi E Leonard. Adaptive network dynamics and evolution of leadership in collective migration. *Physica D*, 267:81–93, 2014.

[62] György Szabó and Gábor Fáth. Evolutionary games on graphs. *Physics Reports*, 446:97–216, 2007.

[63] Erez Lieberman, Christoph Hauert, and Martin A Nowak. Evolutionary dynamics on graphs. *Nature*, 433:1–5, 2005.

[64] Hisashi Ohtsuki, Christoph Hauert, Erez Lieberman, and Martin A Nowak. A simple rule for the evolution of cooperation on graphs. *Nature*, 441(7092):502–505, 2006.

[65] David G Rand, Samuel Arbesman, and Nicholas A Christakis. Dynamic social networks promote cooperation in experiments with humans. *Proceedings of the National Academy of Sciences*, 108(48), 2011.

[66] Iain D Couzin, Jens Krause, Richard James, Graeme D Ruxton, and Nigel R Franks. Collective Memory and Spatial Sorting in Animal Groups. *Journal of theoretical Biology*, 218:1–11, 2002.

[67] J Toner and Y Tu. Long-Range Order in a Two-Dimensional Dynamical XY Model: How Birds Fly Together. *Physical Review Letters*, 75(23):4326–4329, 1995.

[68] Herbert Levine, Wouter-Jan Rappel, and Inon Cohen. Self-organization in systems of self-propelled particles. *Physical Review E*, 63(1):017101, dec 2000.

[69] Eric Bertin, Michel Droz, and Guillaume Gregoire. Hydrodynamic equations for self-propelled particles: microscopic derivation and stability analysis. *Journal of Physics A: Mathematical and Theoretical*, 42:445001, 2009.

[70] Quan-Xing Liu, Arjen Doelman, Vivi Rottschafer, Monique de Jager, Peter M J Herman, Max Rietkerk, and Johan van de Koppel. Phase separation explains a new class of self-organized spatial patterns in ecological systems. *Proceedings of the National Academy of Sciences of the United States of America*, 110(29):11905–10, jul 2013.

[71] Jacques Gautrais, Christian Jost, Marc Soria, Alexandre Campo, Sébastien Motsch, Richard Fournier, Stéphane Blanco, and Guy Theraulaz. Analyzing fish movement as a persistent turning walker. *Journal of Mathematical Biology*, 58(3):429–445, 2009.

[72] Kevin Doxzen, Sri Ram Krishna Vedula, Man Chun Leong, Hiroaki Hirata, Nir S. Gov, Alexandre J. Kabla, Benoit Ladoux, and Chwee Teck Lim. Guidance of collective cell migration by substrate geometry. *Integrative Biology*, 5(8):1026, 2013.

[73] M. B. Wan, C. J. Olson Reichhardt, Z. Nussinov, and C. Reichhardt. Rectification of swimming bacteria and self-driven particle systems by arrays of asymmetric barriers. *Physical Review Letters*, 101(1):1–4, 2008.

[74] Katherine Copenhagen and Ajay Gopinathan. Active matter clusters at interfaces. *Frontiers in materials*, 3(March):1–8, 2016.

[75] Kolbjorn Tunstrom, Yael Katz, Christos C. Ioannou, Cristian Huepe, Matthew J. Lutz, and Iain D. Couzin. Collective States, Multistability and Transitional Behavior in Schooling Fish. *PLoS Computational Biology*, 9(2), 2013.

[76] Zhao Cheng, Zhiyong Chen, Tamás Vicsek, Duxin Chen, and Hai-Tao Zhang. Pattern phase transitions of self-propelled particles: gases, crystals, liquids, and mills. *New Journal of Physics*, 18(10):103005, 2016.

[77] Fong Yew Leong. Physical explanation of coupled cell-cell rotational behavior and interfacial morphology: A particle dynamics model. *Biophysical Journal*, 105(10):2301–2311, 2013.

[78] Brian A. Camley, Yunsong Zhang, Yanxiang Zhao, Bo Li, Eshel Ben-Jacob, Herbert Levine, and Wouter-Jan Rappel. Polarity mechanisms such as contact inhibition of locomotion regulate persistent rotational motion of mammalian cells on micropatterns. *Proceedings of the National Academy of Sciences*, 111(41):14770–14775, 2014.

[79] Jakob Lober, Falko Ziebert, and Igor S Aranson. Collisions of deformable cells lead to collective migration. *Scientific reports*, 5:9172, 2015.

[80] Udo Erdmann, Werner Ebeling, and Alexander S. Mikhailov. Noise-induced transition from translational to rotational motion of swarms. *Physical Review E*, 71(5):051904, 2005.

[81] Yao-li Chuang, Maria R. D'Orsogna, Daniel Marthaler, Andrea L. Bertozzi, and Lincoln S. Chayes. State Transitions and the Continuum Limit for a 2D Interacting, Self-Propelled Particle System. (February 2008), 2006.

[82] J A Carrillo, A Klar, and A Roth. Single to Double Mill Small Noise Transitions via Semi-Lagrangian Finite Volume Methods. M:1–25, 2014.

[83] Kandice Tanner, Hidetoshi Mori, Rana Mroue, Alexandre Bruni-Cardoso, and Mina J Bissell. Coherent angular motion in the establishment of multicellular architecture of glandular tissues. *Proceedings of the National Academy of Sciences of the United States of America*, 109(6):1973–8, 2012.

[84] Clifford Brangwynne, Kevin Kit Parker, Sui Huang, and Donald E. Ingber. Symmetry breaking in cultured mammalian cells. *In Vitro Cell. Dev. Biol.*, 36, 2000.

[85] Bo Li and Sean X. Sun. Coherent motions in confluent cell monolayer sheets. *Biophysical Journal*, 107(7):1532–1541, 2014.

[86] Felix J. Segerer, Florian Thuroff, Alicia Piera Alberola, Erwin Frey, and Joachim O. Radler. Emergence and persistence of collective cell migration on small circular micropatterns. *Physical Review Letters*, 114(22):1–5, 2015.

[87] Gema Malet-Engra, Weimiao Yu, Amanda Oldani, Nir Gov, Loic Dupre, and Giorgio Scita. Collective Cell Motility Promotes Chemotactic Prowess and Resistance to Chemorepulsion. *Current biology : CB*, 2014.

[88] Victoria Tarle, Andrea Ravasio, Vincent Hakim, and Nir S. Gov. Modeling the finger instability in an expanding cell monolayer. *Integr. Biol.*, pages 1–14, 2015.

[89] Wouter-Jan Rappel. Cellcell communication during collective migration. *Proceedings of the National Academy of Sciences*, 113(6):201524893, 2016.

[90] Nestor Sepulveda, Laurence Petitjean, Olivier Cochet, Erwan Grasland-Mongrain, Pascal Silberzan, and Vincent Hakim. Collective cell motion in an epithelial sheet can be quantitatively described by a stochastic interacting particle model. *PLoS computational biology*, 9(3):e1002944, jan 2013.

[91] F. Peruani, A. Deutsch, and M. Bär. A mean-field theory for self-propelled particles interacting by velocity alignment mechanisms. *European Physical Journal: Special Topics*, 157(1):111–122, 2008.

[92] Shradha Mishra, Kolbjorn Tunstrom, Iain D. Couzin, and Cristian Huepe. Collective dynamics of self-propelled particles with variable speed. *Physical Review E - Statistical, Nonlinear, and Soft Matter Physics*, 86(1):1–11, 2012.

[93] Christoph a. Weber, Christopher Bock, and Erwin Frey. Defect-Mediated Phase Transitions in Active Soft Matter. *Physical Review Letters*, 112(16):168301, 2014.

[94] Luca Giomi, Mark J. Bowick, Xu Ma, and M. Cristina Marchetti. Defect annihilation and proliferation in active Nematics. *Physical Review Letters*, 110(22):1–5, 2013.

[95] G. Duclos, S. Garcia, H. G. Yevick, and P. Silberzan. Perfect nematic order in confined monolayers of spindle-shaped cells. *Soft Matter*, 10(14):2346–2353, 2014.

[96] Andre Levchenko and Pablo a Iglesias. Models of eukaryotic gradient sensing: application to chemotaxis of amoebae and neutrophils. *Biophysical journal*, 82(1 Pt 1):50–63, 2002.

[97] Brian A. Camley, Juliane Zimmermann, Herbert Levine, and Wouter-Jan Rappel. Emergent collective chemotaxis without single-cell gradient sensing. *arXiv*, page 20, 2015.

[98] Michael Tinkham. *Introduction to superconductivity*. 1996.

[99] Pernille Rorth. Fellow travellers: emergent properties of collective cell migration. *EMBO reports*, 13(11):984–991, 2012.

[100] Mark J Miller, Sindy H Wei, Ian Parker, and Michael D Cahalan. Two-photon imaging of lymphocyte motility and antigen response in intact lymph node. *Science (New York, N.Y.)*, 296(5574):1869–1873, 2002.

[101] David Bilder and Saori L. Haigo. Expanding the Morphogenetic Repertoire: Perspectives from the Drosophila Egg. *Developmental Cell*, 22(1):12–23, 2012.

[102] Danfeng Cai, Wei Dai, Mohit Prasad, Junjie Luo, Nir S. Gov, and Denise J. Montell. Modeling and analysis of collective cell migration in an in vivo three-dimensional environment. *Proceedings of the National Academy of Sciences*, 113(15), 2016.

[103] Eliseo Ferrante, Ali Emre Turgut, Marco Dorigo, and Cristian Huepe. Elasticity-based mechanism for the collective motion of self-propelled particles with springlike interactions: A model system for natural and artificial swarms. *Physical Review Letters*, 111(26):1–5, 2013.